Galactic Magnetic Fields and the Small-Scale Dynamo

Dissertation

zur
Erlangung der naturwissenschaftlichen Doktorwürde
(Dr. sc. nat.)

vorgelegt der
Mathematisch-naturwissenschaftlichen Fakultät

der
Universität Zürich

von
Michael Horst Rieder

aus
Deutschland

Promotionskommission
Prof. Dr. Romain Teyssier (Vorsitz)
Prof. Dr. Lucio Mayer
Prof. Dr. Christoph Pfrommer

Zürich, 2017

Zusammenfassung

Magnetfelder sind im Universum allgegenwärtig und in einer Vielzahl von astronomischen Systemen zu finden. Diese reichen von kompakten Objekten wie Planeten, Sternen und sogar schwarzen Löchern bis zu ausgedehnten Strukturen wie Molekülwolken und Galaxien, und sogar im intergalaktischen Medium, wie der weite Raum zwischen den Galaxien genannt wird, finden sich Hinweise auf Felder gewisser Grösse. Es ist schon lange bekannt, dass die in der Erde und der Sonne vorkommenden Feldstärken so hoch sind, dass sie auf mannigfaltige Weise Einfluss auf die Dynamik ihrer Umgebung haben. Was Galaxien betrifft, so bedurfte es erst Polarisationsmessungen mittels moderner Radioteleskope mit hoher Sensitivität und Breitband-Technik sowie neuer Methoden zur Datenanalyse, um ein genaueres Bild der Verhältnisse zu bekommen.

Die hohe Komplexität der Magnetohydrodynamik-Gleichungen, welche die zeitliche Entwicklung eines magnetisierten Plasmas beschreiben, erlaubt eine analytische Lösung nur in stark vereinfachten Bedingungen, sodass man für verlässtiche Aussagen diesbezüglich auf rechnergestützte Simulationen zurückgreifen muss. Numerische Modelle zu Entstehung sowie Entwicklung von Galaxien sind jedoch schon ohne Betrachtung von Magnetfeldern äusserst rechenaufwendig und erfordern leistungsstarke Rechencluster, um einen möglichst weiten dynamischen Raum von sub-parsec bis vielen Millionen von parsec abzudecken. Durch beständige Leistungssteigerung der verfügbaren Computertechnologie - insbesondere auch auf dem Gebiet der Parallelisierung - wird es indes zunehmend durchführbarer, die zusätzlichen Anforderungen der Magnetohydrodynamik in Kauf zu nehmen.

Die Entstehung der ersten Magnetfelder im Universum wird mit sogenannten Keimfeldern erklärt, welche auf verschiedene Arten entstehen können, jedoch allgemein sehr schwach sind. Astronomische Beobachtungen zeigen indessen, dass die gemessenen Magnetfelder viel stärker sind und ein Prozess der Selbstverstärkung stattgefunden

haben muss. Theorien zu magnetischen Dynamos beschreiben, wie gewisse Plasma-Bewegungen dazu in der Lage sind, Feldlinien auf eine Art zu krümmen, dass sich die Magnetfelder selbst potenzieren und eine Umwandlung von kinetischer in magnetische Energie ihren Lauf nimmt. Sogenannte schnelle Dynamos wie der Turbulenz-Dynamo, dessen Wirkungsweise durch die Kazantsev-Theorie beschrieben wird, können auf kosmischem Masstab sehr kurze Verdopplungszeiten aufweisen und Keimfelder innerhalb kürzester Zeit fast auf Äquipartitionsniveau bringen.

Die vorliegende Arbeit untersucht mit Hilfe von kombinierten Gravitations- und Magnetohydrodynamik-Simulationen, wie in modellierten Galaxien durch Feedback-Prozesse erzeugte Turbulenz einen Kazantsev-Dynamo antreiben kann. Diese Feedback-Prozesse können verschiedener Natur sein und umfassen hier Supernova-Explosionen und Strahlung von Sternen, es sind jedoch auch darüber hinaus andere Mechanismen wie z. B. Jets von Schwarzen Löchern denkbar. Supernovae sind besonders wirkungsvoll in Zwerggalaxien, da deren geringeres Gravitationspotential leichter überwunden werden kann. Der so entstehende Turbulenz-Dynamo kann schwache Keimfelder in sehr kurzer Zeit verstärken, bis schliesslich die Saturationsphase eintritt. In dieser Phase wird jedoch keine Äquipartition erreicht und die Magnetfelder haben nur eine schwache regelmässige Komponente, was sich erst durch Plasmakompression in weniger turbulenten Phasen oder durch andere Dynamo-Prozesse ändert. In voll kosmologischen Simulationen wird dieses Szenario bestätigt und gezeigt, dass die Magnetfelder rapide und schon bei hoher Rotverschiebung wachsen.

Diese Dissertation zeigt ein Szenario auf, in dem anfangs schwache Magnetfelder in Zwerggalaxien in kürzester Zeit durch den von Supernova-Feedback angetriebenen Turbulenz-Dynamo verstärkt wurden. Nachdem sich die ersten Strukturen im frühen Universum ausgebildet hatten, begannen sich durch ihre eigene Gravitation kompakte Objekte zu bilden, welche ultimativ zu Sternen wurden und Kernfusion ermöglichten. Die hierdurch freigesetzten enormen Energiemengen erzeugten starke Turbulenzen in Zwerggalaxien, wodurch wiederum die Keimfelder schnell fast auf Äquipartitionsstärke anwuchsen, und später durch andere Prozesse dann weiter verstärkt und umgeformt wurden. Die in heutigen benachbarten Galaxien wie

auch der Milchstrasse beobachteten Magnetfelder sind das Resultat dieser Evolution, nachdem sie durch Verschmelzungen von Zwerggalaxien und darauf folgener Restrukturierung starke regelmässige wie auch turbulente Magnetfeld-Komponenten ausgebildet haben.

Abstract

Magnetic fields are ubiquitous in the Universe and can be found in a variety of astronomical systems. These range from compact objects like planets, stars and even black holes to extended structures like molecular clouds and galaxies. Even the vast spaces between galaxies, called intergalactic medium, hold evidence of weak fields. It is long known that inside the Earth and the Sun the measured field strengths are so intense that they influence the dynamics of the surrounding environment in a variety of ways. In regard to galaxies, it was not until the advent of polarisation measurements with modern high-sensitivity radio telescopes with broadband-technology and new methods of data analysis, that it was possible to reconstruct a more exact description.

The high complexity of magnetohydrodynamics equations which govern the time evolution of magnetised plasmas permit analytic solutions only under extremely simplified assumptions. Therefore one must rely on computer-based simulations to obtain reliable conclusions. Even when neglecting magnetic fields, numerical models for the formation and the evolution of galaxies are extremely demanding from a computational point of view and require high-performance computer clusters, since these simulations should idealistically span over a wide dynamic spatial range, from sub-parsec up to millions of parsecs. Through continuous increase in performance of the available computational technology, particularly in terms of parallelisation, it has become more and more viable to take into account the additional demands imposed by magnetohydrodynamics.

The origin of the first magnetic fields in the Universe is normally explained in terms of the so-called seed fields, which could arise in different ways, but are generally very weak. However, astronomical observations reveal that the magnetic fields we measure are much stronger than those first seed fields, so that a process of self-amplification must have occurred at some point. Theories of magnetic dynamos describe how certain plasma motions are capable of bending the field lines in a

way, such that magnetic field strengths increase via a transformation from kinetic to magnetic energy. So-called fast dynamos such as the turbulent dynamo, whose operation is described by the theory of Kazantsev, can exhibit very short doubling times on cosmic scales and bring the seed fields almost to equipartition level in an extremely short time.

By using combined gravitational and magnetohydrodynamical simulations, this work investigates how feedback-generated turbulence can establish a Kazantsev dynamo mechanism in modelled galaxies. These feedback processes can vary in nature and in our case include supernova explosions and stellar radiation, but further different viable mechanisms might be conceivable, such as black hole jets. Supernovae are especially effective in dwarf galaxies because of their shallow gravitational potential, which can be overcome more easily. The turbulent dynamo established this way can strengthen the weak seed fields in a very short time until ultimately the saturation phase sets in. In this phase, however, equipartition is not reached and the magnetic fields show only a weak regular component, which can later become stronger through plasma compression in less turbulent phases or other types of dynamo processes. This scenario is confirmed in fully cosmological simulations and shows that magnetic fields grow rapidly and already at high redshift.

This dissertation illustrates a scenario in which the initially weak magnetic fields were quickly amplified inside dwarf galaxies through a turbulent dynamo fuelled by supernova feedback. After the first structures in the early Universe have formed, compact objects began to develop due to self-gravity, eventually becoming stars and allowing nuclear fusion. The high amount of energy liberated in this way induced strong turbulence in dwarf galaxies, whereby the seed fields quickly grow almost to equipartition and then are afterwards amplified further or reshaped by other processes. The magnetic fields observed in nearby galaxies as well as in the Milky Way today are the result of this evolution, after they developed strong regular as well as turbulent magnetic field components through galaxy mergers and subsequent restructuring.

Galactic Magnetic Fields and the Small-Scale Dynamo

Michael Rieder

Michael Rieder
Institute for Computational Science
Universität Zürich
Winterthurerstrasse 190
CH-8057 Zürich
Schweiz

Contents

Preface **xi**

1 Magnetic fields in the Universe **1**
1.1 Magnetism . . . 1
1.1.1 The mysterious force . . . 1
1.1.2 The guidance system . . . 4
1.2 Astronomical observations . . . 5
1.2.1 Compact objects . . . 5
1.2.2 Galaxies and the interstellar medium . . . 7
1.3 Magnetohydrodynamics . . . 8
1.4 The Reynolds number . . . 11
1.4.1 Turbulence . . . 14
1.5 Numerical simulations . . . 15
1.6 Seed fields . . . 17
1.6.1 Primordial magnetic fields . . . 17
1.6.2 Subsequent generation . . . 18
1.7 Dynamo theory . . . 19
1.7.1 The fast dynamo . . . 20
1.7.2 The small-scale dynamo . . . 21
1.8 A brief history of galaxies . . . 22

2 Small-scale dynamo amplification **25**
2.1 Introduction . . . 26
2.2 Numerical methods . . . 29
2.2.1 Ideal MHD solver . . . 29
2.2.2 Cooling and star formation . . . 31
2.2.3 Stellar feedback . . . 32
2.3 Initial conditions . . . 34
2.3.1 Initial halo . . . 34
2.3.2 Initial magnetic field . . . 35
2.3.3 Summary of additional physics parameters . . . 38
2.4 Field amplification by feedback processes . . . 38
2.4.1 Dwarf galaxy . . . 40
2.4.2 Milky-Way-like galaxy . . . 57

2.5 Discussion . . . 59
2.5.1 Implications for high-redshift galaxies . . . 64
2.5.2 Transition to quiescent, low-redshift galaxies . . . 65
2.6 Conclusions . . . 70

3 Small-scale dynamo saturation 73
3.1 Introduction . . . 74
3.2 Numerical methods . . . 78
3.2.1 Ideal MHD with Gravity . . . 78
3.2.2 Turbulence . . . 79
3.3 Initial conditions . . . 81
3.4 Results . . . 83
3.4.1 Saturation of the small-scale dynamo . . . 86
3.4.2 Effect of Resolution . . . 93
3.4.3 Transition to Quiescence . . . 94
3.5 Discussion . . . 100
3.6 Conclusions . . . 104

4 Cosmological evolution 105
4.1 Introduction . . . 106
4.2 Method . . . 108
4.3 Results . . . 111
4.4 Discussion . . . 114
4.5 Conclusions . . . 117

5 Comparison to observations 119
5.1 Faraday Rotation . . . 119
5.2 Simulated observations . . . 120
5.2.1 Through the telescope . . . 122
5.2.2 Ionised magnesium . . . 122
5.2.3 Velocity dispersion . . . 125
5.3 Conclusions . . . 127

6 Summary 129

Bibliography 133

Preface

'Where shall I begin, please your Majesty?' he asked.
'Begin at the beginning,' the King said gravely,
'and go on till you come to the end: then stop.'

Alice's Adventures in Wonderland (Lewis Carroll)

This dissertation can be regarded in a sense as the final result of my research during my time as a doctoral student at the University of Zurich. It seems to me, however, that life is an everlasting lesson and the Universe an everlasting enterprise where no process is isolated in itself. In that respect, I think that the initial statement is not an entirely adequate description and that in fact many teachers, artists, researchers, friends, strangers and family and the experience of 30 years have culminated in this work which was influenced by and hopefully will influence the works of others in some way or another.

That being said, I am happy to thank my supervisor Prof. Dr. Romain Teyssier sincerely for his guidance, patience, and faith in me, without which all this would have certainly been unattainable.

Zürich, July 2017

Für meine Eltern
Barbara und Horst

1 Magnetic fields in the Universe

This chapter contains a general introduction to the main topic of this work. We will cover what is known about magnetism, what astronomers observe about magnetic fields, how we can describe a theory for their evolution in the Universe, where they may have originated, how they became amplified thereafter, and how we can attempt to study their evolution. This will set the stage for the following chapters where we will investigate based on this framework, how magnetic fields in galaxies might have evolved to their present-day form.

1.1 Magnetism

1.1.1 The mysterious force

Les miracles véritables, qu'ils font peu de bruit!

Lettre à un otage (Antoine de Saint-Exupéry)

The natural phenomenon of magnetism was already known to mankind since the Iron Age. Indeed, there is evidence of objects made from iron of meteoritic origin found in Sumerian and Egyptian tombs dating back to the Bronze or even Chalcolithic Ages, as well as the Throne Room in the palace of Knossos in Crete (15th century BC) which is paved with flagstone made of iron oxide (Du Trémolet de Lacheisserie et al., 2005), but there is no conclusive evidence that people were aware of its magnetic properties at that time. It is impossible to tell whether they were or if it is due to the fact that written records from that time are sparsely preserved.

As a matter of fact, it is only by the testimony of Aristotle (*De Anima*, 350 BC) that we can attribute knowledge of lodestone ('the stone has soul because it moves iron') to Thales of Miletus who lived around 600 BC. These naturally magnetized pieces of the mineral magnetite, the iron oxide $\mathrm{Fe_3O_4}$, had surely drawn the attention of many ancient philosophers, as documented by several references in classical Greek

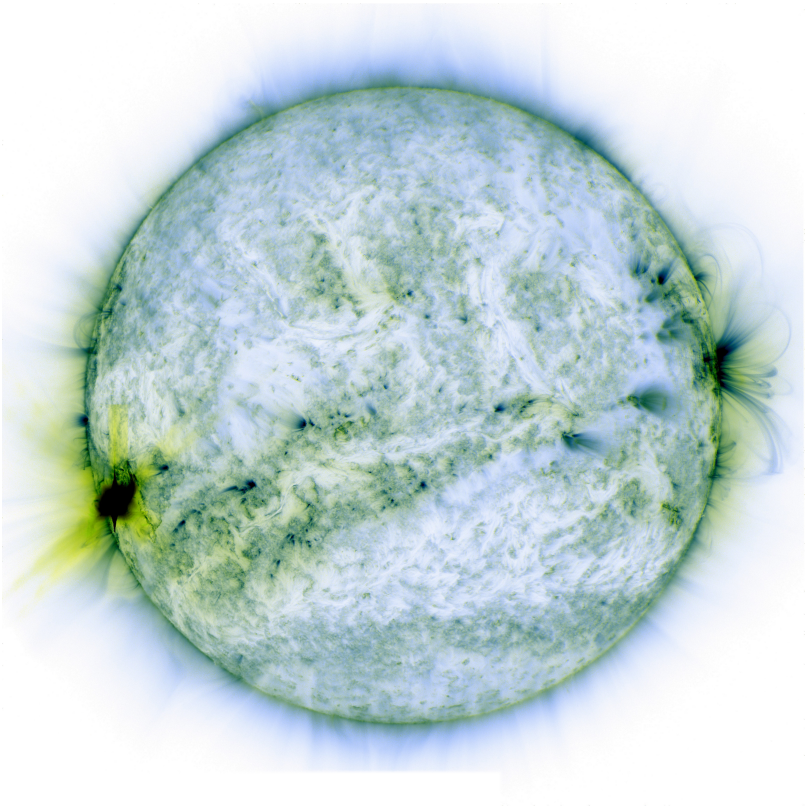

Figure 1.1: The Sun as seen on March 7, 2015 by NASA's Solar Dynamics Observatory as a composite image at 171 and 131 Angstroms. Visible loops in the corona illustrate closed magnetic field lines between sunspots. Image: NASA / SDO.

and Latin literature. Lucretius (*De rerum natura*, 1st century BC), for example, mentions 'this stone capable of guiding iron that the Greeks call Magnet, since it originates in the land of the Magnetes'. This associates the origin of the contemporary word *magnet* with the geographical region around present-day Magnesia in Thessaly, or alternatively colonies of the Magnetes in Western Anatolia. The latter is supported by Sophocles (*Alexandros*, 5th century BC) calling it the 'Lydian stone' and Plato (*Timaeus*, 360 BC) mentioning the 'attraction of amber and the Heraclean stones', which is interpreted by scholars as a reference to the region Asia Minor (Caley and Richards, 1956). Pliny The Elder (*Naturalis Historia*, 77 AD) mentions important quarries for 'magnetic stone' existing in both regions, but describes the ones from Asia (the Roman province in Western Anatolia) and Troas as 'female', meaning without magnetic attraction. This is probably a reference to minerals of the elements Magnesium and Manganese, since many stones of various colours and magnetic properties shared the name 'magnetic stone' and their distinction as being made from different elements was not clear at the time. Interestingly, Pliny's explanation for their name is not geographic and uses the mythical figure of a shepherd called Magnes instead, who is said to have stumbled upon it on Mount Ida when he felt the magnetic force on the nails in his shoes. This account has the typical appearance of a legend, however, and the previous explanation seems more plausible.

Ancient people were deeply impressed by the invisible force emanating from lodestone and tried their best to explain this behaviour, and it seems that this natural phenomenon was an important test for their philosophies. Thales thought that it must contain some kind of 'soul' since it was able to move other objects as if it was a living being. Centuries later, it was believed that it was rather a law of nature that magnets had an invisible outflaw that caused a certain 'vacuum' around them which made iron and other magnets fill the void. Lucretius gives a detailed description of this mechanism and reports that 'men marvel at this stone' when he writes that a lodestone could hold several separate iron rings suspended from each other. It is worth noting that Plato already connects the distinct phenomena caused by lodestone and amber (which was called *elektron* in Greek), since they had similar capabilities of attracting objects. Thus, he had an early indication for a link between the electric and the magnetic forces, a

principle which would take 2 millenia to find a theoretical explanation for. Despite those sophisticated theories, however, the magnet remained mainly a curiosity for Greeks and Romans as they were not able to refine their understanding of magnetic poles or discover the Earth's own magnetic field.

1.1.2 The guidance system

Follow the white rabbit...
Knock knock Neo.
The Matrix (Larry and Andy Wachowski)

It were instead Chinese scholars who, at the same time, discovered that an elongated lodestone, sculpted in the shape of a spoon, adjusted its orientation roughly along the north-south axis (Lowrie, 2007). Its first use was probably rather spiritual in that it helped building houses in accordance with the principle of *feng shui*, and it turned into a navigational instrument only later. By the beginning of the second millenium, Chinese craftsmen knew that melting iron and subsequently cooling it with its long axis lying along the earth's magnetic field would magnetise it to form compass needles (Du Trémolet de Lacheisserie et al., 2005). In medieval Europe, Petrus Peregrinus de Maricourt wrote a letter in 1269 describing his knowledge of magnets, where he draws a link between the celestial poles and the magnetic poles of a lodestone that he polished into a spherical shape, thus attributing to it the 'likeness of heavens'. From there, William Gilbert (*De Magnete*, 1600) took on to put his knowledge on a scientific basis by rigorously testing hypotheses in experiments rather than relying on mystic interpretations.

This finally set the stage for modern science to take over and in 1743, Daniel Bernoulli invented the horseshoe magnet in Switzerland (Coey, 2010). The last missing puzzle piece was the understanding of electric currents. In 1820, Hans Christian Oersted discovered the existence of magnetic fields around the current inside a wire and spawned research by many scientists such as André-Marie Ampère, Michael Faraday, Pierre-Simon de Laplace and many others. James Clerk Maxwell then finally found the common analytical description with his theory of the electromagnetic field which he presented to the

Royal Society in London in 1864. His pioneering work combining the previously known laws governing the topology and evolution of electric and magnetic fields into one set of equations and introducing the displacement current into them laid the foundation for rigorous theoretical analysis and his discovery of electromagnetic waves in Maxwell (1865). His formulation was slightly cumbersome and used potentials, thus it was only after Oliver Heaviside put them in their vector calculus form (Hunt, 1991)

$$\begin{array}{ll} \nabla \cdot \mathbf{E} = 4\pi\rho & c\nabla \times \mathbf{E} = -\partial_t \mathbf{B} \\ \nabla \cdot \mathbf{B} = 0 & c\nabla \times \mathbf{B} = \partial_t \mathbf{E} + 4\pi\mathbf{J} \end{array} \tag{1.1}$$

which simplified their appearance and remains the basis for our understanding of electromagnetic fields to this day. The equations are given in cgs units which are still customary in astronomy and astrophysics, but also have the nice side effect that the electric field $\mathbf{E}$ and the magnetic field $\mathbf{B}$ have the same units. The displacement current term $\partial_t \mathbf{E}$ leads to the presence of electromagnetic waves, but will be of minor importance in the context of cosmic time scales (Brandenburg and Subramanian, 2005).

1.2 Astronomical observations

1.2.1 Compact objects

> Der Weise als Astronom. - Solange du noch die Sterne fühlst als ein »Über-dir«, fehlt dir noch der Blick des Erkennenden.
>
> *Jenseits von Gut und Böse (Friedrich Wilhelm Nietzsche)*

Magnetic fields are widely observed in the Universe in virtually all astrophysical objects on a variety of scales. Naturally, planet Earth was the first object where a field was discovered, but space probes sent to explore the solar system found magnetic fields around nearly all planets. Most of them have centred dipole moments with their axes loosely aligned to their rotation axis. An exception to this are Uranus and Neptune with strongly inclined and highly off-centred dipole moments and Mars which does not have any global magnetic field but only small-scale components, which are probably local remnants of a once strong field similar to Earth's (Rüdiger and Hollerbach, 2004).

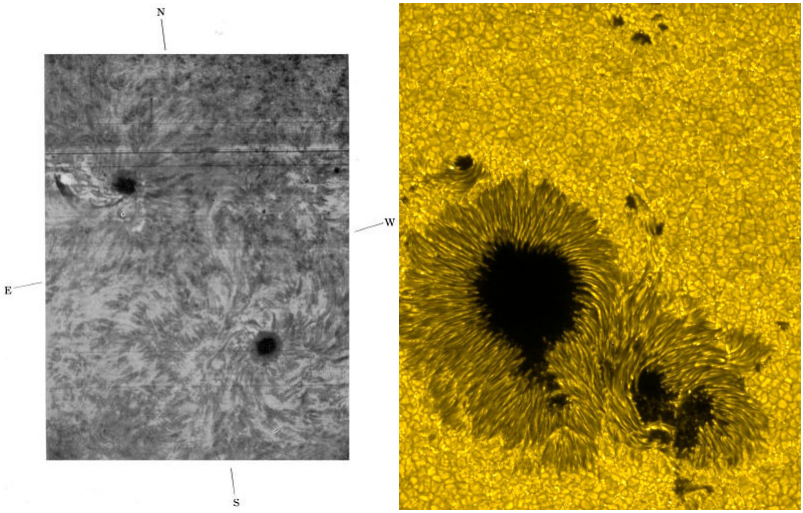

Figure 1.2: Sunspots and hydrogen flocculi with left- and right-handed vortices as seen by Hale on September 9, 1908 (left). Reproduction of photographic plate 27 from Hale (1908b). Modern image in the visible spectrum taken on December 13, 2006 by Hinode's Solar Optical Telescope (SOT) (right). Dark sunspots with surrounding filamentary structure with alternating sense of rotation are clearly visible. Image: Hinode JAXA/NASA.

The Sun itself hosts a magnetic dipole as well, but its differential rotation tends to wind up the field lines into toroidal fields, which gives it a more complex structure. In 1908, George Ellery Hale pointed out that the way the plasma on the Sun's surface was shaped around sunspots looked like iron filings in a magnetic field (Hale, 1908a) and, in the very same volume of the Astrophysical Journal, showed that sunspots are actually magnetic phenomena with opposing polarity by the presence of Zeeman splitting (Hale, 1908b). A comparison of the photographic plates used in his work with a modern high-resolution image is shown in Figure 1.2.

Similar magnetic activity has also been found in observations of other stars with external convection envelopes (Berdyugina, 2005). The magnetic field strengths inferred from the pulsation times of

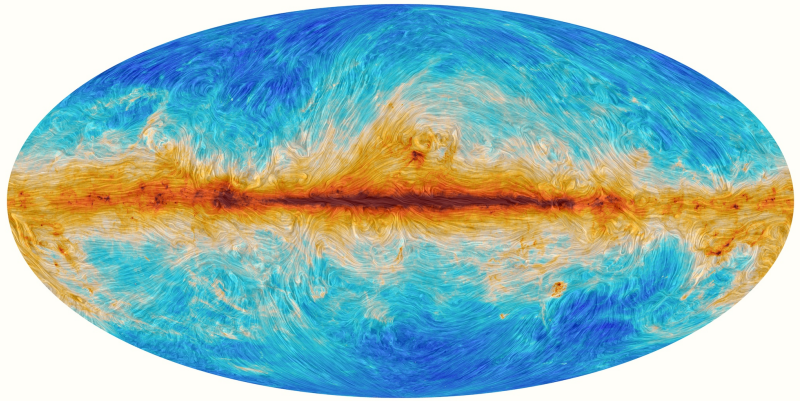

Figure 1.3: Orientation of magnetic field lines based on polarisation measurements and total intensity of dust emission in the Milky Way. Image: ESA / Planck Collaboration.

neutron stars suggest very strong magnetic fields between 10^8 G in millisecond pulsars and 10^{15} G in soft gamma-ray repeaters (Reisenegger, 2007). In first promising results from Event Horizon Telescope data, Johnson et al. (2015) confirmed the signature of ordered magnetic fields around the black hole Sagittarius A* in the centre of the Milky Way galaxy, which foreshadows interesting insights into the dynamics of central galactic environments.

1.2.2 Galaxies and the interstellar medium

Adieu, dit le renard. Voici mon secret.
Il est très simple: On ne voit bien qu'avec le cœur.
L'essentiel est invisible pour les yeux.

Le Petit Prince (Antoine de Saint-Exupéry)

Apart from these localised objects, the vast gas-filled spaces between them called the interstellar medium are threaded by magnetic fields as well, as has been confirmed by various measurement techniques. In the Solar neighbourhood, space probe Voyager 1 found a steady magnetic field in the local ISM of $3\,\mu$G (Burlaga, 2015). Faraday

rotation measures from distant pulsars indicate a mean value for the local regular field of about $2\,\mu$G in the solar neighbourhood and $4\,\mu$G at a galacto-centric radius of 3 kpc (Han et al., 2006). At the same time, there is evidence of strong turbulent fields as well, with mean strengths of $4 - 6\,\mu$G and on spatial scales between 10 and $100\,\mathrm{pc}$ (Ohno and Shibata, 1993), also based on pulsar-based rotation measure analysis. Observations of nearby galaxies yield similar results. In a review of magnetic fields in spiral galaxies, Beck (2016) aggregates data from the literature which finds total field strengths ranging from $9\,\mu$G in spirals, $17\,\mu$G in bright, $20 - 30\,\mu$G in highly star-forming, up to $100\,\mu$G in star-burst galaxies. These values are based on the equipartition assumption between magnetic and cosmic ray energy densities which may be subject to bias (Beck et al., 2003), but are in reasonable range compared to the Milky Way measurements above. The strength of ordered magnetic fields is slightly smaller, between $10 - 15\,\mu$G for high star formation rates and $5\,\mu$G in bright galaxies where the ratio of total to ordered fields seems to be about 3 (Fletcher, 2010). The average pressure of total magnetic fields is found to be comparable to the turbulent kinetic energy density, as is the case in IC 342 (Beck, 2015). In a sample of 17 spiral galaxies, Heesen et al. (2014) found that B_{tot} scales with the star-formation rate surface density Σ_{SFR} as

$$B_{\mathrm{tot}} \propto {\Sigma_{\mathrm{SFR}}}^{0.3}. \tag{1.2}$$

As far as the present-day Local Group environment is concerned, magnetic fields in dwarf galaxies are generally weaker than in spirals with a total field strength of $4.2\,\mu$G on average (in a sample of 12) and up to $10\,\mu$G in the star-burst dwarf IC 10 (Chyży et al., 2011). As in the case of spiral galaxies, also here a correlation of the total magnetic field with star-formation rate surface density is found with the same power-law exponent of 0.3. Moreover, similar field strengths are even found in high-redshift galaxies, ie. when the Universe was much younger. Analysing rotation measure data from distant quasars, Bernet et al. (2008) found the imprint of strong magnetic fields in intervening normal galaxies at redshift $z = 1.3$, a cosmological era about one third the age of the present Universe. This suggests that any amplification processes working on weaker seed fields must have been very rapid.

1.3 Magnetohydrodynamics

Simplify, simplify.
Walden (Henry David Thoreau)

In order to model the evolution of the Universe, whether on large scale or smaller scales such as galaxies, we need to follow the evolution of the partly ionised gas that permeates it. In our Galaxy, hydrogen amounts to 90 % and helium to 9 % of all atoms (Ferrière, 2001), the tiny rest being heavier elements. As we have seen in Section 1.2, magnetic fields can be dynamically important in the context of galaxy formation, thus should not be neglected. The equations of ideal magnetohydrodynamics, or in short "ideal MHD", used to approximate the plasma make a number of assumptions that simplify them. It is therefore beneficial to consider their derivation to highlight the simplifications rather than just stating the final result.

The analytical expression to describe a magnetised gas or fluid flow of a certain species of charged particles can be derived by integrating the Boltzmann equation over velocity space, assuming for the sake of our purpose that the long-range forces are given by gravity and the Lorentz force. As will become clear in Section 1.5, the viscosity force can be neglected since the numerical method of solving the non-viscous Euler equations exhibits an inherent viscosity. The three equations

$$\begin{aligned}
&\partial_t \rho + \nabla \cdot (\rho \mathbf{U}) = 0 && \text{(mass)} \\
&\partial_t (\rho \mathbf{U}) + \nabla \cdot \left(\rho \mathbf{U}\mathbf{U}^{\mathrm{T}} + \mathbf{P}\right) = \\
&\quad \rho_c \left(\mathbf{E} + c^{-1}\mathbf{U} \times \mathbf{B}\right) - \rho \nabla \phi && \text{(momentum)} \\
&\partial_t (\rho e) + \nabla \cdot [(\rho e + p)\,\mathbf{U}] = \rho_c \mathbf{E} \cdot \mathbf{U} && \text{(energy)}
\end{aligned} \tag{1.3}$$

incorporate the laws of transport for mass, momentum and energy, where ρ and ρ_c are the mass and charge densities, $\mathbf{U}$ is the flow velocity field, $\mathbf{P}$ and p are the isotropic pressure tensor and scalar, $\mathbf{E}$ and $\mathbf{B}$ are the electric and magnetic fields, ϕ is the gravitational potential, and $e = \frac{1}{2}\mathbf{U}^2 + \epsilon + \phi$ is the sum of specific kinetic, internal, and gravitational potential energies. The equations above are in fact conservation equations.

We will consider a quasi-neutral plasma of positively-charged ions and negative electrons, i.e. we assume that

$$n_i \approx n_e \tag{1.4}$$

where n_i and n_e are the number densities of the ions and the electrons respectively. This plasma will have a net charge-current density field $\mathbf{J} = en(\mathbf{v_i} - \mathbf{v_e})$ where $\mathbf{v_i}$ and $\mathbf{v_e}$ are the drift velocities of the two species. The momentum and energy for these combined species become

$$\begin{aligned} \partial_t(\rho\mathbf{U}) + \nabla\cdot\left(\rho\mathbf{U}\mathbf{U}^{\mathrm{T}} + \mathbf{P}\right) &= c^{-1}\mathbf{J}\times\mathbf{B} - \rho\nabla\phi \quad \text{(momentum)} \\ \partial_t(\rho e) + \nabla\cdot\left[(\rho e + p)\,\mathbf{U}\right] &= \mathbf{E}\cdot\mathbf{J} \qquad\qquad \text{(energy)} \end{aligned} \tag{1.5}$$

as the electric forces on the opposite charges cancel.

The above system of equations is under-determined so we need more assumptions to solve them. We can assume an equation of state for a reversible adiabatic (isentropic) process, the absence of magnetic monopoles, and the electric and magnetic fields can be related to the currents by a Maxwell's equation and a simple version of Ohm's law

$$\begin{aligned} (\gamma-1)\epsilon = p &\quad \text{(e.o.s.)} \\ \nabla\cdot\mathbf{B} = 0 &\quad \text{(no monopoles)} \\ \partial_t\mathbf{E} = c\nabla\times\mathbf{B} - 4\pi\mathbf{J} &\quad \text{(Ampère's law)} \\ \eta\mathbf{J} = \mathbf{E} + c^{-1}\mathbf{U}\times\mathbf{B} &\quad \text{(Ohm's law)} \end{aligned} \tag{1.6}$$

which we combine with the two simplifying assumptions that $\eta = 0$, i.e. that the electrical conductivity is infinite, and $\partial_t\mathbf{E} = 0$, which means that in astrophysical applications, the electric field variation is small compared to the curl of the magnetic field (Vietri, 2008), which helps to eliminate $\mathbf{J}$ and $\mathbf{E}$ from the system. In fact we can see from Ohm's law that in the ideal MHD limit of infinite conductivity and for non-relativistic fluid speeds, the electric field is much weaker than the magnetic field and can be neglected in comparison to it. The last equation may be deemed empirical but in Section 1.6.2, it will turn out from a generalised law derived from the momentum equation. It is worth noting that the restriction of $\eta = 0$ - as well as $\mu = 0$ for dynamic viscosity - in the context of numerical simulations is counter-acted by inherent numerical viscosity and dissipation.

The last ingredient is then to specify the governing laws for the magnetic field and the gravitational potential. Combining Faraday's law with Ohm's law and Ampère's law, we get:

$$\partial_t \mathbf{B} = -c\nabla \times \mathbf{E} = \nabla \times (\mathbf{U} \times \mathbf{B}) + \eta c \Delta \mathbf{B} \tag{1.7}$$

which called the induction equation that governs the time evolution of $\mathbf{B}$. The gravitational potential is simply determined by the Poisson equation

$$\Delta \phi = 4\pi G \rho \tag{1.8}$$

which can be solved for ϕ for a given matter distribution ρ. The above equations, 2 vector equations and 3 scalar equations in total are sufficient to solve for the unknowns ρ, $\mathbf{u}$, p, $\mathbf{B}$ and ϕ, but analytical solutions are possible only in very simple cases. In general, it requires the raw processing power of modern supercomputers to study the behaviour of a plasma governed even by the simplified ideal MHD equations.

1.4 The Reynolds number

We have so far assumed that the dynamic viscosity of our plasma is zero $\mu = 0$, meaning we have neglected any forces related to shearing stress when adjacent fluid layers flow in the same direction along the layer but at unequal velocities. Otherwise, Equation 1.3 should account for a momentum dissipation term and a transfer of energy. When the viscosity is non-zero, there is a shearing interaction between the layers, dragging them along in the same direction, in which case the flow is called laminar. An example of this can be seen in Figure 1.4, where the flame of a candle produces a plume whose lower half moves uniformly in a straight upright stream of hot air. However, as the gas rises, we find that the plume changes its shape completely and turns into countlessly many small sub-structures in curled, almost chaotic movement. This regime is called the turbulent flow and it is caused by a decrease of viscosity which according to Sutherland's formula is

$$\mu = a \frac{T^{3/2}}{T + b} \tag{1.9}$$

Figure 1.4: The plume from a candle will rise in a laminar flow at first, but become turbulent as the Reynolds number increases. Photo: Gary Settles (CC BY-SA 3.0).

so that, as the plume cools down, it becomes less viscous. To determine whether a certain viscosity level makes a flow laminar or turbulent, one has to relate it to the inertial forces. For this reason we determine the dimensionless Reynolds number

$$\mathrm{Re} = \frac{\rho U L}{\mu} \tag{1.10}$$

which is the ratio of inertial forces to viscous forces and therefore a measure of their relative importance for the flow. The laminar-turbulent transition happens at a critical Reynolds number which depends on the particular geometry of the problem.

1.4.1 Turbulence

Ich sage euch: man muss noch Chaos in sich haben,
um einen tanzenden Stern gebären zu können.

Also sprach Zarathustra (Friedrich Wilhelm Nietzsche)

A defining feature of turbulent flows are the swirling eddies that have different sizes and velocities. Larger eddies break up into successively smaller ones, transferring kinetic energy to shorter and shorter scales until they reach the scale at which viscosity dissipates them.

The problem of subsonic turbulence was analysed theoretically by Kolmogorov (1941) who proposed that for high enough Reynolds numbers, the characteristics are universal and isotropic since the length scale of the defining geometry is much larger than the eddy scales. Turbulence is then stirred on comparatively large forcing scales and sets an energy cascade through the intermediate inertial range down to the dissipating Kolmogorov length scale

$$l_\nu = \left(\frac{\nu^3}{\epsilon}\right)^{1/4} \tag{1.11}$$

where $\nu = \mu/\rho$ is the kinematic viscosity and ϵ is the energy dissipation rate. By dimensional analysis, Kolmogorov found that the kinetic energy spectrum $E(k)$ of any turbulent flow from the scale where turbulence is injected down to the dissipation scale must follow the relation

$$E(\epsilon, k) = C_\mathrm{K}\, \epsilon^{2/3}\, k^{-5/3} \tag{1.12}$$

with $k = 2\pi/l$ being the wavenumber for the length scale l, which has been well confirmed by laboratory and numerical experiments (Mathieu and Scott, 2000).

For a shock-dominated flow with high mach numbers $\mathcal{M} = U/c_\mathrm{s}$, where c_s is the sound speed, the above relations no longer hold. This regime is called Burgers turbulence (Burgers, 1950, 2013) and can be modeled by a series of discrete shocks treated as infinitesimally thin discontinuities in the velocity field (Girimaji and Zhou, 1995). Under these assumptions, the kinetic energy spectrum becomes

$$E(k) = C_\mathrm{B}\, k^{-2} \tag{1.13}$$

which is slightly steeper than in the Kolmogorov case.

1.5 Numerical simulations

"Forty-two," said Deep Thought, with infinite majesty and calm.
The Hitchhiker's Guide to the Galaxy (Douglas Adams)

With the exception of the induction equation for the magnetic field evolution and the Poisson equation for the gravitational potential, the rest of the ideal MHD equations (Equation 1.5) can be reshaped into the conservative form

$$\partial_t \mathbf{U} + \nabla \cdot \mathbf{F} = \mathbf{S} \tag{1.14}$$

where $\mathbf{U}$ is not the velocity but a generic vector of states, $\mathbf{F}$ is the corresponding flux tensor, and $\mathbf{S}$ are the source terms. We may compute a numerical solution[1] by solving the equations on a cartesian grid of cubic volumes or cells of size V. If we approximate the states of $\mathbf{U}$ linearly between each cell, this method will become second-order accurate. In a one-dimensional problem, the discretisation would look like

$$\frac{\mathrm{d}U_i}{\mathrm{d}t} + \frac{1}{\Delta x}\left[F\left(U_{i+1/2}\right) - F\left(U_{i-1/2}\right)\right] = 0 \tag{1.15}$$

where U_i are the states at the center of the i-th cell, $U_{i+1/2}$ the states at the boundary between the i-th and the $i+1$-th cell, and Δx is the cell length. Therefore, to solve this equation we have to compute the fluxes at the cell interfaces, which means solving a conservation law of piecewise constant values separated by discontinuities, also known as the Riemann problem. The solution to the above equation is not total-variation-diminishing (TVD) and will produce spurious oscillations, so we have to replace the states $U_{i+1/2}$ at the interfaces by slope-limited versions. This will essentially smooth out discontinuities such as shocks but ultimately helps in reducing oscillations.

[1] The concepts outlined in this section can only cover a brief outline of the techniques needed to successfully perform these numerical simulations. They have been implemented in the simulation code RAMSES (Teyssier, 2002) which was used to perform all the numerical studies presented in the following chapters.

In order to solve the induction equation in combination with the divergence-free constraint of the magnetic field, it is beneficial to treat the magnetic field separately on a staggered mesh, ie. each component on its perpendicular cell interface. Then the magnetic field components inside the cells can also be linearly reconstructed from their cell boundary values. The induction equation

$$\partial_t \mathbf{B} + \nabla \times \mathcal{E} = 0 \tag{1.16}$$

can then be solved with the constrained transport method (Evans and Hawley, 1988), which works in a similar fashion as before, but averages each magnetic field component over the face, making it a two-dimensional Riemann problem instead of a three-dimensional one. By using Stokes' theorem, this amounts to computing the the electromotive force $\mathcal{E}$ along the four edges around each face, and guarantees that the initial value of $\nabla \cdot \mathbf{B}$ is preserved. If we set up our initial conditions such that the magnetic field components are computed from a vector potential as

$$\mathbf{B} = \nabla \times \mathbf{A} \tag{1.17}$$

then we can ensure $\nabla \cdot \mathbf{B} = 0$ up to machine precision throughout the whole simulation.

To find the gravitational potential ϕ, the Poisson equation has to be solved separately, for example, at each half-time step. This can be done by the Gauss-Seidel relaxation method, which starts off by guessing a solution and then damps the residual

$$r = \Delta\phi - 4\pi G\rho \tag{1.18}$$

iteratively. Since this involves only a forward computation of the Laplace operator which is highly local, it can be implemented to run fast on massively parallel computer clusters, unlike Fast Fourier Transform methods, for example. The resulting force field $\mathbf{f} = -\nabla\phi$ must then be added to the momentum equation.

Finally, in the context of astrophysical studies we usually consider systems over very large scales where it is virtually impossible to cover all physical effects from the smallest up to the system scale. Therefore, it can be useful to employ sub-grid models to account for the effects

happening on scales smaller than the mesh size. In this way, we can follow the evolution of a large system such as a galaxy and still have a realistic representation of efficient cooling, star formation, supernova explosions and more. Stars and dark matter are modeled as a fluid of collisionless particles.

Any stable numerical scheme solving conservation equations needs artificial damping to suppress unphysical oscillations. For example, as mentioned before, in order to make the scheme above TVD, one needs to use slope limiters and flux limiters that smooth out the states and fluxes, which can make the solution locally less accurate. Effectively, this is is like adding artificial diffusion terms $\mu_{\rm N}\Delta\mathbf{U}$ and $\eta_{\rm N}\Delta\mathbf{B}$ to the momentum and induction equations, where $\mu_{\rm N}$ is the numerical viscosity and $\eta_{\rm N}$ is the numerical magnetic diffusion. In a simple first-order numerical scheme, they would scale linearly with the grid size and the velocities involved (Dullemond, 2008)

$$\mu_{\rm N} = \frac{\rho \Delta x u}{2} \tag{1.19}$$

but in the case of higher-order numerical schemes, there is no straightforward way of estimating them, since there is a strong dependence on the flow geometry. Considering the numerical viscosity term, one can also define a numerical Reynolds number

$$\mathrm{Re}_{\rm N} = \frac{\rho u L}{\mu_{\rm N}} \tag{1.20}$$

associated with the problem which is a measure of how well a numerical scheme can resolve turbulent motions. Ideally, it should always be larger than the physical Reynolds number to make realistic predictions. In the simple first-order case the numerical Reynolds number would just become $\mathrm{Re}_{\rm N} = 2L/\Delta x$, which illustrates that an increase of the numerical Reynolds number can be achieved by decreasing the grid size. In general, this shows that a good resolution is crucial for simulations of turbulent flows.

1.6 Seed fields

1.6.1 Primordial magnetic fields

de nihilo quoniam fieri nihil posse videmus.
De Rerum Natura II (Titus Lucretius Carus)

It is possible that the first magnetic fields in the Universe were formed at the earliest stages of its evolution. During the inflation period after the Big Bang, they could have been created if the conformal invariance of the electromagnetic field was broken (Turner and Widrow, 1988). This might have been the case if the electromagnetic field was coupled to the inflaton field or to curvature, or if the gauge invariance itself was broken (Durrer and Neronov, 2013). Other occasions for field generation arise during phase transitions such as the electroweak phase transition when the electromagnetic force decoupled from the weak force (Vachaspati, 1991), or primordial density perturbations in second-order perturbation theory (Ichiki et al., 2007). Traces of the primordial magnetic fields (PMF) created by any of these processes might still persist in the large-scale structure voids of the intergalactic medium. Their presence with a certain strength at the time of recombination will have also left an imprint in the cosmic microwave background (CMB). Recent measurements from Planck Collaboration et al. (2016a) constrain the upper limit of PMF in the CMB to 10^{-9} G (comoving) while Vovk et al. (2012) set lower limits on intergalactic fields between 10^{-18} G and 10^{-15} G.

1.6.2 Subsequent generation

Apart from primordial magnetic fields generated during the initial era of the Universe, other creation mechanisms working at any stage of its evolution are also viable. Ampère's circuital law tells us that any presence of net charge currents will induce a magnetic field loops around them. Such currents can arise in an ionised plasma when the positively-charged and ions and the negatively-charged electrons have a relative drift, which is facilitated by the fact that the proton-electron mass ratio is $m_p/m_e \approx 1836$ (Mohr et al., 2016).

This mass disparity causes electrons to be accelerated much faster than the ions even when the acting forces are equal. By multiplying by

their mass-ratio, subtracting the momentum equations of both species from one another, we can derive a generalised version of Ohm's law (Gurnett and Bhattacharjee, 2017) as

$$\begin{gathered}\mathbf{E}+c^{-1}\mathbf{U}\times\mathbf{B}-\eta\mathbf{J}= \\ \tfrac{1}{en}\mathbf{J}\times\mathbf{B}-\tfrac{1}{en}\nabla p_e+\tfrac{m_e}{ne^2}\left[\partial_t\mathbf{J}+\nabla\cdot\left(\mathbf{J}\mathbf{U}^{\mathrm{T}}+\mathbf{U}\mathbf{J}^{\mathrm{T}}\right)\right]\end{gathered} \tag{1.21}$$

with extra terms on the right-hand side which are usually neglected. In the case of zero magnetic fields however, Biermann (1950) illustrated that this will lead to

$$\partial_t\mathbf{B}=\frac{1}{en}\nabla T_e\times\nabla n \tag{1.22}$$

and therefore magnetic fields can be generated by density fluctuations which are perpendicular to the temperature gradients. This mechanism is called Biermann battery and can occur in shock fronts around supernovae, ionization fronts around stars, or possibly even be spontaneous fluctuations, and it will create small magnetic field strengths of $B\approx10^{-21}\,\mathrm{G}$ (Kulsrud et al., 1997, Gnedin et al., 2000, Schlickeiser, 2012). Similiarly, fluctuating magnetic fields can arise due to the Weibel instability in the plasma of protogalaxies (Lazar et al., 2009), when momentum anisotropies are present.

Magnetic fields generated in stars by a stellar dynamo are locally very strong, but their spatial extension is small compared to galactic scales. Nevertheless, stellar winds and supernova outbursts are able carry them into interstellar space where they become diluted, but may retain considerable strength. If we consider a red supergiant star with a moderate size of $R=100\,\mathrm{R}_\odot$ and a typical surface magnetic field of $B_\mathrm{s}=1\,\mathrm{G}$ Tessore et al. (2017) blasting its shell out to $L=10\,\mathrm{pc}$, it will leave a trace with field strengths of

$$B_\mathrm{t}=\left(\frac{R}{L}\right)^2\,\mathrm{G}\approx10^{-14}\,\mathrm{G} \tag{1.23}$$

on that spatial scale. These numbers may be varied. Analogously, we may conclude that AGN jets may provide powerful methods to carry magnetic fields into the intergalactic medium (Bisnovatyi-Kogan et al., 1973, Rees, 2005).

1.7 Dynamo theory

causarum enim cognitio cognitionem eventorum facit.
Topica (Marcus Tullius Cicero)

The magnetic seed fields discussed in Section 1.6 are all considerably weaker than what we can see in observational data. It can be seen from the induction equation that it is possible to increase the total magnetic energy in the system by doing work against Lorentz force (or by a Poynting flux through the system boundaries). However, for a plasma flow to do this efficiently it has to show certain properties. Cowling (1934) argued that no axisymmetric flow can maintain a magnetic field against dissipation, which became known as the Cowling anti-dynamo theorem. Similar anti-dynamo theorems show that any presence of a high degree of symmetry will break dynamo action. In particular, the system's flow velocity field $\mathbf{u}(x, y, z, t)$ must depend on more than two variables (Childress and Gilbert, 2008), thus any two-dimensional steady flow will be unable to generate a dynamo.

Vaĭnshteĭn and Zel'dovich (1972) introduced the distinction between *fast* and *slow* dynamos by their dependence on the Ohmic dissipation η. While slow dynamos have a dynamo growth rate $\gamma \propto \eta^{\alpha}$ for some $\alpha > 0$, where

$$B \propto \exp(\gamma t) \tag{1.24}$$

depends on the growth rate γ, this growth rate is independent of the Ohmic dissipation rate η for fast dynamos, i.e. $\alpha = 0$. In particular, fast dynamos can also operate in the ideal MHD limit where the Ohmic dissipation is zero, while slow dynamos will not work in this regime as γ approaches zero.

1.7.1 The fast dynamo

Practically all dynamo mechanisms relevant in astrophysical applications are fast dynamos (Brandenburg et al., 2012). The Stretch-Twist-Fold mechanism (Vaĭnshteĭn and Zel'dovich, 1972) is a very intuitive way of envisioning how magnetic field lines may be amplified in a suitable plasma flow condition. Figure 1.5 illustrates how a closed magnetic field loop is stretched, twisted, and folded onto itself. If

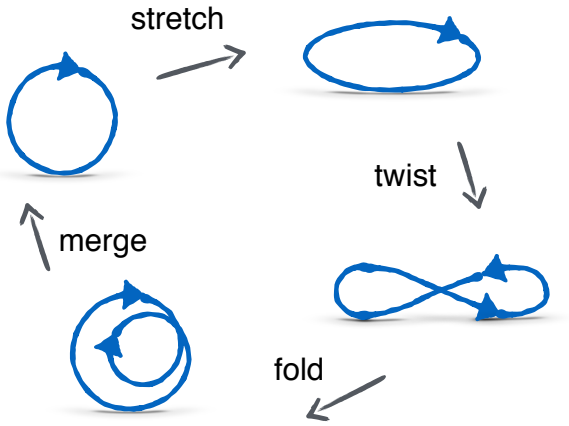

Figure 1.5: Stretch - Twist - Fold: Magnetic field loops following the plasma flow can become stretched and then twisted. If the twisted loop is then folded back, its field lines can reconnect to a stronger loop due to a finite resistivity.

there is finite resistivity, it will make the double-loop reconnect itself and create a single stronger loop, but this is not necessary to sustain the dynamo (Brandenburg and Subramanian, 2005). It becomes evident that there must be shear to do the stretching, as well as a perpendicular twisting and folding motions, so the required plasma flow may appear very complex.

The group of fast dynamos can be further divided in *large-scale* dynamos which produce magnetic fields which are ordered on scales larger than the flow scale, and *small-scale* dynamos where the generated field lines are fluctuating incoherently. The most prominent theory for large-scale dynamos is given by the mean-field approach, where the velocity field and the magnetic field are decomposed into averaged components and fluctuating components $\mathbf{U} = \overline{\mathbf{U}} + \mathbf{u}$ and $\mathbf{B} = \overline{\mathbf{B}} + \mathbf{b}$ where the average can either be an ensemble average or some kind of spatial average. The modified induction equation for the mean magnetic field then becomes

$$\partial_t \overline{\mathbf{B}} = \nabla \times \left(\overline{\mathbf{U}} \times \overline{\mathbf{B}} - \eta \overline{\mathbf{J}} + \overline{\mathcal{E}} \right) \tag{1.25}$$

with a mean electromotive force $\overline{\mathcal{E}} = \overline{\mathbf{u} \times \mathbf{b}}$ depending on the small-

scale components of velocity and magnetic field. This type of dynamo has long been of interest in the research on galactic magnetic fields because observations of the Milky Way as well as nearby spiral galaxies showed large ordered fields. Naturally, this seemed a good candidate to produce these kinds of fields, although they require certain flow conditions, such as magnetic helicity and shearing motions, to work.

1.7.2 The small-scale dynamo

More recently, however, more attention has been given to small-scale dynamos as they are more generic in terms of flow requirements and exhibit much faster magnetic field growth, since their amplification time scales are of the order of the smallest turbulent eddy turnover time scale. This is important because they allow field amplification even in galaxy clusters or elliptical galaxies (Brandenburg and Subramanian, 2005), and they can explain strong magnetic fields in high-redshift galaxies when the Universe was much younger and large-scale dynamo amplification times were not sufficient.

Assuming a turbulent velocity field $\mathbf{v}$ with an isotropic and homogeneous Gaussian random distribution and δ-correlation in time, Kazantsev (1968) used the two-point correlation function

$$M_{ij}(r,t) = \langle B_i(\mathbf{x},t) B_j(\mathbf{y},t) \rangle \tag{1.26}$$

to derive a differential equation for it which has exponentially growing solutions, which laid the foundation for what became known as Kazantsev theory. Under the same assumptions, Kulsrud and Anderson (1992) found that for a Kolmogorov kinetic energy spectrum the magnetic energy spectrum produced by this dynamo will scale with the wave number as $k^{3/2}$ for scales larger than the resistive scale, and that the amplification time is comparable to the turnover time of the shortest eddy. Using the Wentzel-Kramers-Brillouin (WKB) approximation on Kazantsev's equation, Schober et al. (2015) analysed its behaviour as the magnetic field becomes stronger and approaches saturation. They considered the limits of very small and very large magnetic Prandtl numbers found that the dynamo growth rate scales with the magnetic and kinetic Reynolds numbers, respectively. Their results show that this type of dynamo will saturate between 0.1% and

50% of turbulent equipartition, depending on $\mathrm{Pr_M}$, the Mach number and the model of turbulence.

1.8 A brief history of galaxies

'Bring action hither, this cannot go to war:
A stirring dwarf we do allowance give
Before a sleeping giant.' Tell him so.

Troilus and Cressida (William Shakespeare)

The hierarchical scenario in the Λ-CDM paradigm assumes that structures grew from initially small-scale perturbations in the density field, as matter became condensed under its own gravitation and subsequently collapsed into small halos. These are believed to be the hosting sites for the formation of protogalaxies and of the first stars which were very massive Population III stars. These first galaxies, due to the lower mass, are strongly affected by stellar feedback, which is very efficient in driving turbulence. In particular, radiation pressure driven winds and supernovae explosions can affect star formation and increase the ISM inhomogeneity (Wise et al., 2012, Brook et al., 2012).

According to the hierarchical formation scenario (White and Frenk, 1991, Cole et al., 2000), the leading mechanism in galaxy formation is galaxy merging and accretion of smaller systems. Indeed, at high redshift galaxies are expected to experience subsequent violent interactions, eventually building up more massive stable structures. Mergers of lower-mass galaxies are considered rarer due to the low observational evidence. An outstanding case, on the other hand, is a satellite galaxy of Andromeda, Andromeda II, which is thought to be the remnant of an old merger of two dwarf galaxies (Amorisco et al., 2014). The galaxy merging rate is estimated to depend on the redshift as $(1+z)^m$, with $1 < m < 3$ Lotz et al. (2011), however most observations these estimates are based on are at low redshift (z<1.5), hence this linear dependence could have a turn-off at some point.

In the later stages of evolution, gas accretion and dynamical encounters are limited, which determines the establishment of a more quiescent phase, where turbulence progressively decreases. The timescale over which turbulence is dissipated can be estimated from the

Kolmogorov's energy flow through the eddie scale and it turns out to be about a crossing time (Klessen and Glover, 2016), which amounts to 1 Gyr for a dwarf galaxy like the ones that we are going to consider.

All in all, the emergent picture is that as the first galaxies formed and evolved, assembling to larger and larger objects. At the same time, they underwent very active phases with strong turbulence that eventually decayed as they 'settled down'. This turbulence may have been a strong driver of dynamo action which amplified magnetic fields. Thus, galactic magnetic fields are closely connected to the evolution of their host galaxy.

2 Small-scale dynamo amplification

Und jedem Anfang wohnt ein Zauber inne
Das Glasperlenspiel (Hermann Hesse)

In this chapter[1], we will investigate the particular role played by feedback mechanisms in creating strong fluid turbulence, allowing for a magnetic dynamo to emerge. Performing magnetohydrodynamic simulations of isolated cooling gas halos, we compare the magnetic field evolution for various initial field topologies and various stellar feedback mechanisms. We find that feedback can indeed drive strong gas turbulence and dynamo action. We see typical properties of Kolmogorov turbulence with a $k^{-5/3}$ kinetic energy spectrum, as well as a small-scale dynamo, with a $k^{3/2}$ magnetic energy spectrum predicted by Kazantsev dynamo theory. We also investigate simulations with a final quiescent phase. As turbulence decreases, the galactic fountain settles into a thin, rotationally supported disk. The magnetic field develops a large-scale, well-ordered structure with even symmetry, which is in good agreement with magnetic field observations of nearby spirals. Our findings suggest that weak initial seed fields were first amplified by a small-scale dynamo during a violent, feedback-dominated early phase in the galaxy formation history, followed by a more quiescent evolution, where the fields have slowly decayed or were maintained via large-scale dynamo action.

[1]The work presented in this chapter has been published in the *Monthly Notices of the Royal Astronomical Society*, Volume 457, Issue 2 under the title 'A small-scale dynamo in feedback-dominated galaxies as the origin of cosmic magnetic fields - I. The kinematic phase', following peer-review (Rieder and Teyssier, 2016). It was also presented at the XXIX General Assembly of the International Astronomical Union in Honolulu, Hawaii, USA in August 2015.

2.1 Introduction

Large-scale magnetic fields are measured with strengths of up to several μG in nearby galaxies (Beck et al., 1996), and possibly even higher field strength have been detected in earlier galaxies at high redshift (Bernet et al., 2008). The preferred theory to explain their origin is based on the early generation of seed fields at the epoch of cosmic re-ionisation, through the microscopic process known as 'Biermann battery' (Biermann, 1950, Naoz and Narayan, 2013), later amplified during the galaxy formation era, through the large-scale galactic dynamo process (Parker, 1970, Brandenburg and Subramanian, 2005). The Biermann battery is likely to generate fields at the level of 10^{-20} G, leaving to the galactic dynamo process more than 14 orders of magnitude of field amplification during the 10 Gyr of cosmic evolution. The challenge for galactic dynamos is even more severe, if one considers that strong fields are already in place at high redshift (Widrow, 2002), and are probably even stronger than they are today (Bernet et al., 2008).

Successful theoretical models for large-scale galactic dynamos report exponential growth rates of the order of $\Gamma \simeq 0.01$ to 0.1Ω, where Ω is the galactic disk rotation rate (Pariev et al., 2007). For typical, present day spirals, this translates into e-folding amplification time scale of roughly 1 Gyr, making the task of amplifying the field over 14 orders of magnitude virtually impossible. One noticeable exception is the cosmic-ray-driven dynamo proposed by Parker (1992) and simulated by Hanasz et al. (2004), leading to a measured growth rate $\Gamma \simeq \Omega$, although the numerical experiment was performed over only a relatively limited time, since the reported magnetic field amplification was over only 3 orders of magnitude (Hanasz et al., 2004). On the theoretical side, classical mean field dynamos are plagued by the catastrophic α-quenching effect, leading to very low saturated values for the large-scale magnetic field (Kulsrud and Anderson, 1992, Vainshtein and Cattaneo, 1992), owing to the strict conservation of magnetic helicity in a closed system. A possible solution to this problem is the effect of galactic winds, that could drag the magnetic field lines outside of the dynamo-active disk, therefore alleviating the aforementioned quenching issue (Del Sordo et al., 2013).

The theory of galaxy formation has significantly evolved over the

past decade, with the ever increasing role of feedback processes (Scannapieco et al., 2012) and their associated galactic winds (Oppenheimer and Davé, 2006), together with the dominant accretion mechanism through cold streams (Kereš et al., 2005, Ocvirk et al., 2008, Dekel et al., 2009). On the observational side, galactic winds are indeed ubiquitous in star bursting local galaxies (Martin, 1999), but also in many "normal" high redshift galaxies (Steidel et al., 2010). One of the most spectacular observational constraints on galaxy formation theories was obtained by matching the stellar mass of the central galaxies to their parent halo mass (Behroozi et al., 2013, Moster et al., 2013). This has led theorists to consider much stronger feedback processes, in order to regulate star formation throughout cosmic time, especially at high redshift, when the star formation efficiency was so low (Agertz et al., 2013, Hopkins et al., 2014, Roškar et al., 2014, Wang et al., 2015).

In this rather violent, feedback-dominated scenario, dwarf galaxies play a very important role. They are the dominant galaxy population at high redshift, probably responsible for the cosmic re-ionisation (Kimm and Cen, 2014). They are also the progenitors of the Milky Way satellites, which are useful laboratories to test our current galaxy formation paradigm. For the latter, violent feedback mechanisms have also been invoked to explain the absence of cusp in the dark matter density profile, and the presence of a dark matter core in low surface brightness galaxies (de Blok et al., 2001). Cosmological simulations of dwarf galaxies have been performed with strong feedback recipes, confirming in this case the formation of a dark matter core (Governato et al., 2010, 2012). Recently, we have also performed idealised simulations of an isolated, cooling gaseous dwarf halo, obtaining, in this well-controlled numerical experiment, the formation of a dark matter core (Teyssier et al., 2013). The dark matter core formation mechanism is now well understood (Pontzen and Governato, 2012). It is due to repeated, energetic feedback events due to many supernovae explosions, leading to violent oscillations of the gravitational potential, due to the large gas mass variations within the central kilo parsec of the galaxy. A possible observational signature of this effects is a typical, oscillatory star formation history, mimicking a breathing mode in the gas distribution (Kauffmann, 2014).

In this chapter, we want to study the impact of a strong feedback scenario on the growth of magnetic fields in dwarf, as well as in larger

galaxies. The velocity field on both small and large scales, resulting from repeated giant feedback events, can have a direct influence on the growth of the magnetic energy. Indeed, supernovae explosions in the Milky Way have been considered for quite a long time as a source of helical gas motions, promoting a large-scale α-dynamo in the Galaxy (Ferriere, 1992). The Milky Way is however a rather quiescent galaxy, with moderate supernovae activity. Here, we are considering feedback-dominated galaxies, with high star formation rates and violent turbulent motions, together with large-scale galactic fountains or winds.

Several simulations including magnetic fields have been performed recently in the context of galaxy formation (Wang and Abel, 2009, Dubois and Teyssier, 2010). These simulations, based on the popular "cooling halo" numerical set-up, have achieved only moderate magnetic field amplification. The important property of these simulations is the absence of feedback (Wang and Abel, 2009), or the relative weakness of the feedback recipe used at that time (Dubois and Teyssier, 2010).

A first exception is the simulation reported in Beck et al. (2012), based on a MHD version of the SPH code GADGET with divergence cleaning. They observed a fast exponential growth of the magnetic field, which they attribute to a small-scale dynamo. Feedback processes were included through an effective Equation-of-State (EoS), without any explicit source of turbulence in these relatively smooth, thermally-supported flows. These authors however reported very strong growth rates, with e-folding times as small as 10 Myr, although analytical estimates based on small-scale dynamo theory predicted e-folding times closer to 100 Myr.

A second exception is the recent simulation reported in Pakmor and Springel (2013), using the new Magneto-Hydrodynamics (MHD) solver developed for the AREPO code (Pakmor et al., 2011), where strong magnetic field amplification has also been observed, although, here again, stellar feedback effects were not considered explicitly, but only indirectly as a modified thermal EoS, leading to the formation of relatively smooth, two-dimensional flows, in which dynamo amplification is in principle notoriously difficult to obtain.

In this chapter, we will use a similar set-up as in all those previous studies, namely a cooling isolated gaseous halo, considering simula-

tions with (but also without) strong stellar feedback. We will use the Adaptive Mesh Refinement code RAMSES (Teyssier, 2002), adopting the 'Constrained Transport', strictly divergence-free-preserving, MHD solver presented in Teyssier et al. (2006) and in Fromang et al. (2006). The chapter is organised as follows: In Section 2.2, we will present our numerical methods, both in terms of galaxy formation physics and magnetic field modelling. In Section 2.3, we describe our initial conditions for the isolated, *magnetised* cooling halo. In Section 2.4, we present our main results, outlining the difference between the feedback and the no-feedback cases. Finally, in Section 2.5, we discuss the implications of our results in the context of galactic dynamo theory, as well as possible further studies to confirm and broaden our findings.

2.2 Numerical methods

We have performed MHD simulations of isolated, cooling haloes, using the Adaptive Mesh Refinement (AMR) code RAMSES (Teyssier, 2002). These simulations feature a collisionless fluid (for dark matter and stars) and a magnetised gaseous component, coupled through gravity. In this section, we describe the simulation technique used to follow the evolution of our isolated halo. First, we describe in details our AMR implementation for solving the ideal MHD equations, together with simple test cases to show that it works as intended in the context of galactic dynamo. We then describe the adopted galaxy formation physics, such as gas cooling, metal enrichment, star formation and stellar feedback, leading to what we believe to be a realistic model of the interstellar medium (ISM).

2.2.1 Ideal MHD solver

The equations that we solve are the ideal MHD equations (written here without gravity and cooling source terms for the sake of simplicity)

$$\partial_t \rho + \nabla \cdot (\rho \mathbf{u}) = 0 \tag{2.1}$$

$$\partial_t (\rho \mathbf{u}) + \nabla \cdot (\rho \mathbf{u}\mathbf{u}^T - \mathbf{B}\mathbf{B}^T + P_{\rm tot}) = 0 \tag{2.2}$$

$$\partial_t E + \nabla \cdot [(E + P_{\rm tot})\mathbf{u} - (\mathbf{u} \cdot \mathbf{B})\mathbf{B}] = 0 \tag{2.3}$$

$$\partial_t \mathbf{B} - \nabla \times (\mathbf{u} \times \mathbf{B}) = 0 \tag{2.4}$$

where ρ is the gas density, $\rho\mathbf{u}$ is the momentum, $\mathbf{B}$ is the magnetic field, $E = \frac{1}{2}\rho\mathbf{u}^2 + \varepsilon + \frac{1}{2}\mathbf{B}^2$ is the total energy, and ε is the internal energy. The total pressure is given by $P_{tot} = P + \frac{1}{2}\mathbf{B}^2$ where we assume a perfect gas equation of state $P = (\gamma - 1)\varepsilon$. The system of equations is completed by the soloinoidal constraint

$$\nabla \cdot \mathbf{B} = 0. \tag{2.5}$$

The code is grid-based with a tree-based adaptively refined mesh. The equations are solved using the second-order unsplit Godunov scheme based on the MUSCL-Hancock method. We chose the HLLD Riemann solver with the MinMod slope limiter for the hydro variables which are cell-centred. The magnetic field on the other hand is treated as a face-centered variable. This allows the use of the Constrained Transport (CT) method to advance the induction equation (Equation 2.4) in time, which preserves the divergence of the magnetic field to the numerical precision level (Teyssier et al., 2006). The CT method involves a spatial interpolation of the EMF on the cell edges for the predictor step and solving a 2D Riemann problem for the corrector step. For the 2D problem, we use the HLLD solver as well and for the magnetic field in general, the MonCen slope limiter.

Boundary conditions were chosen to allow for free outflow. For the 5 hydro variables, this is done by imposing a vanishing gradient at the domain boundary (zero-gradient method). The same can be applied to the transverse magnetic field component parallel to the boundary face $B_{\parallel}$, but would cause a non-zero divergence of the magnetic field if applied to the normal component $B_{\perp}$ which is perpendicular to the face. Instead, we use a linear interpolation for $B_{\perp}$ so that $\nabla \cdot \mathbf{B} = 0$. Note that this method can cause an inward Poynting flux which transports magnetic energy from the outside into the computational domain. Since the magnetic field at the border is many orders of magnitude weaker than the average, this does not contribute significantly to the overall magnetic energy evolution (see Dubois and Teyssier, 2010).

Special care needs to be taken also when refining and de-refining cells, in order to enforce the $\nabla \cdot \mathbf{B} = 0$ constraint, when interpolating the magnetic field. A solution to this problem within the CT framework has been proposed by Balsara (2001) and Tóth and Roe (2002), and we adopt it here for newly refined cells, but also for temporary

ghost cells used to set proper boundary conditions at coarse-fine level boundaries.

In the context of galactic dynamos, it is worth mentioning that our code has been tested extensively against well-known flows triggering fast dynamos, such as in the ABC flow (Galloway and Frisch, 1986, Childress and Gilbert, 2008) or in the Ponomarenko dynamo (Ponomarenko, 1973). We have shown in Teyssier et al. (2006) that our numerical scheme for the ideal MHD equations was in fact slightly resistive, with, for a regular Cartesian grid, a numerical magnetic Reynolds number roughly inversely proportional to the square of the number of grid points per box length. This scaling is to be expected for second-order schemes and smooth flows. In the context of AMR and highly complex, turbulent flows, determining the exact effective numerical Reynolds number of the simulated flow is impossible. Qualitatively, though, it is important to bear in mind that magnetic reconnection and other diffusive processes occur in the simulation at a typical scale probably very close to the grid scale. This scale plays a very important role in dissipating the kinetic energy of the turbulence, and also controls the magnetic energy losses due to reconnection or (numerical) Ohmic dissipation.

2.2.2 Cooling and star formation

In addition to solving the ideal, self-gravitating MHD equations, we also include many physical processes relevant to galaxy formation. One of the key physical ingredient is gas cooling, which leads the hot, initially hydrostatic halo gas to loose pressure support and to condense in the centre as a centrifugally supported disc. When this atomic gas of 10^4 K is allowed to cool even more due to fine-structure metal line cooling or molecular cooling, the disc fragments into dense clumps, leading to the formation of a turbulent, multiphase medium. To model gas cooling, we use standard H and He cooling processes with an additional contribution from metals based on Sutherland and Dopita (1993) for temperatures above 10^4 K and metal fine-structure cooling below 10^4 K, as in Rosen et al. (1995). The metallicity, denoted as Z, is modelled as a passive scalar, representing the mass fraction of atoms heavier than Helium in the gas. It is initialised to $Z_{\rm ini} = 0.05 Z_\odot$ in the halo, mimicking molecular Hydrogen cooling in a zero

metallicity gas. The metallicity is increased further by supernova feedback events, using a metal yield of $y = 0.1$.

Our refinement strategy is based on a quasi-Lagrangian approach: each cell is refined if it contains more than 8 dark matter particles or if its baryonic mass (including gas and star particle mass) exceeds $8 \times m_{\rm res}$, where $m_{\rm res}$ is the adopted mass resolution of the simulation. Refinement are performed recursively, on a cell–by–cell basis, until the adopted maximum level of refinement is reached (noted $\ell_{\rm max}$). It is crucial for astrophysical simulations to resolve spatially the Jeans length (Truelove et al., 1997). Requiring that the Jeans mass is resolved by at least 64 mass resolution elements, $M_{\rm J} = 64 m_{\rm res}$, and adopting a realistic minimum temperature for the gas, noted $T_{\rm J}$, one can compute the corresponding Jeans length, and require it to be resolved by 4 cells, $\lambda_{\rm J} = 4\Delta x_{\rm min}$. We can then determine the maximum required level of refinement corresponding to the adopted mass resolution $m_{\rm res}$. To prevent the gas from accumulating and locally violating the Jeans length criterion, we also add an artificial pressure floor,

$$P_J = (4\Delta x_{\rm min})^2 \frac{G}{\pi\gamma}\rho^2 \tag{2.6}$$

so that the gas density will never significantly exceed a typical value $n_{\rm J}$ given by the relation $k_{\rm B}T_{\rm J} = P_{\rm J}(n_{\rm J})/n_{\rm J}$.

Stars are treated as collisionless particles which are created stochastically from the gas according to a Schmidt law (as in Rasera and Teyssier, 2006)

$$\dot{\rho}_* = \epsilon_* \frac{\rho_{\rm gas}}{t_{\rm ff}} \tag{2.7}$$

if the local density $\rho_{\rm gas}$ is above a threshold density $\rho_* = n_* \, {\rm m_H}$. We always choose the star formation threshold density to be equal to the previously defined Jeans density $n_{\rm J}$. The star formation efficiency per free-fall time is always set to $\epsilon_* = 0.01$; this value is based on observations of nearby molecular clouds (Krumholz and Tan, 2007). Creation of stellar particles is a local random Poisson process with Poisson parameter $\lambda = \rho_* \Delta x^3 \Delta t / m_*$ where Δt is the simulation time-step and

$$m_* = n_* \left(\Delta x_{\rm min}\right)^3 \tag{2.8}$$

the mass of the resulting stellar particle, which is equal to the smallest cell mass at the density threshold. For each simulation, precise numbers for all these parameters are given in Table 2.1.

2.2.3 Stellar feedback

In this study, we explore the consequences of strong feedback scenarios on the amplification of the magnetic field in dwarf and Milky-Way-sized galaxies. The proper modelling of stellar feedback mechanisms, such as supernovae explosions, photo-ionised bubbles or infrared radiation in dusty environment is subject to intensive research throughout the ISM and galaxy formation literature. Understanding in details these various processes goes far beyond the scope of this work. Our goal is merely to use various phenomenological recipes to model such feedback mechanisms very crudely, and produce dynamical properties that we believe are relevant for high-redshift galaxies, the most important one being the gas velocity field, highly turbulent, explosive and fountain-like, which could result in a fast magnetic dynamo.

Supernovae feedback

For this purpose, we used a numerical model for supernovae feedback developed in the context of dwarf galaxies evolution, and that turned out to lead to the formation of a dark matter core (Teyssier et al., 2013). The main ingredient is the use of a non-thermal energy variable, and its associated pressure, treated as a passively advected scalar quantity $e_{\rm turb} = \rho\epsilon_{\rm turb}$, which represents various small-scale, non-thermal energies released by supernovae (e.g. turbulence, magnetic fields or cosmic rays). The evolution of this non-thermal energy is specified by

$$\rho\frac{D\epsilon_{\rm turb}}{Dt} = \dot{E}_{\rm inj} - \frac{\rho\epsilon_{\rm turb}}{t_{\rm diss}}. \tag{2.9}$$

where the dissipation time scale is fixed to $t_{\rm diss} = 20$ Myr and the energy injection per supernovae is set by

$$\dot{E}_{\rm inj} = \dot{\rho}_*\eta_{\rm SN}\cdot 10^{50}\,{\rm erg/M_\odot} \tag{2.10}$$

where the mass fraction in massive stars is set to $\eta_{\rm SN} = 0.1$ and the local star formation rate $\dot{\rho}_*$ is set by our adopted Schmidt law. For details about the implementation, we refer to Teyssier et al. (2013)

Radiation feedback

Because supernovae are probably not energetic enough to trigger strong winds in Milky-Way-sized galaxies, it has been proposed recently to consider stellar radiation as an additional feedback mechanism (Murray et al., 2010). Interstellar dust indeed absorbs UV photons, much of it being subsequently re-emitted as thermal radiation in the infrared band. This radiation will transfer momentum to the gas through radiation pressure (Murray et al., 2010, Hopkins et al., 2012, Agertz et al., 2013, Roškar et al., 2014) We consider radiation feedback only for Milky-Way-sized galaxy simulations. We use here again a very crude model to capture the energy from the stellar UV radiation, using a simple escape probability model as

$$E_{\rm UV} = E_{\rm rad}\left[1 - \exp(-\kappa_{\rm UV}\rho_{\rm dust}\Delta x)\right] \tag{2.11}$$

with the dust mass density is assumed to be $\rho_{\rm dust} = Z\rho_{\rm gas}$ (here, Z denotes the gas metallicity). The dust opacity at $0.1\,\mu{\rm m}$ is taken to be $\kappa_{\rm UV} = 1000\,{\rm cm}^2/{\rm g}$ (Draine and Li, 2007), and the total energy released during the first 10 Myr of a $10\,{\rm M}_\odot$ progenitor $E_{\rm rad} = 10^{52}\,{\rm erg}/{\rm M}_\odot$. The same cell is then assumed to absorb the energy in the infrared

$$E_{\rm IR} = E_{\rm UV}\left[1 - \exp(-\kappa_{\rm IR}\rho_{\rm dust}\Delta x)\right] \tag{2.12}$$

where $\kappa_{\rm IR}$ is the dust opacity in the IR band, which is a free parameter in our feedback implementation, usually around 10 ${\rm cm}^2/{\rm g}$ (Draine and Li, 2007, Semenov et al., 2003). The energy $E_{\rm IR}$ is added in the non-thermal energy equation for $\dot{E}_{\rm inj}$ in the supernova feedback so that it contributes to $\epsilon_{\rm turb}$. Details about the implementation can be found in Roškar et al. (2014). Here again, we would like to stress that our goal is not to study in great details realistic feedback mechanisms, but rather to generate galactic velocity fields in qualitative agreement with high-redshift galaxies and their associated strong outflows, in the context of galactic dynamos.

2.3 Initial conditions

We have performed a series of non-cosmological simulations of isolated halos in hydrostatic equilibrium, varying the initial set-up with two different halo sizes (a typical dwarf and a typical Milky-Way) and two different initial magnetic field topologies (dipole and quadrupole), in addition to the various options for stellar feedback that we have discussed in the previous section. We will now describe more precisely our initial set-up, and a summary of the various run parameters is given in Table 2.2. We refer the interested reader to Teyssier et al. (2013) for a more detailed analysis of the non-magnetohydrodynamic properties in the dwarf halo case.

2.3.1 Initial halo

Our initial halo follows a Navarro et al. (1997) (hereafter NFW) density profile with a concentration parameter $c = 10$. The smaller of the two halos, representative of a typical dwarf galaxy (we use the acronym DW), has a circular velocity of $V_{200} = 35\,\mathrm{km/s}$ and a virial mass of $M_{200} = 1.4 \times 10^{10}\,\mathrm{M_\odot}$, both measured at the virial radius $R_{200} = 50\,\mathrm{kpc}$. The halo is truncated at $112.5\,\mathrm{kpc}$, resulting in the total enclosed mass of $2 \times 10^{10}\,\mathrm{M_\odot}$. This is essentially the same set of parameters we used in the hydrodynamic simulations of Dubois and Teyssier (2010) and Teyssier et al. (2013).

The larger halo is chosen to be a typical Milky Way galaxy (we use the acronym MW), where we increased the circular velocity to $V_{200} = 160\,\mathrm{km/s}$, corresponding to a virial radius of $R_{200} = 230\,\mathrm{kpc}$ and a virial mass of $M_{200} = 1.3 \times 10^{12}\,\mathrm{M_\odot}$. It is truncated at $514\,\mathrm{kpc}$, resulting in the total enclosed mass of $2 \times 10^{12}\,\mathrm{M_\odot}$.

In all other aspects, both initial configurations follow the same prescription as in Teyssier et al. (2013). We consider a gas fraction equal to the universal mean value $f_{\mathrm{gas}} = 15\%$, and the gas density is also following a NFW profile. The gas temperature is initialised by solving the hydrostatic equilibrium equation. The gaseous halo is set in slow rotation around the z-axis, using the angular momentum profile from cosmological simulations and a spin parameter $\lambda = 0.04$. The dark matter halo is sampled by 10^6 dark matter particles, whose initial positions and velocities were computed with the density-

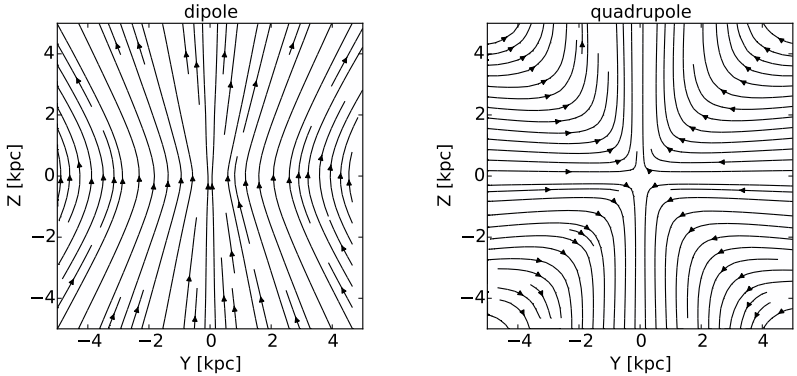

Figure 2.1: Streamlines of the magnetic field for the two topologies used in the initial conditions. The left panel shows the dipole with mid plane symmetry of the vertical component and mid plane antisymmetry of the radial component, while the right panel shows the quadrupole field topology with opposite symmetries.

potential pair approach of Kazantzidis et al. (2004) and Read et al. (2006). The stability of the resulting gas-dark matter equilibrium was shown in Teyssier et al. (2013) to be sufficiently good for our present purpose.

2.3.2 Initial magnetic field

A fundamental ingredient in any MHD simulation is the adopted initial magnetic field configuration. The simplest possible choice would be a constant field parallel to one direction, e.g. a vertical uniform field

$$\mathbf{B}_{\rm initial} = \begin{pmatrix} 0 \\ 0 \\ B_0 \end{pmatrix} . \tag{2.13}$$

However, we argue here that this choice is not appropriate for initially concentrated mass distributions in general and for cosmological halos in particular. This simple choice results indeed in a completely uniform magnetic energy distribution. As collapse proceeds, because of

the initially peaked density distribution, less and less mass is added to the central galaxy, especially at late time. Magnetic energy, however, is still being accreted efficiently, even at late time, and artificially added to the central object. We believe it is more appropriate, in the context of ideal MHD (frozen-in magnetic flux), to consider that the initial magnetic energy follows closely the initial density distribution, in which case the magnitude of the field would scale roughly as

$$\|\mathbf{B}\| \propto \rho^{2/3} \tag{2.14}$$

This requirement translates into a more complex field topology, and we need to work harder to initialise the field, compared to the uniform, vertical field case. Another important property of galactic dynamos is the field parity with respect to the system's mid-plane. To explore possible effects related to the direction of the vector field, with odd or even parity across the mid plane, we consider initially two typical topologies: dipole-like or quadrupole-like. The dipole-like field (we use the acronym D) is defined using the following vector potential

$$\mathbf{A}_{\mathrm{D}} = B_0 \left[\frac{\rho(r,z)}{\rho_0}\right]^{2/3} r\mathbf{e}_\phi \tag{2.15}$$

where $\rho(r,z)$ is the initial gas density given by the NFW profile and $\mathbf{e}_\phi$ is the unit vector along the toroidal direction. Note that here, coordinates are given in a cylindrical coordinate system centered around the halo center and aligned with the rotation axis. The corresponding magnetic field has a vertical component which is symmetric with respect to the mid plane, while its radial component is antisymmetric. The quadrupole field (we use the acronym Q) is defined using the vector potential

$$\mathbf{A}_{\mathrm{Q}} = B_0 \left[\frac{\rho(r,z)}{\rho_0}\right]^{2/3} z\,\mathbf{e}_\phi \tag{2.16}$$

and has the reversed symmetries. Its vertical component is antisymmetric and its radial component is symmetric with respect to the mid plane. Figure 2.1 illustrates the shape of the two vector fields. Note that in both cases, the initial field strength follows a profile peaked around the center with magnitude roughly proportional to $\rho^{2/3}$, as

expected. The magnetic field is then initialised on each cell face of the AMR grid, using a finite-difference approximation of the curl:

$$\mathbf{B}_{\rm initial} = \nabla \times \mathbf{A} \tag{2.17}$$

This ensures that the divergence of the magnetic field is initially exactly zero (to machine precision), and, thanks to the Constrained Transport method, remains zero during the entire simulation.

In the present chapter, we would like to explore the purely kinematic regime of the magnetic field evolution. This corresponds to very small values of the magnetic field, for which there is no back reaction on the flow (the Lorentz force can be ignored). We therefore only solve the induction equation, which is linear with respect to the magnetic field. The exact value of the parameter B_0 is therefore irrelevant, and we will always quote magnetic field intensity as a function of the initial intensity, or as a function of the average intensity. We will study the saturation regime, and how the field reaches equipartition with the thermal and kinetic energies of the gas in Chapter 3. Close to saturation and equipartition, the exact value of the field matters a lot, and in this case, the initial intensity plays a very important role. Here, however, only the initial spatial distribution and the initial topology of the field are important, but not its overall initial normalisation.

2.3.3 Summary of additional physics parameters

The feedback mechanism, whose details were explained in the previous section, can be switched on and off and in case of radiative feedback its effective strength can be controlled by changing the surrounding dust opacity parameter κ. The dwarf halo simulations were run without any radiative feedback. The only option was to have supernova feedback (simulations dubbed 'SN') or no feedback at all. In the Milky Way case, however, adding to those two options we also tested two more set-ups with radiation feedback. The values tested were one medium scale dust opacity value of $\kappa = 5\,\mathrm{cm}^2/\mathrm{g}$ ('K-5') for 70 K dust and a rather opaque gas with $\kappa = 20\,\mathrm{cm}^2/\mathrm{g}$ ('K-20') corresponding to a dust temperature of 140 K (cite Semenov et al. 2003). The feedback parameters for the dwarf as well as the Milky Way simulations are given in Table 2.1 and Table 2.2. Both configurations have the same star formation $\epsilon_* = 1\%$ and supernova feedback

Table 2.1: Halo initial conditions parameters.

parameter	Dwarf	Milky-Way	units
R_{200}	50	230	kpc
V_{200}	35	160	km/s
M_{200}	1.4×10^{10}	1.3×10^{12}	$M_\odot$
Δx	18	84	pc
$m_{\rm res}$	1.5×10^3	1.5×10^5	$M_\odot$
m_*	2.0×10^3	5.9×10^4	$M_\odot$
T_*	100	2000	K
n_*	14	4	H/cc
ϵ_*	1	1	%
$\eta_{\rm SN}$	10	10	%
$Z_{\rm ini}$	0.05	0.05	$Z_\odot$
met. yield	10	10	%

$\eta_{SN} = 10\%$ efficiencies. The temperature floor used to prevent the gas from fragmenting below our resolution limit is given by

$$T_{min} = T_* \left(\frac{n}{n_*} \right)^{2/3} \tag{2.18}$$

where the critical temperature T_* is a cool 100 K for the dwarf halo and warm 2000 K in the Milky Way case.

2.4 Field amplification by feedback processes

We will now present the results of our halo simulations, where we studied the influence of various stellar feedback parameters. This section is organised as follows: First, we present our dwarf galaxy simulations, without feedback, then using supernovae feedback. Second, we present the Milky-Way-sized galaxy simulations. For the latter case, supernovae feedback does not differ strongly from the no-feedback case, although it introduces slightly more turbulence in the gas. Radiation feedback makes however a big difference, and we explore two different dust opacities, resulting into two different scenarios for the galactic outflows.

Table 2.2: Initial magnetic field topology and feedback parameters.

Name	Topology	SN Feedback	Opacity κ [cm^2/g]
DW-D	Dipole	No	0
DW-D SN	Dipole	Yes	0
DW-Q	Quadrupole	No	0
DW-Q SN	Quadrupole	Yes	0
MW	Dipole	No	0
MW SN	Dipole	Yes	0
MW K-5	Dipole	Yes	5
MW K-20	Dipole	Yes	20

2.4.1 Dwarf galaxy

All our simulations begin in a similar way, which is the classical scenario for these cooling halo set-up. The gas, although initially in strict hydrostatic equilibrium, loses thermal energy through radiative cooling. It thus collapses and a centrifugally supported disk forms from the inside out, thanks to the initial angular momentum profile. In the dwarf galaxy case, the disc is relatively thick at first: Atomic cooling sets a natural temperature floor around 10^4 K. Low temperature radiative processes (here mostly fine-structure cooling of metals) cools the gas further, leading to the formation of a thin disc which quickly fragments into dense gas clumps. The gas density in these clumps reaches the star formation density threshold and the first stars form.

No feedback case

In absence of feedback, the disc remains very thin, and the gas clumps are long-lived. Although our star formation efficiency was set very low (one percent), most of the gas inside the dense clumps is converted into stars, after a few disc orbital time. The resulting galaxy is very efficient at transforming most of its baryons into stars, which is at odd with observed dwarf galaxies in the universe. Moreover, the resulting circular velocity profile is strongly peaked towards the centre, although dwarf galaxies circular velocity profiles are usually declining towards the centre.

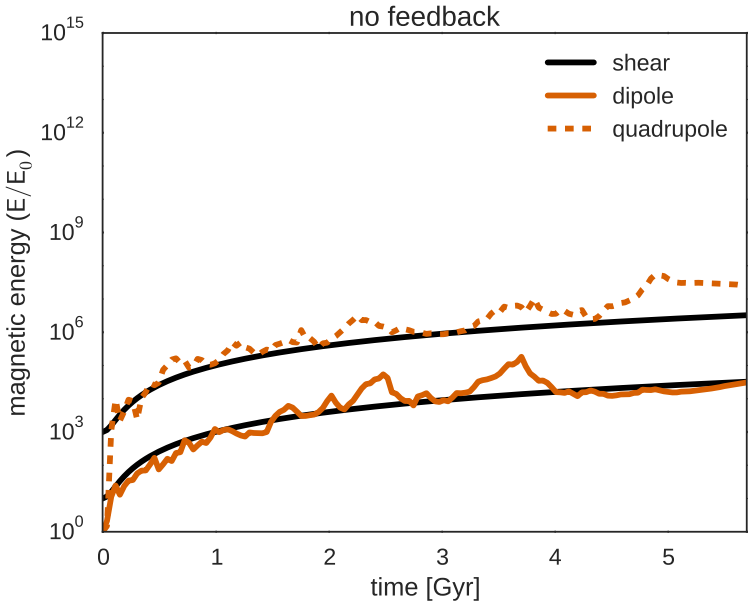

Figure 2.2: Magnetic energy evolution in the dwarf galaxy simulations without feedback, with dipole (solid lines) and quadrupole (dashed lines) initial conditions. Values are normalised to the initial total magnetic energy in the box. The black curves illustrate the shearing amplification $E_{\rm S}$ with compression values of $E_{\rm C} = 10E_0$ (dipole) and $E_{\rm C} = 10^3 E_0$ (quadrupole) and a shearing rate of $S = (100\,{\rm Myr})^{-1}$ for comparison. Without feedback, magnetic energy rises a few orders of magnitude during the initial collapse but is from then only slightly amplified by shearing over the entire simulation time.

The magnetic energy evolution can be seen in Figure 2.2. Our new simulations confirm the earlier finding of Wang and Abel (2009) and Dubois and Teyssier (2010): During the early magnetic field amplification due to the collapse of the gas in the first few Myr, the magnetic energy increases as $\Delta^{4/3}$, where Δ is the ratio of the gas density after and before the collapse. Note that the magnetic field topology matters a lot in this early evolution. Without feedback, the dipole configuration leads to magnetic reconnection in the mid plane, as expected from the antisymmetry in the poloidal field. In the quadrupole field configuration, because of the symmetry of the poloidal field, the magnetic energy is not affected by field cancellation effects.

After the collapse, one can see in Figure 2.2 that the magnetic energy still grows, but much more slowly. This can be explained from field lines being twisted by the differential rotation. In this almost perfectly axisymmetric geometry, one can indeed approximate the induction equation as (see e.g. Dubois and Teyssier, 2010)

$$\partial_t B_r \simeq 0 \quad \text{and} \quad \partial_t B_\theta \simeq r B_r \partial_r \Omega. \tag{2.19}$$

The toroidal field grows therefore only linearly with time, while the poloidal field (mostly radial) remains constant. This results in quadratic time relation of the magnetic energy

$$E_{\rm S} = E_{\rm C} \cdot \left(1 + (S \cdot t)^2\right) \tag{2.20}$$

with the magnetic energy after collapse $E_{\rm C}$, which depends on the field topology, and the shearing rate $S = r\partial_r\Omega$. We illustrate the contribution of this model for shearing amplification to $E_{\rm mag}$ for the no feedback simulations in Figure 2.2.

On the other hand, one can see directly from Equation 2.19 that a fast, exponential amplification of the field can be obtained only if the radial component grows as fast as the tangential component. For two dimensional, axisymmetric flows like our smooth rotating disk, this cannot be the case, according to the famous Zel'dovich and Cowling *anti-dynamo theorems* (Charbonneau and Steiner, 2012). A further inspection of Figure 2.2 reveals several spikes in the magnetic energy evolution. These are due to collapsing, rotating gas clumps,

which trigger short episodes of field amplification. As anticipated by Wang and Abel (2009), these vortex modes do indeed amplify the field locally, but as soon as the clumps dissolve in the large-scale rotating flow, so does their magnetic energy.

These clumps also trigger three-dimensional turbulence in the gas, thanks to clump-clump interactions (Agertz et al., 2009). This could in principle increase the magnitude of the radial component of the magnetic field, but the induced effects remain too weak to affect the large-scale dynamo. Figure 2.4 shows the velocity dispersion of the dwarf galaxy in the no-feedback case: It barely reaches 10% of the tangential velocity.

As a consequence, the corresponding magnetic field remains mostly toroidal, as shown in Figure 2.3. One can also clearly see in this Figure that the initial field parity (odd for the dipole and even for the quadrupole) has been conserved during the collapse and the subsequent shear amplification, providing a direct dependence of the final field parity on the initial halo field topology.

Supernovae feedback case

We now describe our results for the dwarf galaxy with supernovae feedback enabled. The evolution is drastically different, with violent outflows terminating quickly the life of the dense star-forming clouds. The resulting star formation rate is reduced by one order of magnitude, compared to the no-feedback case. As shown in Teyssier et al. (2013), the galactic circular velocity is now in much better agreement with observed dwarf galaxies, exhibiting a kpc-sized core in the dark matter distribution. Star formation also proceeds in successive starbursts, leading to the ejection of massive quantities of gas into a galactic fountain. The gas falls back after a dynamical time, triggering a new star formation event.

The corresponding magnetic energy evolution can be seen in in Figure 2.5. We observe, for both dipole and quadrupole initial conditions, a very fast, exponential growth with e-folding time of around 200 Myr. The measured growth rate is therefore quite fast, comparable to the rotation rate $\Gamma \simeq \Omega$. Note that the magnetic energy has been amplified by almost 18 orders of magnitude, which correspond to 9 orders of magnitude in the magnetic field itself. Figure 2.4 compares the rota-

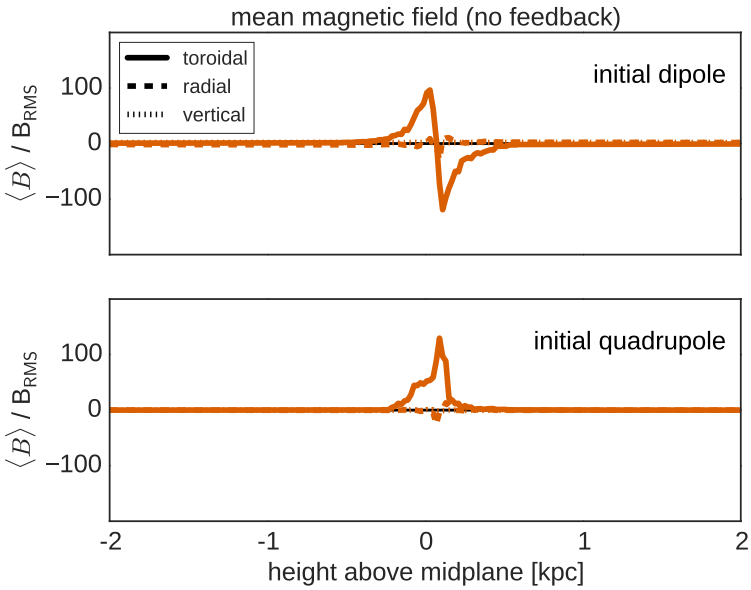

Figure 2.3: Magnetic field components after 1.9 Gyr, as a function of the vertical height relative to the galactic mid plane, normalised to B_{RMS}, the root mean square (rms) value of the field amplitude. Each component has been computed for each z bin as the volume-weighted average value inside each slice (the bin size is 10 pc). Without feedback, the initial mid plane symmetry of the radial component is imprinted on the toroidal field, whose peak value is rather high (in units of the rms field).

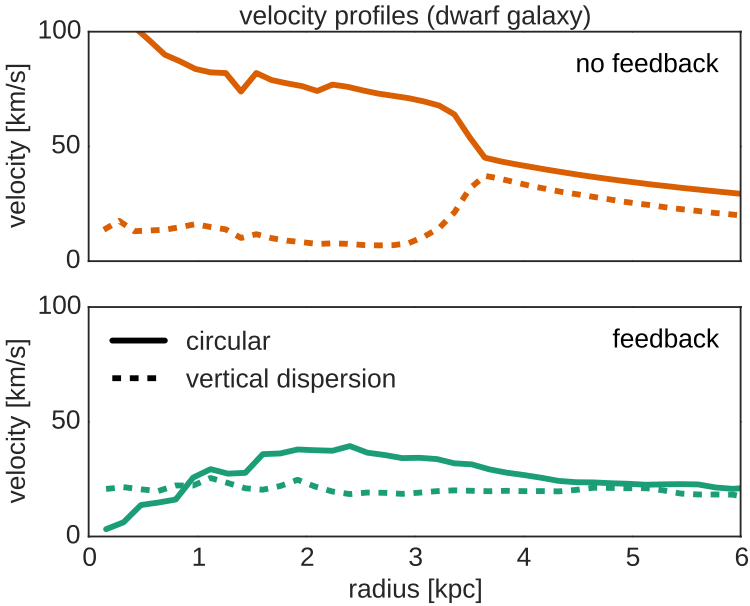

Figure 2.4: Velocity profiles of circular velocity and vertical velocity dispersion in our dwarf galaxy simulations without (top) and with feedback (bottom) at 1.9 Gyr. The solid lines show the average rotational velocity $\overline{V_\theta}$ and the dashed lines shows the vertical velocity dispersion σ_z, both as a function of the cylindrical radius.

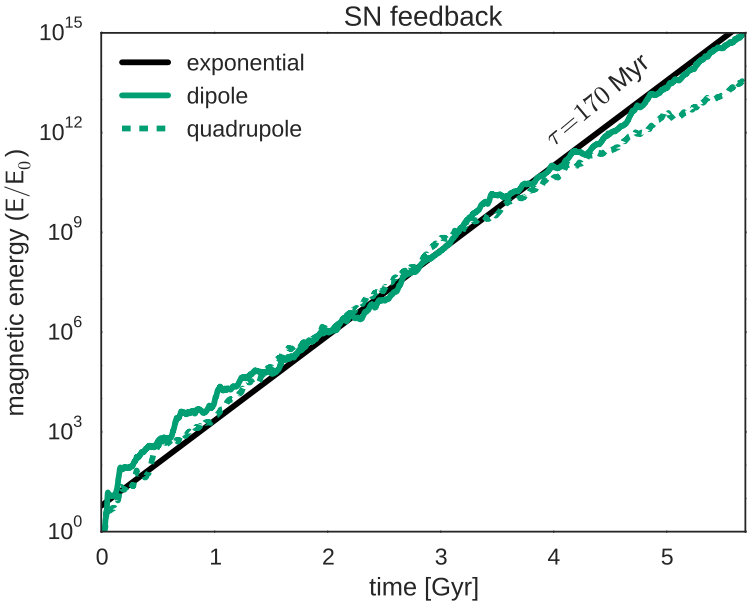

Figure 2.5: Magnetic energy evolution in the dwarf galaxy simulations with supernova feedback, with dipole (solid lines) and quadrupole (dashed lines) initial conditions. Values are normalised to the initial total magnetic energy in the box. The black straight line (right) marks an exponential growth $\exp(t/\tau)$ *at a rate of* $\tau = 170\,\mathrm{Myr}$ *for comparison. With feedback, we observe a fast exponential growth of magnetic energy over many orders of magnitude.*

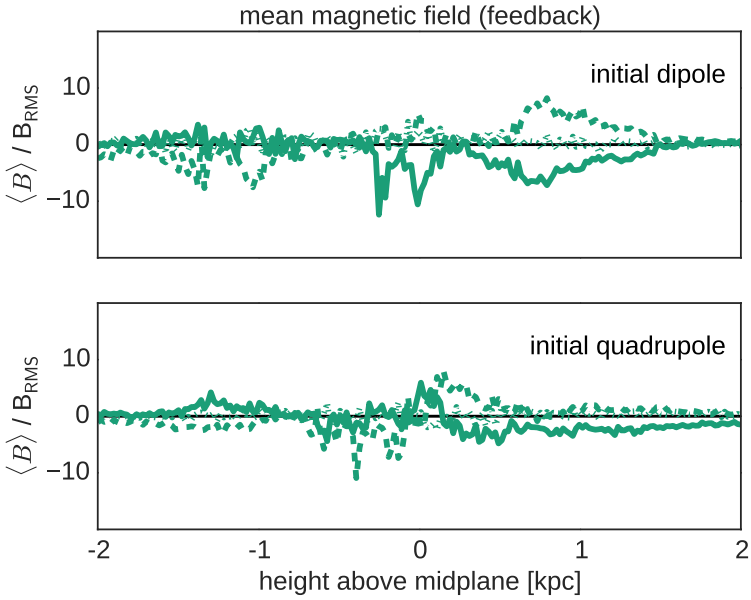

Figure 2.6: Magnetic field components after 1.9 Gyr, as a function of the vertical height relative to the galactic mid plane, normalised to B_{RMS}, the root mean square (rms) value of the field amplitude. Each component has been computed for each z bin as the volume-weighted average value inside each slice (the bin size is 10 pc). With feedback, all 3 field components are equally strong and their typical values comparable in strength to the rms.

tional velocity V to the vertical velocity dispersion σ. We have in the feedback case $V/\sigma \simeq 1$, a clear sign of strong turbulence. As a result, field lines are violently twisted in random directions, allowing the radial and vertical components of the field to reach a similar strength than the toroidal component. Figure 2.6 illustrates this isotropy in the magnetic field. The field is now highly turbulent, with the largest fluctuation seen on the smallest scales (a few cell in size).

To study further the interplay between the supernovae-driven turbulence and the growth of the field, we have computed the power spectra of both the gas kinetic energy and the gas magnetic energy in Figure 2.7. For the former, we see the almost immediate onset of a power law power spectrum like the one predicted by Kolmogorov ($P \sim k^{-5/3}$), quite typical of subsonic turbulence. The kinetic energy power spectrum appears very stable throughout the evolution, maintained at this high level by supernovae explosions and rotational energy. Note that the injection scale of the kinetic energy is very large here: it is the size of the entire galaxy. To get an idea of the nature of the forcing of the turbulence in this feedback-dominated galaxy, we have plotted in Figure 2.12 a rendering of the gas velocity field. It shows large-scale upward and downward motions, together with a clear overall rotation pattern. The largest scale at which kinetic energy is injected turns out the be roughly the halo scale radius r_s, for which marks the transition between the two power law regimes in the dark matter distribution (from r^{-1} deep inside to r^{-3} in the outskirts). In what follows, this radius will be identified to the kinetic energy injection scale, also noted L. Note that in our spectral analysis, the global rotation was not removed from the velocity field before computing its Fourier transform, because turbulence is clearly dominating. As an additional caveat, we also note that both the gas density and the magnetic field are far from being homogeneously distributed in the box where the spectrum is computed, so that the signals are only approximately isotropic and far from periodic.

The magnetic energy power spectrum, on the other hand, is plotted in Figure 2.7 (bottom). We see here again that its amplitude is exponentially growing, while its shape remains roughly the same, with $P \sim k^{3/2}$ on the large-scale end. The power spectrum reaches a maximum at a scale corresponding to 5 cells, then slowly declines as its gets to the Nyquist frequency of the grid. This is exactly what is

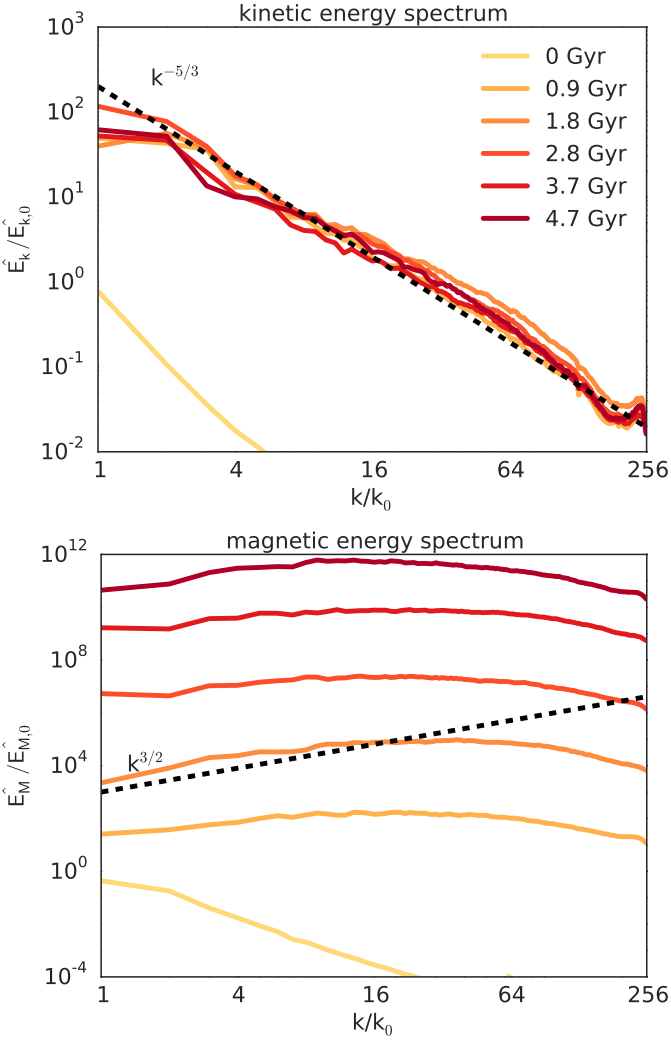

Figure 2.7: Time evolution of the kinetic and magnetic energy spectrum in a central 512^3 box and normalised to the total initial magnetic energy in the box. The simulation quickly develops a $k^{3/2}$, exponentially growing energy spectrum, typical of small-scale Kazantsev's dynamos, bottlenecked on scales of a few grid cells.

predicted from Kazantsev's theory of turbulent dynamos (Kazantsev, 1968), and confirmed in the forced-turbulence, periodic box MHD simulations of Haugen et al. (2004). In the present dwarf galaxy simulations, we also obtain a small-scale magnetic dynamo, for which the forcing scale would be the size of the entire galaxy $L \simeq 10$ kpc, and for which the magnetic dissipation scale would be set by the adopted numerical resolution.

In the small-scale dynamo theory, a critical ingredient is the magnetic Reynolds number $R_m = VL/\eta$ which encode the magnitude of the small-scale magnetic dissipation. In our notation, the velocity dispersion at the forcing scale L is V and η is the magnetic dissipation coefficient. As discussed in Brandenburg and Subramanian (2005), exponential growth of the field is obtained if $R_m > R_{\rm crit}$, where the critical magnetic Reynolds number was observed to be around 30-35. In our case, where no explicit magnetic dissipation has been included in the induction equation, this translates into a critical spatial resolution, beyond which we expect to see exponential amplification of the field.

For this reason, we repeat the dwarf simulations at different resolutions to study their effect. We show in Figure 2.8 and Figure 2.9 the time evolution of the total magnetic energy in our dwarf galaxy with 3 different maximum resolutions: Δx =36, 18 and 9 pc. We see a tendency for stronger amplification from compression with increasing resolution in all cases because the gas can build structures with higher density. Yet, without supernova feedback the subsequent shearing amplification does not show a significant impact of resolution in the resulting magnetic energy at the end. The feedback-driven dynamo, on the other hand, shows a strong growth rate dependence on the maximum resolution. In the low-resolution run, we obtain a rather slow amplification, with $\Gamma \simeq 0.4\Omega$. This means we are close to or slightly better than the critical resolution for small-scale dynamo. For our fiducial resolution, we see a fast exponential growth with $\Gamma \simeq \Omega$. In the high resolution case, we observe an even faster growth with $\Gamma \simeq 2\Omega$. In Figure 2.10, images of gas density projections are plotted to show how the gas structure is resolved at different resolutions. With increasing resolution, we see more dense substructures and importantly finer details in the flow and stronger winds.

This behaviour can be explained nicely within the framework of

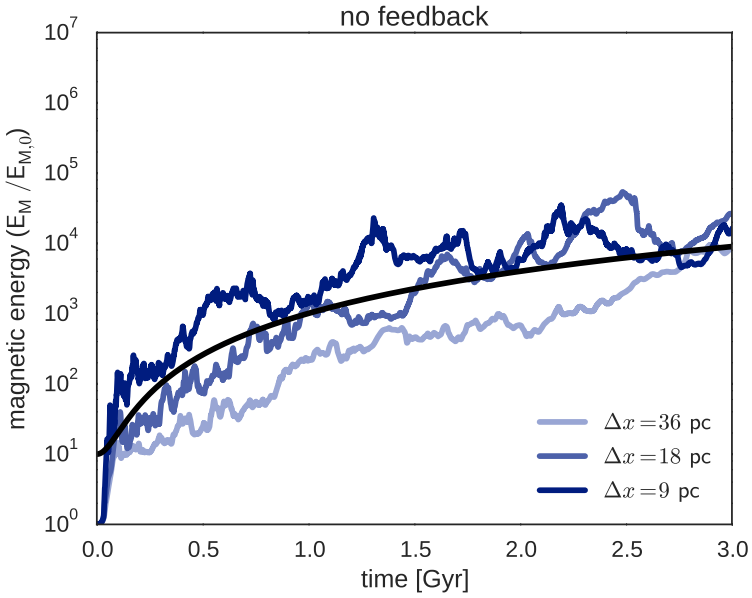

Figure 2.8: Time evolution of total magnetic energy in the simulation box for the dwarf galaxy simulation with different maximum resolutions without feedback and normalised to their initial values. The initial magnetic field topology used in all cases is the dipole type. We explore the effect of half and double resolution as compared to the original resolution of Δx = 18 pc. The black curve illustrates the same shearing amplification as in Figure 2.2.

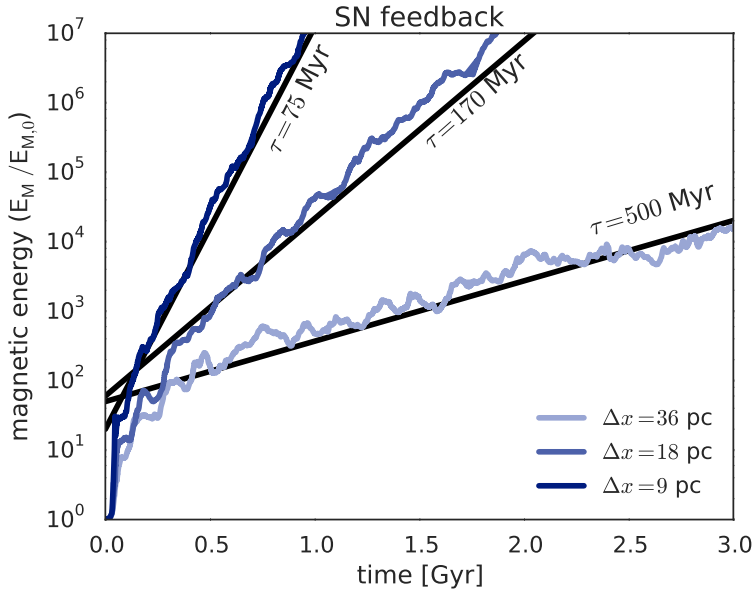

Figure 2.9: Time evolution of total magnetic energy in the simulation box for the dwarf galaxy simulation with different maximum resolutions with supernova feedback and normalised to their initial values. The initial magnetic field topology used in all cases is the dipole type. We explore the effect of half and double resolution as compared to the original resolution of Δx = 18 pc. The black straight lines show exponential growth exp(t/τ) with values of $\tau = 500, 170, 75$ Myr respectively.

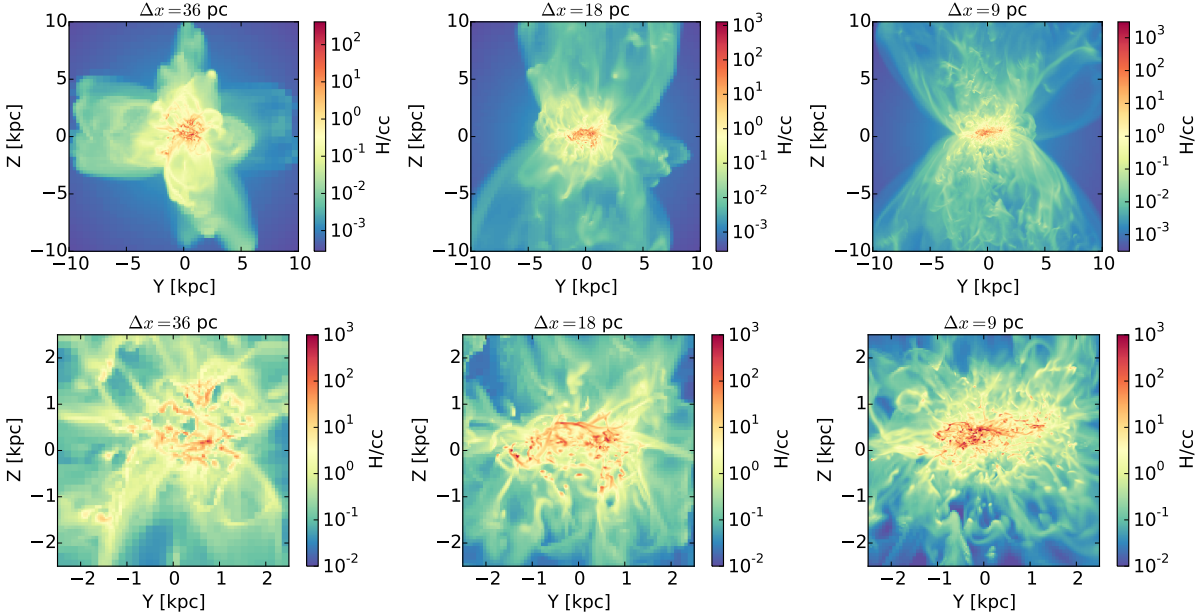

Figure 2.10: Side-on views of the mass-weighted average density in the central region of the dwarf galaxy simulation with the different spatial resolutions as in Figure 2.8, with a panel size of 20 kpc (top row) and 5 kpc (bottom row). The maximum resolution is increased from left to right, starting from $\Delta x = 36$ pc (left) to $\Delta x = 18$ pc (middle) $\Delta x = 9$ pc (right). Increasing the resolution allows one to reveal more substructures, finer details in the flow and stronger winds.

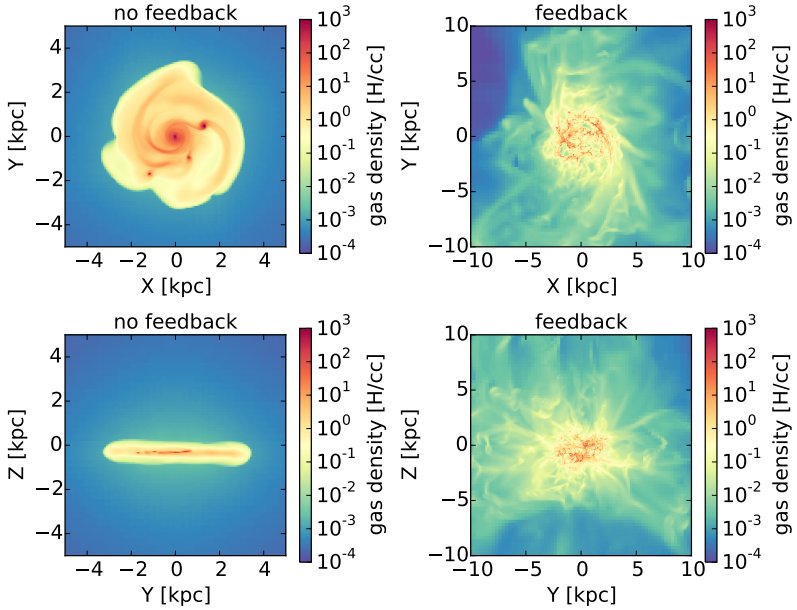

Figure 2.11: Face-on (top row) and side-on (bottom row) of mass-weighted density projections in the dwarf galaxy simulation at 1.9 Gyr. When there is no feedback (left column), the gas builds up a thin and rotationally suported disk. With feedback (right column), we form a thick, turbulence-supported disk with strong outflows.

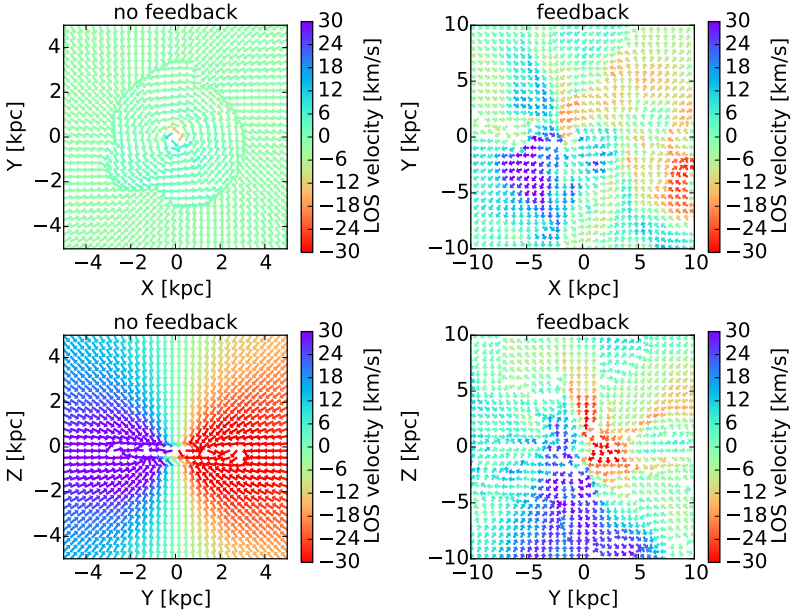

Figure 2.12: Mass-weighted average velocity field maps corresponding to the density projections of Figure 2.11. Arrows show direction (but not strength) of the mean velocity field perpendicular to the line of sight. Colours indicate the strength and direction of the line-of-sight velocity component, where blue means approaching and red means receding from the observer. Without feedback (left), gas motion is dominated by global rotation (bottom) and the vertical velocity component is weak (up). Feedback (right) drives winds which can be seen as a strong vertical component (upper panel) and significant deviations from pure rotation (lower panel).

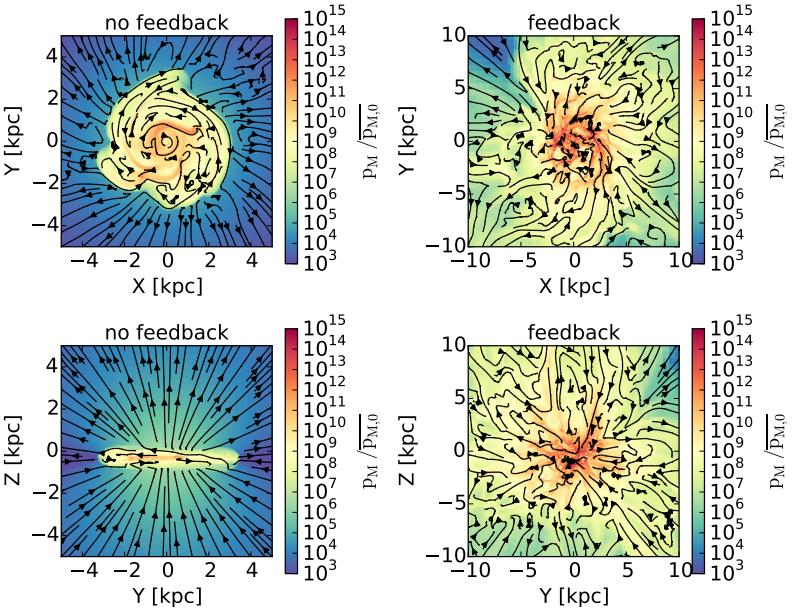

Figure 2.13: Mass-weighted magnetic pressure maps of the dipole simulation at 1.9 Gyr, normalized to the initial average magnetic pressure. Overlaid in black are streamlines of the mean field perpendicular to the line of sight. Without feedback (left), the field is ordered and dominated by a large-scale dipole structure (bottom) and a dominant toroidal field in the disk (top). With feedback (right), the magnetic field is characterised by random turbulent motions, without preferred direction or large-scale pattern (both right panels).

small-scale dynamos, for which the growth rate is determine by the inverse of the eddy turn-over time at the dissipation scale ℓ, namely $\Gamma \simeq v(\ell)/\ell \propto \ell^{-2/3}$ for Kolmogorov's turbulence. At higher resolution, the eddy turn-over time scale become shorter, so that the growth rate becomes larger. In the kinematic phase, well before the saturation phase, when the magnetic energy will reach equipartition with the kinetic energy, the growth rate of the small-scale dynamo is therefore determined by the smallest resolved scale of the turbulence, ℓ, and propagates through an inverse cascade all the way up to the forcing scale L, following the $k^{3/2}$ Kazantsev's power law.

Since actual microscopic dissipation processes are occurring on very tiny scales, completely unresolved even by our highest resolution run, one expects the actual growth rate to be even higher than the already fast rates we have measured in our numerical experiments. It is therefore reasonable to assume that field saturation will be reached very quickly. For the study of the saturation phase we refer to Chapter 3.

2.4.2 Milky-Way-like galaxy

We now describe our results for the Milky-Way-sized halo. In this case, the gas quickly cools down to 10^4 K, which leads to the immediate formation of a very thin disk. Our spatial resolution in the Milky-Way case is limited to 84 pc, so we can't allow the gas to cool much below 3000 K, as summarised in Table 2.1. Nevertheless, the disk is so massive that it also quickly fragments into massive clumps that actively form stars.

No feedback and supernovae feedback cases

In the no-feedback case, the galactic disk develops a massive central condensation of stars, which results in a central circular velocity close to 500 km/s. With supernovae feedback, however, we manage to reduce significantly the central bulge mass, with a maximum rotational velocity approaching only 250 km/s (see Figure 2.18). Note that even with supernovae feedback included, we do not reduce the overall star formation efficiency, and after several Gyr, most of the baryons have been converted into stars. This can be explained by the relatively low specific energy released by supernovae, making it very difficult for

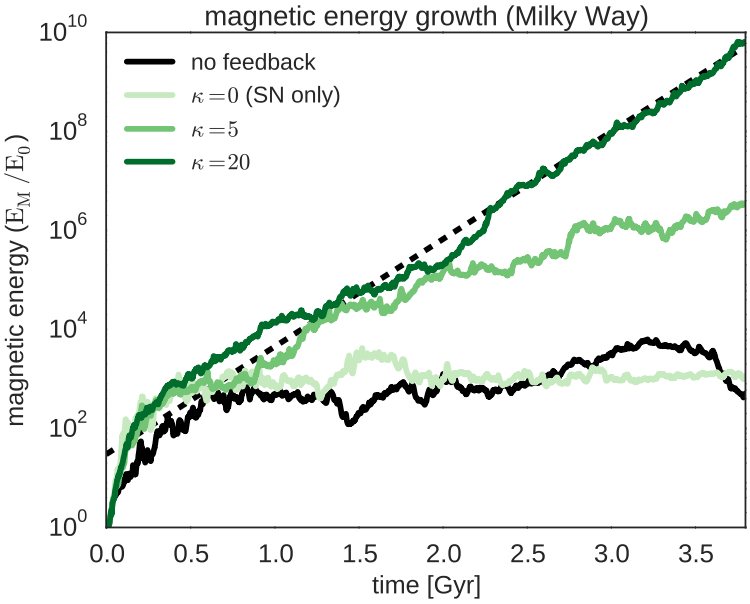

Figure 2.14: Magnetic energy time evolution in the Milky Way simulations, normalised to their initial values. The dashed line marks an exponential growth $\exp(\Gamma t)$ *at a rate of* $\Gamma = 5\ Gyr^{-1}$ *for comparison. Without feedback or only supernova feedback* ($\kappa = 0$)*, the energy does not grow after the initial collapse. Increasing the effective radiative feedback strength* κ *boosts the growth rate* Γ*.*

the gas to reach the escape velocity of the halo (see for example Roškar et al., 2014, for a complete discussion). A small galactic fountain sets in, so that the gas remains mostly bound to a weakly turbulent disc, as can be seen on Figure 2.18 in the vertical velocity dispersion profile.

Figure 2.14 shows the magnetic energy evolution for these two cases, and they exhibit the same features as the no-feedback dwarf galaxy case: early magnetic field amplification due to gravitational collapse of the cooling halo gas, followed by a weak shear amplification, with some fluctuations associated with fragmenting-clumps-induced vortex modes. The corresponding magnetic field topology appears

as very well organised on large scales, with a dominating toroidal component.

Radiative feedback case

Following the methodology explored for the first time in Roškar et al. (2014), we now consider a feedback model based on radiation from young stars efficiently absorbed by dust, and converted into kinetic energy through the infrared radiation force. Bear in mind that this model has been designed to be very optimistic, in order to maximise the effect of the radiation pressure on dust grains. Realistic modeling of the physical underlying processes is not our main objective here and we rather want to obtain an efficient feedback mechanism, launching a strong enough galactic wind, and analyse the possible effect of the resulting fountain flow on a magnetic dynamo. Images of gas density projections are shown in Figure 2.15. We have modelled our Milky-Way-like galaxy using two different values for the dust opacity: $\kappa = 5\ \mathrm{cm}^2/\mathrm{g}$ and $\kappa = 20\ \mathrm{cm}^2/\mathrm{g}$, which span a range of realistic dust temperatures. The latter model gives rise to the strongest galactic fountain, and resembles in many aspects to the dwarf galaxy case with supernovae feedback. The former, lower opacity case appears as less energetic, with a weaker wind and slightly smaller turbulence. These differences can be seen in the gas images in Figure 2.16, and are expressed quantitatively using the vertical velocity dispersion and the rotational velocity profiles (see Figure 2.18), the high opacity, more extreme case giving rise to a quasi-spheroidal galaxy, with $V/\sigma \simeq 2$.

When looking at the corresponding magnetic energy evolution on Figure 2.14, it is interesting to notice that the higher velocity dispersion corresponds to the faster growth rate. Although both galaxies show an exponential growth of the magnetic energy, only the high opacity simulation reaches a growth rate as high as $\Gamma \simeq \Omega$. The low opacity case only reaches $\Gamma \simeq \Omega/2$. This is again in line with the theory of small-scale magnetic dynamos, for which the growth rate $\Gamma \simeq v(\ell)/\ell$, is proportional to the amplitude of the velocity fluctuations. Here again, our turbulent forcing scale is the size of the entire galaxy, and the dynamo growth rate is set by the the dissipation scale, which in our case corresponds to the numerical spatial resolution.

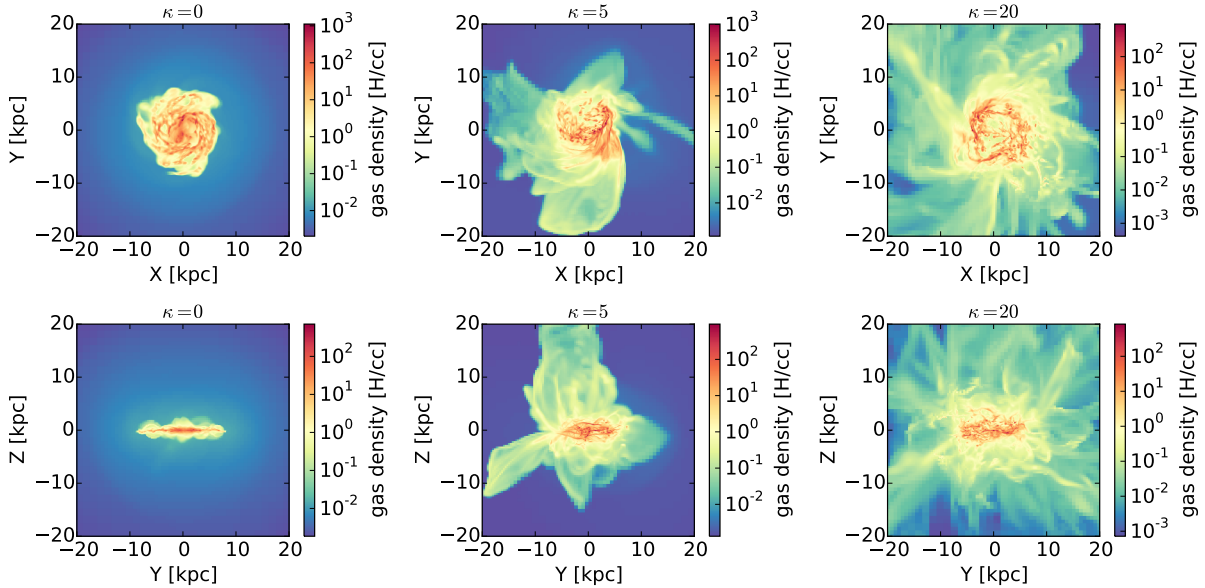

Figure 2.15: Face-on (top row) and side-on (bottom row) views of mass-weighted average density in the Milky Way simulations at 2.3 Gyr. Radiative feedback efficiencies are low (left), medium (middle) and high (right). With increased feedback strength, the disk becomes thicker and winds stronger.

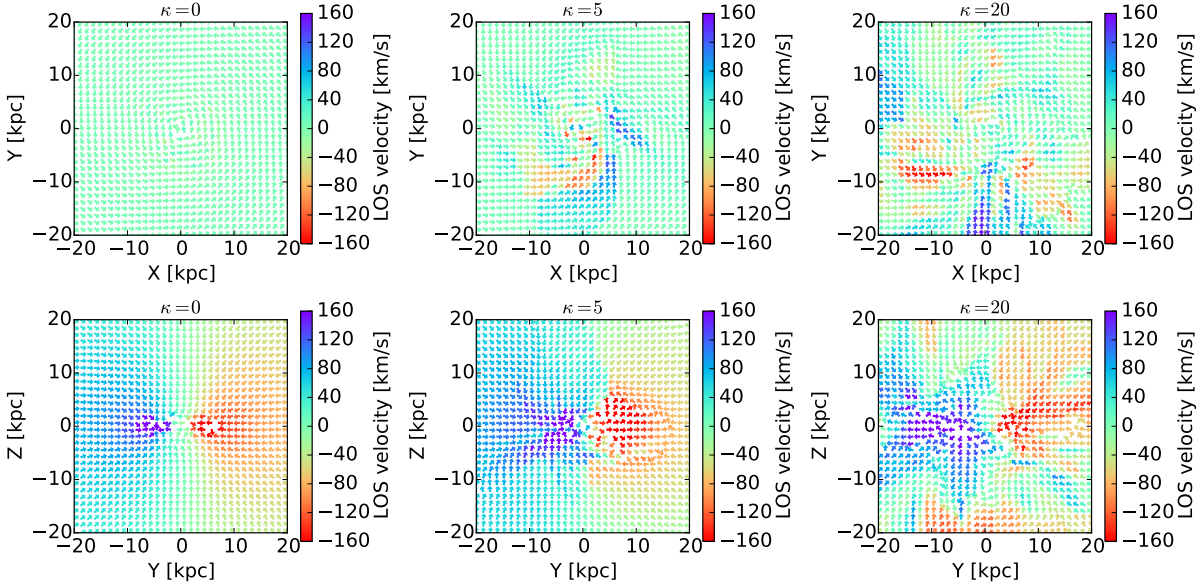

Figure 2.16: Maps of the mass-weighted average velocity field corresponding to the density projections of Figure 2.15. Arrows show direction (but not strength) of the mean velocity field perpendicular to the line of sight. Colours indicate the line-of-sight component strength and direction where blue means approaching and red means receding from the observer. While the velocity is dominated by global rotation when feedback is weak (left, SN feedback only), the gas motion develops additional small-scale motion and flows vertical to the disk (middle) until it becomes almost isotropic turbulence (right).

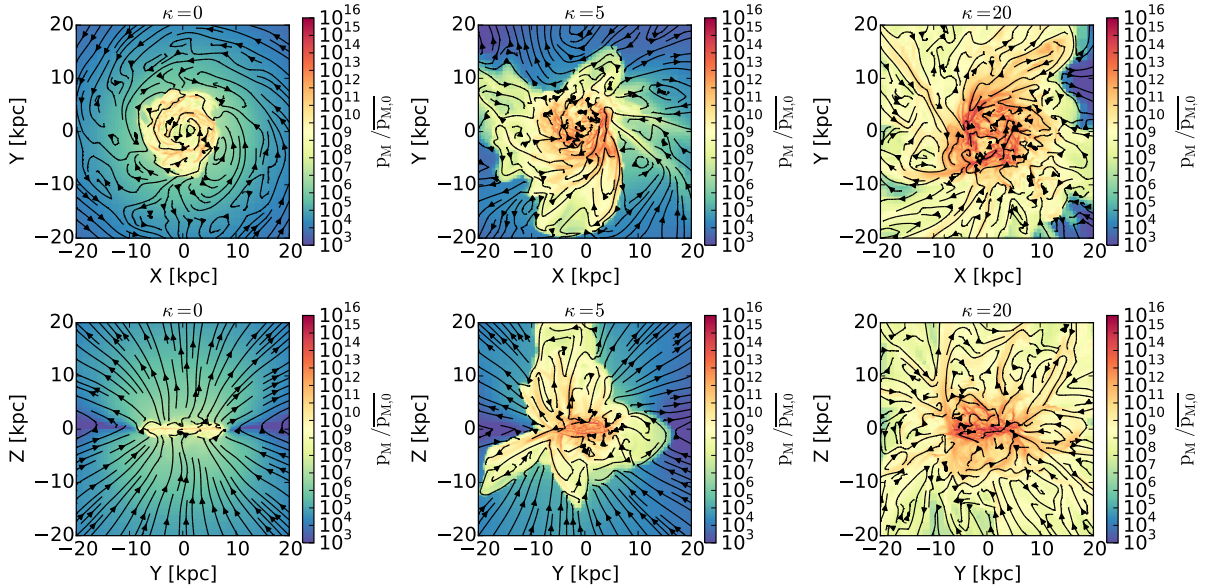

Figure 2.17: Maps of the mass-weighted magnetic pressure corresponding to the density projections of Figure 2.15 of Milky Way simulations with initial dipole field, normalised to the initial average magnetic pressure. Overlaid in black are streamlines of the mean field perpendicular to the line of sight. With weak feedback (left), the magnetic field retains the initial large-scale dipole structure outside the disk and a toroidal field inside the disk. Increasing feedback (mid and right) makes the field more small-scale.

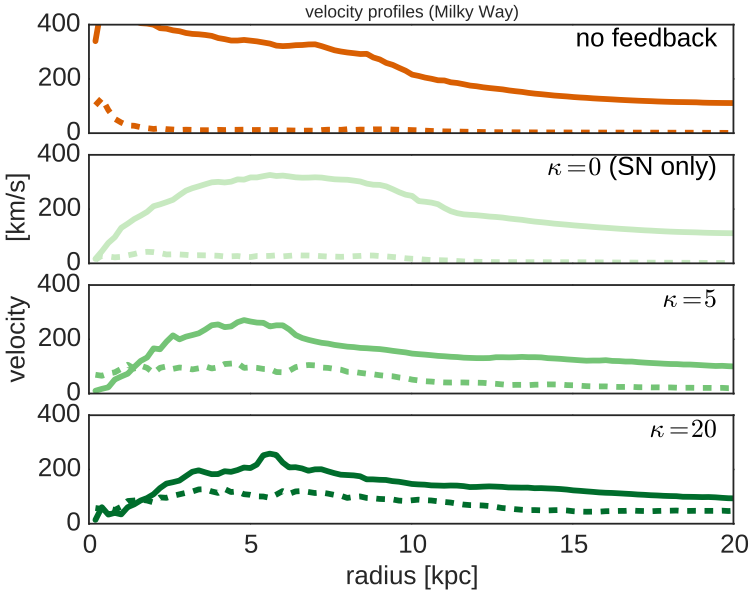

Figure 2.18: Velocity profiles of circular velocity and vertical velocity dispersion analogous to the one in Figure 2.4, but for the Milky Way simulations with increasing values of the dust opacity κ from top to bottom. While the rotational velocity $\overline{V_\theta}$ (solid lines) becomes smaller, the vertical velocity dispersion σ_z (dashed lines) increases.

2.5 Discussion

We have performed MHD simulations of feedback-dominated galaxies, both dwarf galaxies and Milky-Way-sized galaxies. We have shown that, if feedback processes are strong enough, a small-scale dynamo sets in, with a typical kinetic energy injection scale L corresponding to the size of the entire galaxy (which is in our case is close to the halo scale radius r_s), and a typical magnetic dissipation scale ℓ corresponding in our case to the adopted spatial resolution. We have observed an exponential increase of the magnetic energy, with growth rate $\Gamma \geq \Omega$, higher than the galaxy rotation rate, possibly much higher if one considers realistic microscopic diffusion processes instead of only numerical diffusion.

Three important aspects are missing in order to apply our findings to the origin of galactic magnetic fields: 1- We have considered rather idealised simulations of galaxies in isolation. 2- We have only described the kinematic phase, deferring the discussion of the saturation to Chapter 3. 3- We have considered feedback-dominated galaxies, which are relevant for the high-redshift universe. What will happen after this feedback-dominated epoch, for quiescent, razor-thin galactic discs? In this section, we speculate on possible cosmological consequences of our results on the nature of the magnetic field in high redshift galaxies, as well as the magnetic strength and topology in lower redshift galaxies.

2.5.1 Cosmological implications for high-redshift galaxies

Although our numerical simulations were not performed in a realistic cosmological context, we can still draw conclusions for the cosmic evolution of magnetic fields, assuming that the universe is made of a collection of halos of various masses, and generalised our results using simple analytical estimates. For this purpose, we will assume that high-redshift galaxies are all dominated by efficient feedback processes, so that galactic winds can drive a powerful fountain, resulting in a gas rich, turbulence-dominated corona, with a size equal to r_s, the halo scale radius, that sets the turbulence injection scale. As shown in the previous sections, a very efficient small-scale dynamo is likely to develop, with a growth rate larger (possibly much larger) than the

rotation rate of the galaxy. Although a detailed study of the saturation phase is required to study how fast the field will reach equipartition (and at what scales, see Chapter 3), we postulate here that each halo reaches equipartition between magnetic and turbulent kinetic energy almost instantaneously, within a volume set by the halo scale radius r_s. This leads to the equipartition value for the field:

$$\frac{B_{\rm eq}^2}{4\pi} = \rho_{\rm gas}\sigma_{\rm turb}^2 \tag{2.21}$$

For the gas density, we assume that its average value can be approximate by the baryon fraction $f_b = \Omega_b/\Omega_m$ of the total mass halo scale density

$$\rho_{\rm gas} \simeq f_b \rho_s \tag{2.22}$$

and for the turbulence velocity dispersion, we adopt the value inferred by our simulations, namely the halo maximum circular velocity (at r_s)

$$\sigma_{\rm turb}^2 \simeq V_{\rm max}^2 \simeq 0.193 \times 4\pi G \rho_s r_s^2 \tag{2.23}$$

Using standard redshift-dependant functions for these two halo parameters r_s and ρ_s, assuming an average halo concentration parameter $c = 8$ and a baryon fraction $f_b \simeq 0.18$, we obtain a prediction for the saturated field

$$B_{\rm eq} \simeq 3\mu G\,(1+z)^2 \left(\frac{M_{200}}{10^{10} M_\odot}\right)^{1/3} \tag{2.24}$$

The resulting magnetic pressure scales as a function of mass and redshift exactly like a "viral pressure" in the halo. Note that this equipartition field increases quite fast with increasing redshift, but quite slowly with increasing halo mass. For a feedback-dominated, Milky-Way-sized galaxy, at redshift $z = 2$, one still predicts a rather strong magnetic field, slightly above $100\mu G$. Although very interesting in setting the foundations for a theory of small-scale dynamo in the cosmological context, our present discussion remains speculative, in the sense that we do not properly model cosmological infall and the associated hierarchical merging of smaller structures. This could lead to a dilution of the dynamo-amplified field and lower the growth

rate. It is therefore of primary importance to simulate such feedback-dominated galaxy formation models with both MHD and a realistic cosmological environment.

2.5.2 Transition to quiescent, low-redshift galaxies

The cosmological applications we have derived from a simple analytical extension of our numerical results was within the context of feedback-dominated, high-redshift galaxies. Low redshift galaxies are however quite different. We see in our nearby universe many grand design, quiescent disk galaxies, with very thin, low velocity dispersion disks, and for larger halo masses, we even see red and dead elliptical galaxies. The present day universe is therefore very quiet, and strong feedback effects are absent, except may be in some very intense starbursts, usually triggered by (very rare) merger events. Our present methodology, based on isolated, gas rich, cooling halos, does not allow to explore the low redshift universe self-consistently, unless one artificially switches off feedback processes. This is the strategy we adopt in this section, in order to explore the consequence of evolving our simulated objects from a feedback-dominated state, to a more quiescent state, without strong galactic fountains, resulting in much thinner, rotationally supported disks.

It is indeed very important to estimate how the magnetic field, amplified first through a turbulent-driven small-scale dynamo, could evolve into a large-scale field, mostly driven by rotational shear. The obvious question one might ask is: Does the magnetic energy disappear, as the small-scale turbulent field reconnects on small scales? How intense will the surviving large-scale and mostly toroidal magnetic field be, after the galaxy develops into a thin, centrifugally supposed disk? For this reason, we decide to re-start our dwarf galaxy simulations after 3 Gyr of small-scale dynamo amplification, but without any stellar feedback. In the absence of galactic winds, the turbulent corona rapidly collapses back to a thin disk, and a mostly toroidal field appears after a few rotations. Images for gas density, velocity field and magnetic field of the galaxy after it has collapsed are shown in Figure 2.19.

We see in Figure 2.20 the evolution of the magnetic energy versus time for this "suppressed feedback" simulation. We see that overall,

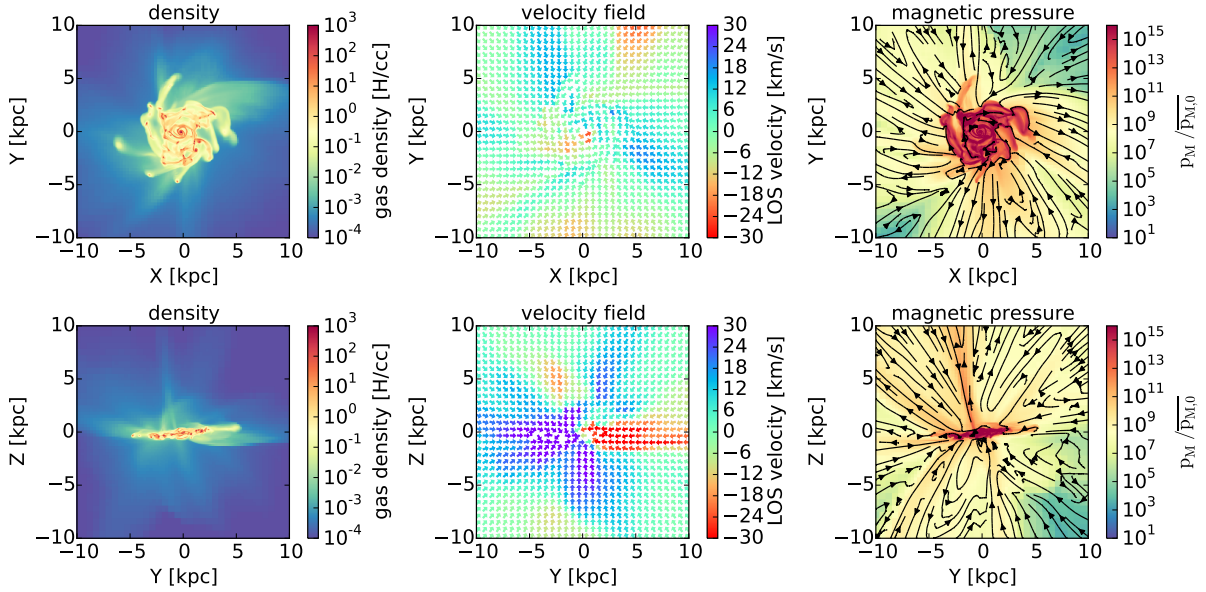

Figure 2.19: Face-on (top row) and side-on (bottom row) views of mass-weighted projections of density (left), velocity fields (middle) and magnetic field (right) of suppressed feedback simulation at 3.8 Gyr. After feedback was switched off, the gas collapses into a thin clumpy disk. Turbulence becomes weaker, and the magnetic pressure is compressed in the disk with large-scale field lines.

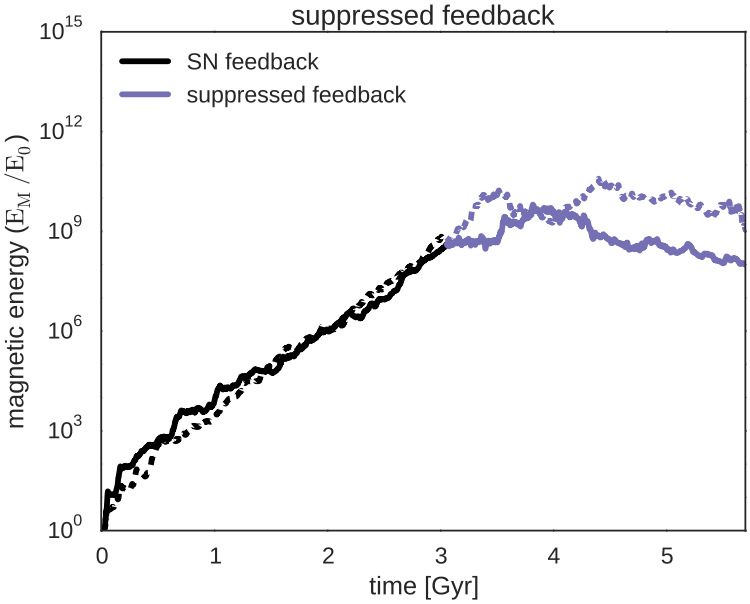

Figure 2.20: Time evolution of the magnetic energy inside the simulation box of dwarf galaxies with feedback (black) and re-runs of the same simulations from 3 Gyr, but with feedback switched off (blue), with initial dipole (solid) and quadrupole (dashed) magnetic field configuration. When feedback becomes suppressed, the exponential growth is halted and the total magnetic energy remains roughly constant.

after the thin disk appears, the magnetic energy is for the most part conserved. Two competing effects are indeed at work here: gravitational collapse that amplifies the field from a corona-diluted state to a thin disk-concentrated state, on one hand, and magnetic losses due to reconnection of mostly small-scale field lines in the mid plane of the disk. What is interesting and highly non-trivial, is that these two effects basically cancel each other, and that the final magnetic energy in the thin disk is the same than the initial magnetic energy in the large, turbulence-supported corona.

Large-scale, collapse-amplified magnetic fields have replaced small-scale, reconnection-suppressed fluctuations. Large-scale modes arise in the small-scale dynamo picture because the field is amplified on all scales at the same rate, up to the turbulence forcing scale, a well-known property of small-scale dynamos. Enough magnetic energy has been stored on large scales, so it can survive and compensate for reconnection and field cancellation effects during the collapse.

We would like to stress here again that this new type of simulations with suppressed feedback was performed in the weak field, pure kinematic regime as well. Since we believe that after the feedback-driven, small-scale dynamo phase, the field has probably quickly reached equipartition, we need to study this transition from thick-corona to thin-disk using a properly saturated field, which is the purpose of Chapter 3.

Nevertheless, we can also study the topology of the field after the disk has settled in a thin, rotation-supported state. Figure 2.22 shows the toroidal, radial and vertical field in the disk 2 Gyr after the feedback has been suppressed. The field is mostly tangential, with however stronger radial and vertical components, compared to the no-feedback case. This is in agreement with observations which show pitch angles as high as 30° (Patrikeev et al., 2006). The most interesting results is the topology of the field, which appears quadrupole-like, even if we start with only a dipole in the initial conditions. Dipole-like modes present in the large-scale magnetic field of the corona have odd parity. They will cancel in the mid plane after the gas has collapsed into a thin disk (like in the no-feedback case). Quadrupole-like modes, on the other hand, have even parity and they will be combined non-destructively in the mid plane after the collapse of the turbulent corona. One interesting prediction of the scenario which

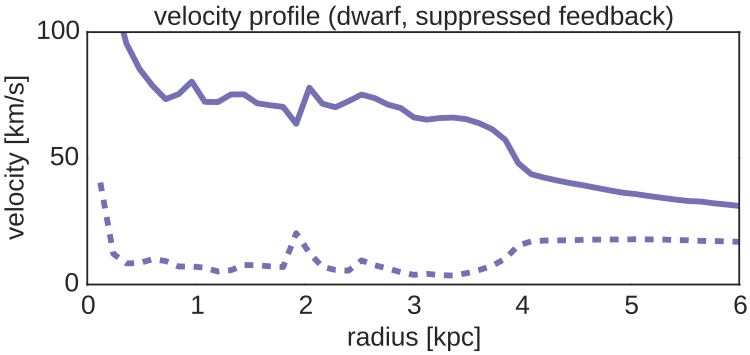

Figure 2.21: Velocity profiles of circular velocity and vertical velocity dispersion in the suppressed feedback run, as in Figure 2.4, 1 Gyr after the feedback has been switched off. Gas motions go back to being rotation-dominated, as in the no-feedback case.

we consider here is therefore a systematic quadrupole field topology, independently of the initial topology of the primordial field. This result is in very good agreement with observational data of the Milky Way (Taylor et al., 2009, Oppermann et al., 2012), as well as external galaxies (Braun et al., 2010, Mao et al., 2012).

2.6 Conclusions

We have performed MHD simulations of cooling halos, for both dwarf and Milky-Way-sized haloes, in the kinematic regime where magnetic field are weak enough so that the effect of the Lorentz force on the turbulent flow is insignificant. Using supernovae feedback for dwarf galaxies, as well as radiation feedback for large galaxies, we have shown that a small-scale dynamo quickly sets in, with the turbulent energy injection scale roughly equal to the halo scale radius r_s, and dissipation scale roughly equal to 4-5 cell sizes. In agreement with small-scale dynamo theory, we observe an exponential amplification of the magnetic energy on all scales, up to the injection scale, with a growth rate at least equal to twice the disk rotation rate. The growth

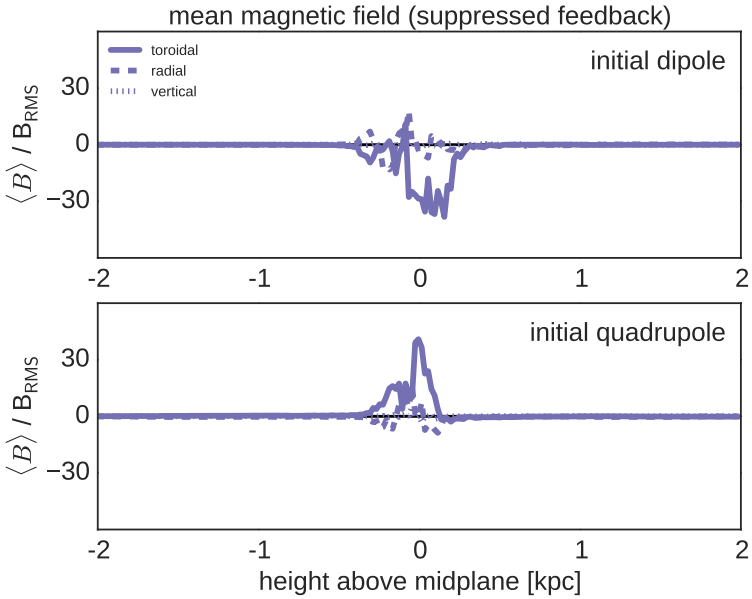

Figure 2.22: Average magnetic field components after feedback has been switched off, versus the vertical height relative to the galactic mid plane, computed as in Figure 2.3 and normalized to $B_{\rm RMS}$. After collapse, the magnetic field is dominated by its toroidal component, but we also see a non-negligible radial component. The toroidal component has also developed an even symmetry across the mid plane, as in the simulations with initial quadrupole and without feedback, even if the initial condition was a dipole (top).

rate in the kinematic phase is set by the adopted numerical resolution. In our simulated halo, we need to have a resolution of 20 pc or better (for $r_s \simeq 3.5$ kpc) to obtain a significant growth rate (as high as $\Gamma \simeq \Omega$).

This corresponds roughly to 100 resolution elements per turbulent energy injection scale. We believe this resolution corresponds to the critical magnetic Reynolds number $R_m \simeq 35$, beyond which magnetic field amplification through small-scale dynamo is possible. Note that for weaker feedback scenarios, the kinetic energy injection scale is likely to be smaller, which translates into more stringent resolution requirements. This analysis should be kept in mind, when one wants to extend this to the cosmological context. One difficulty might arise when one considers infall of pristine, low magnetic field gas as a source of field dilution. This could require a larger small-scale dynamo growth rate for the field to be able to increase, and therefore results in even more demanding resolution requirements.

We have shown that a small-scale dynamo, driven by strong feedback processes in high-redshift galaxies, could be the origin of galactic magnetic fields. This scenario is completely different than the more traditional large-scale dynamo approach, in the sense that the small-scale dynamo acts very quickly at amplifying the field up to the turbulent injection scale. The new ingredient is here the fact that feedback processes at high redshift are probably energetic enough, so that this injection scale is the size of the entire galaxy (more precisely the halo scale radius r_s). We therefore have a small-scale dynamo, together with a large-scale forcing, hence enabling the fast amplification of the field all the way up to the scale of the entire galaxy.

We have also shown, using simple numerical experiments with suppressed feedback, that the field can evolve into a large-scale toroidal, quadrupole field in a low-redshift quiescent state, although it has been amplified by a small-scale dynamo. Compared to the large-scale dynamo picture, for which the field is amplified in a thin disk over several Gyr, the small-scale dynamo picture completely reverses the point of view, with a very strong field already in place at high redshift (after a feedback-dominated epoch) that slowly evolves until the present epoch. This large-scale field could even slowly decay, on resistive time scales, and still be large enough to account for the observed field strength in nearby galaxies. In this new picture, large-scale dynamos are not required anymore to amplify the field from its primordial

value around $10^{-20}G$ to μG levels. Instead, they are needed to maintain the field at a roughly constant level by compensating dissipative losses.

3 Small-scale dynamo saturation

We have seen in Chapter 2 how the small-scale dynamo can efficiently amplify even weak magnetic seed fields on very fast timescales. In this chapter[1], we will investigate what happens as the magnetic field strength approaches equipartition and the dynamo saturates.

Performing high-resolution adaptive mesh magnetohydrodynamic simulations of a small mass, isolated cooling halo with an initial magnetic seed field strength well below equipartition, we follow the small-scale dynamo amplification from supernova-induced turbulence up to saturation of the field. We find that saturation occurs when the average magnetic pressure reaches only 3% of the turbulent pressure. The magnetic energy growth transitions from exponential to linear, and finally comes to halt. The saturation level increases slightly with grid resolution. These results are in good agreement with theoretical predictions for magnetic Prandtl numbers of order $\mathrm{Pr_m} \sim 1$ and turbulent Mach numbers of order $\mathrm{M} \sim 10$. When we suppress supernova feedback after our simulation has reached saturation, we find that turbulence decays and that the gas falls back onto a thin disk with the magnetic field in local equipartition in most of the dense gas arms.

We propose a scenario in which galactic magnetic fields are amplified from weak seed fields in the early stages of the Universe to sub-equipartition fields, owing to the turbulent environment of feedback-dominated galaxies at high redshift, and are evolved further in a later stage up to equipartition, as galaxies transformed into more quiescent, large spiral disks.

[1]The work presented in this chapter has been published in the *Monthly Notices of the Royal Astronomical Society*, Volume 471, Issue 3 under the title 'A small-scale dynamo in feedback-dominated galaxies - II. The saturation phase and the final magnetic configuration' following peer-review (Rieder and Teyssier, 2017a). It was also presented at the European Week of Astronomy and Space Science organised by the European Astronomical Society in Athens, Greece, on 4th July 2016.

3.1 Introduction

Measurements of Faraday rotation in the Milky Way (Taylor et al., 2009), in nearby galaxies (Beck, 2016) as well as in high-redshift galaxies (Bernet et al., 2008) reveal strong magnetic fields, usually close to equipartition with the turbulent energy density. Robishaw et al. (2008) have detected field strengths up to $18\,\mathrm{mG}$ in starburst galaxies but ordered galactic magnetic fields in the ISM of normal spiral galaxies are typically of the order of several $\mu\mathrm{G}$. Their field lines mostly exhibit a spiral structure if the galaxy is itself a grand design spiral galaxy (Beck and Wielebinski, 2013) but, interestingly, this can also be the case for ring galaxies like NGC 4736 (Chyży and Buta, 2008), flocculent galaxies like NGC 4414 without clear spiral arms (Soida et al., 2002) or in the central regions of galaxies. Strong ordered fields are found at the edges of optical arms with dense cold molecular gas in M 51 (Patrikeev et al., 2006) but can also form their own magnetic arms not coinciding with the gaseous or the optical spiral arms like in NGC 6946 (Beck, 2007). In a set of aggregated data on 20 spiral galaxies from the literature, Van Eck et al. (2015) report pitch angles ranging between $-8\,^\circ$ and $-48\,^\circ$ with a mean value of $-25\,^\circ$ and find a correlation between the spiral arm pitch angles and the magnetic pitch angles.

The origin of magnetic fields in the Universe might be primordial (Durrer and Neronov, 2013) or due to microphysical processes at later epochs, such as the Biermann battery (Biermann, 1950) in shock fronts (Kulsrud et al., 1997) or ionization fronts (Gnedin et al., 2000), spontaneous fluctuations (Schlickeiser, 2012) or fluctuations due to the Weibel instability (Lazar et al., 2009) in the plasma of protogalaxies, or even magnetic fields released into the ISM by stars through stellar winds or supernova outbursts (Bisnovatyi-Kogan et al., 1973) or even by AGN jets (Rees, 2005) and subsequently diluted.

Microphysical mechanisms (such as the Biermann battery) are capable of creating magnetic fields of the order of $10^{-20}\,\mathrm{G}$, while the constraints on the primordial field are less definite because the difference between lower and upper limits remains vast. Upper limits can be derived from Big Bang Nucleosynthesis (BBN) abundances and from the large-scale density structure or the Cosmic Microwave Background (CMB). Planck Collaboration et al. (2016a) currently set

the upper limit of the primordial magnetic field (PMF) field strength to 10^{-9} G in the comoving frame based on their CMB anisotropy measurements. γ-ray observations of blazar spectra give lower limits for the field strength ranging from 10^{-18} G up to 10^{-15} G (Neronov and Vovk, 2010, Dermer et al., 2011, Vovk et al., 2012), based on the remnants of the PMF that are believed to thread the intergalactic medium. This leaves us to explain many orders of magnitude magnetic field amplification in a timeframe of just a few Gyr.

Large-scale dynamos (LSD) are a viable mechanism to amplify magnetic fields coherently on (as the name suggests) large spatial scales. Theoretical models for galactic LSD exhibit exponential growth rates of the order of $\Gamma \simeq 0.01 - 0.1\Omega$ (Pariev et al., 2007), where Ω is the galactic angular rotation rate. This translates into an e-folding time scale of roughly 1 Gyr in a typical present-day spiral, making it virtually impossible to amplify the field as fast as required by the observations. Parker (1992) proposed also a cosmic-ray-driven LSD, that was simulated for the first time by Hanasz et al. (2004), who found a larger growth rate of $\Gamma \simeq \Omega$.

Small-scale dynamos (SSD) on the other hand, can have very fast magnetic field amplification, with timescales of the order of the eddy turnover times of the smallest turbulent eddies (Brandenburg et al., 2012). The theoretical foundation of this dynamo theory is commonly attributed to Kazantsev (1968). Kulsrud and Anderson (1992) considered the Kolmogorov power spectrum of small-scale velocity fluctuations for the galactic dynamo and found that the magnetic energy spectrum scales with the wavenumber as $k^{3/2}$ on scales larger than the resistive scale. Schober et al. (2015) presented a theoretical analysis of the SSD, in the limits of both small and large magnetic Prandtl numbers, finding that its growth rate scales with respectively the magnetic or kinetic Reynolds number. They also evaluated the ratio of magnetic to turbulent energy after saturation, finding values between 0.1% and 50%, depending on the model of turbulence, on the value of Pr_M and on the value of the Mach number. Their results are confirmed by previous numerical investigations on the turbulence-driven dynamo such as Federrath et al. (2011, 2014) or Tricco et al. (2016), who also reported that the saturation level is slightly increasing with resolution. The main issue with the SSD mechanism is, however, that it creates strong fluctuating fields, for which the large scale component

is subdominant, and generally does not reach equipartition. These two properties are in contradiction with observational data of nearby galaxies (Beck, 2015). On the other hand, it is plausible that the magnetic fields we observe in galaxies are not the result of just one single process, but probably a combination of various mechanisms, such as the two dynamos theory (Squire and Bhattacharjee, 2015) or various reconnection processes during the hierarchical assembly of galaxies.

The importance of feedback processes has been recognised increasingly over the past decade in galaxy formation theory (Scannapieco et al., 2012), along with the influence of associated galactic winds (Oppenheimer and Davé, 2006) and the dominant cold stream accretion mechanism (Kereš et al., 2005, Ocvirk et al., 2008, Dekel et al., 2009). Observations suggest that galactic winds are ubiquitous in star bursting local galaxies (Martin, 1999), as well as many "normal" high redshift galaxies (Steidel et al., 2010). Abundance matching between dark matter haloes and observed central galaxies (Behroozi et al., 2013, Moster et al., 2013) suggests considerably stronger feedback processes than previously considered for early galaxies to regulate star formation through cosmic evolution, especially at high redshift, to maintain such a low star formation efficiency (Agertz et al., 2013, Hopkins et al., 2014, Roškar et al., 2014, Wang et al., 2015). Interestingly, Kim et al. (2016) found a correlation between strong magnetic field signatures in the Faraday Depth spectrum and strong Mg II absorption, which is associated with superwinds from starbursting galaxies (Bond et al., 2001), suggesting a link between strong outflows and a high magnetisation of the intergalactic medium.

In this rather violent, feedback-dominated scenario, dwarf galaxies play a very important role. They are the dominant galaxy population at high redshift, probably responsible for the cosmic re-ionisation (Kimm and Cen, 2014). They are also the progenitors of the Milky Way satellites, which are useful laboratories to test our current galaxy formation paradigm. For the latter, violent feedback mechanisms have also been invoked to explain the absence of cusp in the dark matter density profile, and the presence of a dark matter core in low surface brightness galaxies (de Blok et al., 2001). Cosmological simulations of dwarf galaxies have been performed with strong feedback recipes, confirming in this case the formation of a dark matter core (Governato et al., 2010, 2012, Teyssier et al., 2013).

In galaxies, the velocity field on both small and large scales resulting from repeated giant feedback events can have a direct influence on the growth of the magnetic energy. Indeed, supernovae explosions in the Milky Way have been considered for quite a long time as a source of helical gas motions, promoting a large-scale α-dynamo in the Galaxy (Ferriere, 1992). The Milky Way is a rather quiescent galaxy with moderate supernova activity but might have undergone different phases in its lifetime. We therefore want to study in this work the small-scale dynamo-induced growth of magnetic fields in dwarf galaxies under the influence of strong feedback, how it reaches saturation and how the magnetic field could evolve when feedback becomes weaker. In the first step, we are considering a feedback-dominated galaxy, with a high star formation rate and violent turbulent motions, together with large-scale galactic fountains or winds. As the magnetic field grows until the small-scale dynamo is saturated, this feedback is turned off in the second step to see how it evolves in a less turbulent, quiescent phase.

In recent years, several simulations of the magnetic fields evolution have been performed in the context of galaxy formation (Wang and Abel, 2009, Dubois and Teyssier, 2010), These early studies were based on the "cooling halo" numerical set-up, and have achieved only moderate magnetic field amplification. An important shortcoming in these simulations was the absence of feedback (Wang and Abel, 2009), or the relative weakness of the feedback recipe used at that time (Dubois and Teyssier, 2010). Beck et al. (2012) performed a simulation using a new developed MHD version of the GADGET code GADGET, using a divergence cleaning technique, and they observed a fast exponential growth of the magnetic field, which they attributed to a small-scale dynamo. Surprisingly, they did not include any explicit source of turbulence resulting in a relatively smooth flow, but reported nevertheless a very large growth rate.

More recently, Pakmor and Springel (2013) also observed strong magnetic field amplification using the MHD version of the AREPO code (Pakmor et al., 2011), although also in this case, stellar feedback effects were not introduced explicitly, and the smoothness of their effectively 2D rotating flow would make dynamo amplification notoriously difficult to obtain. The same code was used very recently for cosmological zoom-in simulations of Milky Way-like disk galaxies

in Pakmor et al. (2017), this time including a more realistic treatment of stellar feedback, resulting in strong turbulence driving. As a consequence, a fast magnetic energy amplification was observed at high redshift, attributed to the SSD, followed by a slower amplification at lower redshift, attributed to the LSD.

In Chapter 2, simulating a dwarf galaxy at high resolution, we found strong evidence for a small-scale dynamo operating in galaxies with feedback-driven turbulence, with e-folding timescales of up to 100 Myr. A similar approach was used in Butsky et al. (2017) for a Milky Way galaxy where the magnetic field was seeded by supernova ejections. Another interesting study was conducted recently by Dobbs et al. (2016) who impose a spiral potential in their simulations of an isolated disk and found magnetic field reversals.

In this chapter, we follow up on Chapter 2, using again the isolated cooling halo setup, with strong stellar feedback to investigate the mechanism of magnetic field amplification through the SSD. We use the Adaptive Mesh Refinement code RAMSES (Teyssier, 2002), adopting the "Constrained Transport", strictly divergence-free-preserving, MHD solver presented in Teyssier et al. (2006) and in Fromang et al. (2006). We focus here our analysis of the saturation properties of the SSD in the galaxy formation context. This chapter is organised as follows: In Section 3.2, we present our numerical methods in terms of galaxy formation physics and magnetic fields evolution, as well as the intricacies of modelling realistic turbulent flows in numerical simulations. In Section 3.3, we describe our initial conditions for the isolated, magnetised cooling dwarf halo. In Section 3.4, we present our main results on dynamo saturation and study the impact of resolution and stellar feedback. In Section 3.5, we discuss our results in the context of current galactic dynamo theories. Finally, in Section 3.6, we discuss the implications of our work for our understanding of cosmic magnetism.

3.2 Numerical methods

We use the Adaptive Mesh Refinement (AMR) code RAMSES (Teyssier, 2002) to simulate the formation and evolution of an isolated dwarf galaxy. It is modelled as a magnetised ideal plasma,

coupled through gravity to a collisionless fluid made of dark matter and stars, with additional numerical schemes to account for physical sub-resolution processes such as gas cooling, star formation and supernova feedback. In this section, we outline the numerical methods used in this work to model self-gravitating supersonic turbulence driven by stellar feedback.

3.2.1 Ideal MHD with Gravity

We solve the ideal MHD equations which are written here without gravity and cooling source terms for the sake of simplicity:

$$\partial_t \rho + \nabla \cdot (\rho \mathbf{u}) = 0 \tag{3.1}$$

$$\partial_t (\rho \mathbf{u}) + \nabla \cdot (\rho \mathbf{u}\mathbf{u}^T - \mathbf{B}\mathbf{B}^T + P_{\rm tot}) = 0 \tag{3.2}$$

$$\partial_t E + \nabla \cdot [(E + P_{\rm tot})\mathbf{u} - (\mathbf{u} \cdot \mathbf{B})\mathbf{B}] = 0 \tag{3.3}$$

$$\partial_t \mathbf{B} - \nabla \times (\mathbf{u} \times \mathbf{B}) = 0 \tag{3.4}$$

where ρ is the gas density, $\rho\mathbf{u}$ is the momentum, $\mathbf{B}$ is the magnetic field, $E = \frac{1}{2}\rho\mathbf{u}^2 + \rho\varepsilon + \frac{1}{2}\mathbf{B}^2$ is the total energy, and ε is the specific internal energy. The total pressure is given by $P_{tot} = P + \frac{1}{2}\mathbf{B}^2$ where we assume a perfect gas equation of state $P = (\gamma - 1)\rho\varepsilon$. This system of conservation laws is furthermore completed by the solenoidal constraint

$$\nabla \cdot \mathbf{B} = 0. \tag{3.5}$$

RAMSES uses a hybrid approach with gas variables stored on a tree-based adaptively refined mesh, while dark matter and stars are tracked by collisionless particles. The equations above are solved using the second-order unsplit Godunov scheme based on the MUSCL-Hancock method with the HLLD Riemann solver and MinMod slope limiter. The induction equation (Equation 3.4) is solved with the Constrained Transport (CT) method (Teyssier et al., 2006), which preserves the divergence of the magnetic field $\nabla \cdot \mathbf{B} = 0$ from the initial conditions, and MonCen sloper limiter. We use free-outflow boundary conditions with imposed zero-gradient at the simulation box boundaries for the gas variables and the perpendicular magnetic field.

To treat physical processes that are well below the resolution limit but nevertheless important in the theory of galaxy formation, we

include several effects such as gas cooling, star formation and supernova feedback. Gas cooling is implemented using a standard H and He cooling function, with an additional metal cooling component, as in Sutherland and Dopita (1993) for temperatures above 10^4 K, and fine-structure cooling of [CI] and [OII] below 10^4 K, based on Rosen et al. (1995). Cooling stops at a minimum pressure floor in order to ensure the Truelove criterion (Truelove et al., 1997) and always resolve the Jeans length by at least 4 grid cells. We create star particles as a random Poisson process compliant with a Schmidt law as in Rasera and Teyssier (2006). The effect of supernovae is modelled by releasing non-thermal energy into the ISM over a dissipation time scale of 20 Myr (Teyssier et al., 2013). We refer to Chapter 2 for a more detailed account.

3.2.2 Turbulence

Modelling turbulence properly is central to our goal of simulating the small-scale dynamo. Two key quantities in this context are the Reynolds number, which is the ratio of inertial vs. viscous forces

$$\mathrm{Re} = \frac{uL}{\nu} \tag{3.6}$$

where ν is the kinematic viscosity and u and L are the typical velocity and length scale of the problem, and its counterpart for the magnetic field, the magnetic Reynolds number as the ratio of induction vs. diffusion

$$\mathrm{Re_M} = \frac{uL}{\eta} \tag{3.7}$$

where η is the magnetic diffusitivity. Additionally, it is useful to define the magnetic Prandtl number

$$\mathrm{Pr_M} = \frac{\mathrm{Re_M}}{\mathrm{Re}} = \frac{\nu}{\eta} \tag{3.8}$$

as the ratio of those two quantities and thus as the ratio of kinematic viscous and magnetic diffusivity. Our simulations do not account for microscopic diffusion processes, as we aim at solving the ideal MHD equations, but the stability of the numerical solution and its

convergence towards the weak solution of the underlying model equations are both enforced by the numerical diffusion inherent to the Godunov scheme. Due to our limited spatial resolution of $\Delta x \simeq 10\,\mathrm{pc}$, the numerical effective viscosity and magnetic diffusivity coefficients are both much greater than the typical physical values for the typical ISM.

RAMSES has been tested to successfully reproduce idealised fast dynamo flows (Teyssier et al., 2006) such as the ABC flow (Galloway and Frisch, 1986, Childress and Gilbert, 2008) or the Ponomarenko dynamo (Ponomarenko, 1973). The numerical magnetic Reynolds number was shown to be proportional to the inverse square of the number of grid points, which is to be expected with second-order schemes and rather smooth solutions. However, in the context of a highly complex flow such our turbulent galaxy, where kinematics is dominated by rotation and supernova explosions inside a deep gravitational potential, it becomes virtually impossible to exactly determine neither viscosity nor diffusion due to the numerical scheme. This is even further complicated by the adaptively refined mesh. Qualitatively, it is sufficient to know that viscous effects as well as magnetic reconnection and diffusion caused by the numerical scheme happen at a length scale which is close to the mesh size, which is mainly the cell size at the maximal refinement level. We also point out that numerical viscosity and numerical diffusion are approximately equal due to their identical numerical origin, so that the effective magnetic Prandtl number $\mathrm{Pr_M} \simeq 1$ (cf. Teyssier, 2015, for more discussion).

3.3 Initial conditions

As in Chapter 2, we simulate an isolated dark matter halo with gas cooling and a small initial rotation. In our previous work, we have conducted a study on varying initial conditions with different halo sizes and initial magnetic field topologies and we found no significant impact on the nature of the dynamo itself. If the feedback mechanism is strong enough to stir strong turbulence in the disk and launch a large scale galactic wind, the magnetic field lines quickly become mangled, so that their initial topology and symmetry are lost and the flow develop a strong characteristic random, quasi isotropic and

Table 3.1: Parameters of initial halo set-up and additional physics mechanisms

parameter	value	unit
R_{200}	50	kpc
V_{200}	35	km/s
M_{200}	14	$10^9 \mathrm{M}_\odot$
c	10	
λ	0.04	
f_{gas}	15	%
T_*	100	K
ϵ_*	1	%
η_{SN}	10	%
Z_{ini}	0.05	$\mathrm{Z}_\odot$
metal yield	10	%
B_{max}	0.35	nG
sim. box length	300	kpc

mostly small-scale component. We are now especially interested in the final phase of the dynamo mechanism, when the magnetic energy growth reaches saturation.

The initial dark matter and baryonic matter densities follow the NFW profile (Navarro et al., 1997) with concentration parameter $c = 10$ and spin parameter $\lambda = 0.04$ as in Teyssier et al. (2013). Dark matter is sampled by 10^6 particles and set to be in equilibrium with the gas by the density-potential pair approach of Kazantzidis et al. (2004) and Read et al. (2006). The temperature profile is also initialised to be in hydrostatic equilibrium. The numerical values of the parameters specific to this set-up are given in Table 3.1. In order to study the effect of numerical resolution on the dynamo saturation properties, we increase the resolution in a second simulation run. The resolution parameters for the two runs are given in Table 3.2.

In Chapter 2, we have studied the dynamo only in the kinematic phase, choosing an arbitrarily small value for the initial magnetic energy. Now we want to see what happens when the magnetic field becomes strong enough to become dynamically important. We have therefore to increase the initial magnetic field strength, but keeping

Table 3.2: Size of smallest grid cells and mass resolutions

resolution	$l_{\max}$	Δx [pc]	$m_{\rm res}$ [$M_\odot$]	m_* [$M_\odot$]	n_* [H/cc]
low	14	18	1523	2108	14
high	15	9	190	264	112

it small enough for the dynamo to operate in the kinematic phase for some time (so that the initial magnetic energy is several orders of magnitude smaller than equipartition), but not too small for the dynamo to saturate in a reasonable amount of time.

Initialising the magnetic field on an adaptively refined grid is a non-trivial task. In order to satisfy the zero-divergence constraint (Equation 3.5), it would be tempting to simply set the initial field to a constant, as

$$\mathbf{B}_0 = \begin{pmatrix} 0 \\ 0 \\ B_0 \end{pmatrix} \tag{3.9}$$

throughout the whole simulation box (see e.g. Wang and Abel, 2009, Pakmor and Springel, 2013). However, this approach can lead to some numerical problems, as the Alvén wave speed

$$v_A = \frac{B}{\sqrt{4\pi\rho}} \tag{3.10}$$

becomes very large at the simulation box boundary, where the density falls off by many orders of magnitude, and the magnetic energy accreted at late time will be much larger, comparatively to the gas internal or gravitational energy, than the magnetic energy accreted at early time. A constant magnetic field would also not be realistic, since a frozen-in magnetic field following the collapse of the hot gas in hydrostatic equilibrium into a dark matter halo should scale as $|\mathbf{B}| \propto \rho^{2/3}$.

Combined with the aforementioned solenoidality constraint, this requires a more complex field topology. For this purpose, as in

Chapter 2, we define the vector potential

$$\mathbf{A}_0 = B_0 \left[\frac{\rho(r,z)}{\rho_0} \right]^{2/3} r\mathbf{e}_\phi \tag{3.11}$$

where $\rho(r,z)$ is the initial gas density given by the NFW profile and $\mathbf{e}_\phi$ is the unit vector along the toroidal direction. The initial magnetic field is then set as the curl

$$\mathbf{B}_0 = \nabla \times \mathbf{A}_0, \tag{3.12}$$

so that it has exactly zero divergence by design. The corresponding magnetic field has a vertical component which is symmetric with respect to the mid plane, while its radial component is antisymmetric so that its shape resembles that of a dipole.

3.4 Results

The gas, though initialised in hydrostatic equilibrium, immediately starts to cool radiatively and loses thermal energy. The spherical structure collapses onto a rotationally supported disk in only a few Myr. This causes the gas disk to fragment into clumps denser than the star formation threshold and the first stars form. Their supernova explosions drive outflows that reach out several kpc above and below the galactic midplane and quickly, a self-regulated galactic fountain is established, where dissipative processes such as cooling and shocks balance off kinetic energy injection through supernovae explosions. The resulting kinematic properties are in very good agreement with those of observed nearby isolated dwarf galaxies (Teyssier et al., 2013).

This galactic fountain turns the whole galaxy into a giant "washing machine" that maintain a very high level of turbulence, injected on very large scales, namely the scale of the entire galaxy. Line-of-sight projections of density, velocity and temperature are plotted in Figure 3.1. The small-scale structure with clumps and filaments is clearly visible. Hot bubbles resulting from SN explosions, with temperature between 10^5 and 10^6 K, rise until the gas can cool down and falls back to the midplane, so that instead of ordered rotation, we see a highly turbulent velocity field configuration.

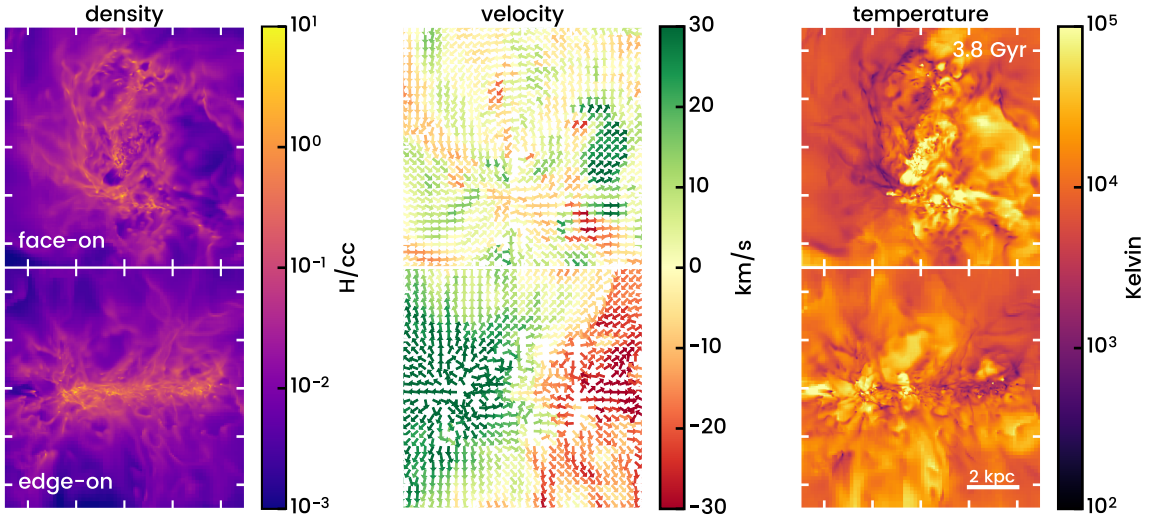

Figure 3.1: Line-of-sight projections for different plasma properties looking face-on (top row) and edge-on (bottom row) in the central 10 kpc cube in the $\Delta x = 18\,\mathrm{pc}$ (lower resolution) simulation at the simulation time $t = 3.8\,\mathrm{Gyr}$. Left: density $\langle\rho\rangle$ Center: velocity Right: temperature

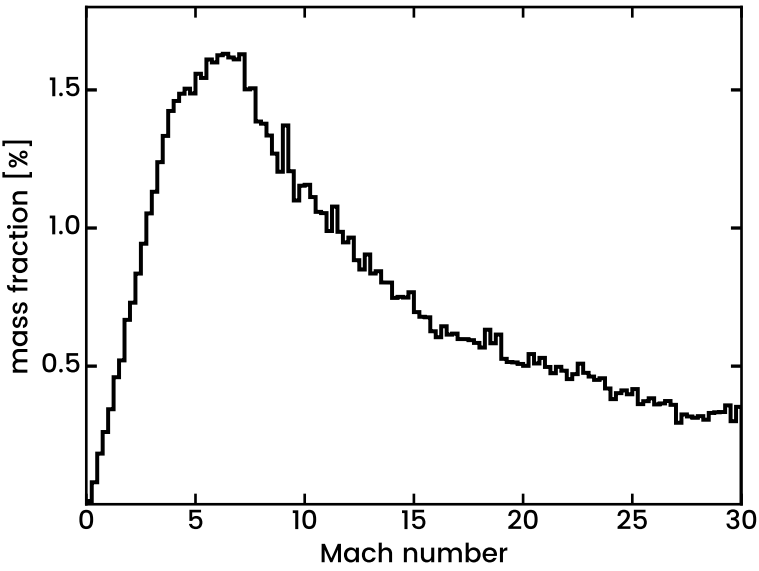

Figure 3.2: Mass histogram of local cell Mach number in the simulation snapshot at $t = 2\,\mathrm{Gyr}$. The flow is highly supersonic with most of the mass at $M \approx 6 - 7$.

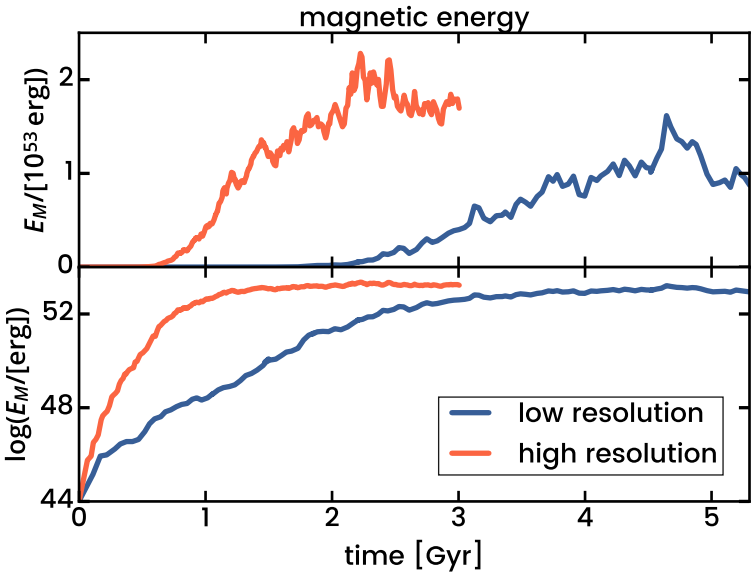

Figure 3.3: Magnetic energy evolution in linear scale (top row) and logarithmic scale (bottom row) for $\Delta x = 18\,\mathrm{pc}$ (low resolution) and $\Delta x = 9\,\mathrm{pc}$ (high resolution). The high resolution run was run until 3 Gyr due to computational resource constraints.

Since the gas is not isothermal, the flow Mach number $\mathcal{M} = v/c_\mathrm{s}$, where v is the local gas velocity and c_s is the local sound speed, is a non-trivial parameter to determine. Nevertheless, we would like to make a good estimate of the typical Mach number in our flow. We plot in Figure 3.2 a mass-weighted histogram of the Mach number for every cell. We find that the flow is highly supersonic, with most of the gas mass at the Mach number in the range of $\mathcal{M} \approx 6 - 7$.

3.4.1 Saturation of the small-scale dynamo

As demonstrated in Chapter 2, the strong turbulence injected on large scale by the galactic fountain triggers a small-scale dynamo that amplifies the magnetic field exponentially fast. The time evolution of the

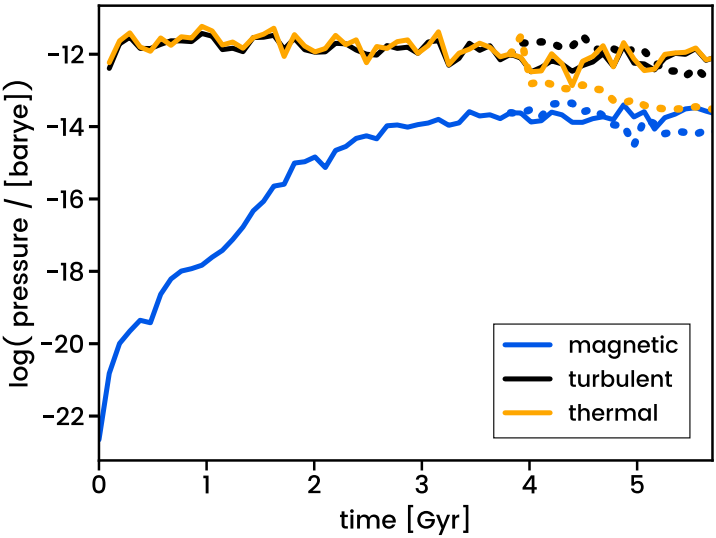

Figure 3.4: Time evolution of thermal, turbulent and magnetic plasma pressure components in central 3 kpc cube for the feedback run (solid) and the subsequent evolution when supernova feedback is suspended (dashed).

total magnetic energy inside the whole simulation box is given in Figure 3.3, using both a linear and a logarithmic scale. The initial simulation phase is characterised by an exponential growth, typical of a fast dynamo in the kinematic regime, for which the field strength is too weak to have an effect on the flow. We measured a best-fit exponential growth rate of $\Gamma \simeq 3.3\,\mathrm{Gyr}^{-1}$. This exponential amplification continues until the magnetic field becomes strong enough for the Lorentz force to back-react on the velocity field: the dynamo enters its non-linear phase. At that point, which is after $t_{\mathrm{nl}} \simeq 2.3\,\mathrm{Gyr}$, the growth rate of magnetic energy becomes weaker and transitions into the onset of the saturation phase, where the growth is now linear in time, and not exponential anymore. Eventually, the field strength becomes so high that the dynamo saturates completely and the field amplification stops, in our simulation after a time of $t_{\mathrm{sat}} \simeq 3.8\,\mathrm{Gyr}$.

In order to study the saturation level of the magnetic field, it is essen-

tial to measure the kinetic energy density of the turbulence. Defining and computing the turbulent energy in a realistic galactic environment is however not as easy as in periodic boxes with forced or decaying turbulence. In our case, gas motions are dominated by the ordered galaxy rotation and quasi-random supernova explosions, both confined inside the stratified gravitational potential of the combined disk and dark halo system.

As a proxy for turbulent energy, we use here the kinetic energy density of the velocity component perpendicular to the disk

$$P_{\rm turb} \sim \frac{1}{2}\rho u_z^2 \tag{3.13}$$

since it is not affected by galactic rotation. The time evolution of the thermal, turbulent and magnetic energies, averaged in a cube of 3 kpc in the centre of the galaxy, is shown in Figure 3.4. One can see that thermal and turbulent pressures are of the same order of magnitude, at approximately 10^{-12} erg/cc during the entire simulation. The magnetic pressure, on the other hand, defined as $P_{\rm mag} = \frac{1}{8\pi}B^2$, increases first exponentially, and then, at the onset of the non-linear dynamo phase, reaches only one per mil of the turbulent energy, corresponding also to a plasma $\beta = P_{\rm therm}/P_{\rm mag} \simeq 700$. At the end of the simulation, when the dynamo is fully saturated, the average magnetic energy reaches a strength of 10^{-14} erg/cc, which is 2.5% of the turbulent pressure, corresponding also to $\beta \simeq 40$.

Figure 3.5 shows volume-averaged line-of-sight projected maps of the different pressure components. One can clearly see that both thermal and turbulent pressure are relatively diffused and homogeneous, with only a few hot bubbles associated to supernova explosions appearing as distinctive features. The magnetic pressure map, on the other hand, is much more structured, with some striking filamentary features, resulting from a complex dynamo process. The magnetic pressure inside these filaments exceeds $10^{-12}\,\mathrm{barye}$, corresponding to a field strength $B > 1\,\mu\mathrm{G}$.

We additionally plot the ratio of the magnetic to turbulent energy in Figure 3.6 (left panel) to evaluate to strength of the field at saturation. Although the magnetic energy (or pressure) averaged over some volume is always (sometimes significantly) below equipartition (even after the saturation, as shown in Figure 3.4), we can now see that the

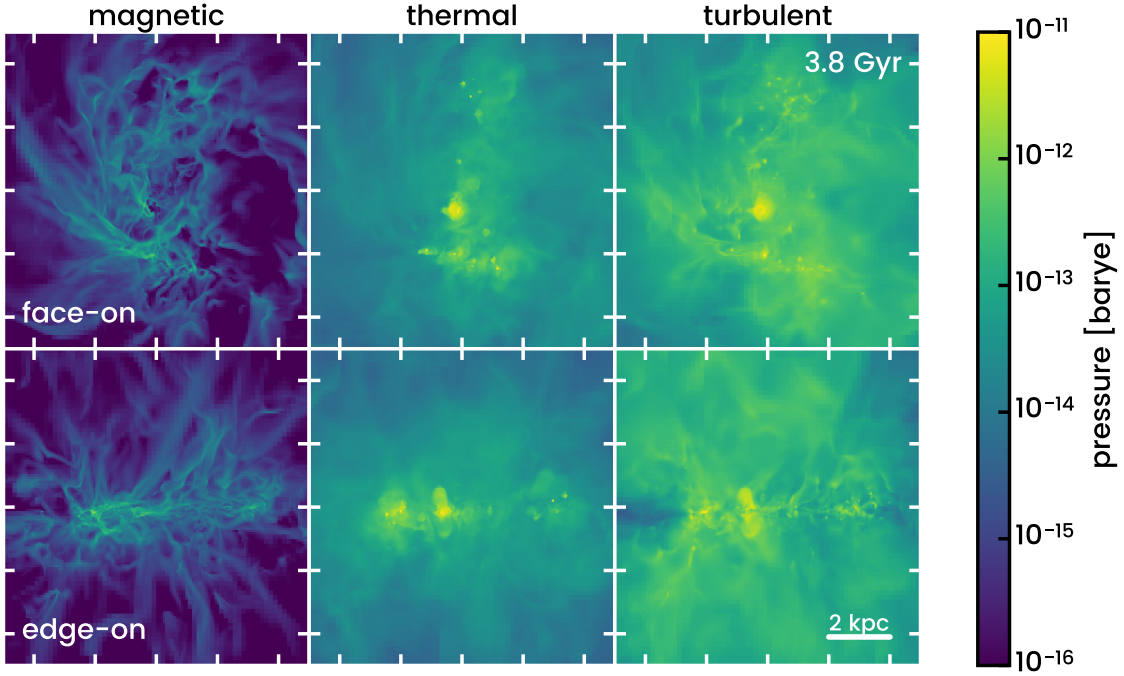

Figure 3.5: Volume-weighted average magnetic (left), thermal (center), and turbulent (right) pressure components along line of sight, looking face-on (top row) and edge-on (bottom row) in the $\Delta x = 18\,\mathrm{pc}$ (lower resolution) simulation at the simulation time $t = 3.8\,\mathrm{Gyr}$. Each panel covers 10 kpc, where every tick marks a distance of 2 kpc.

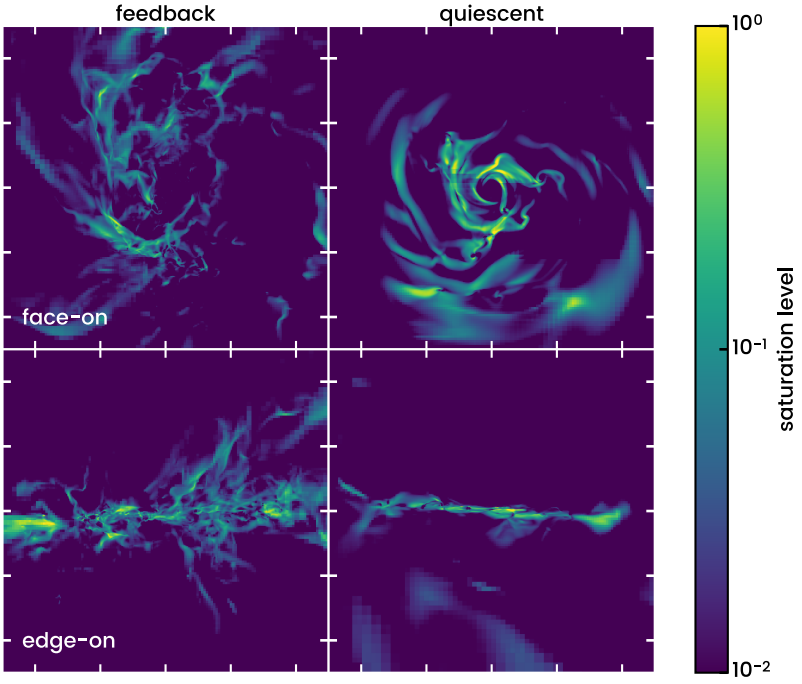

Figure 3.6: Ratio of magnetic to turbulent pressure maps with feedback at time $t = 3.8\,\mathrm{Gyr}$ (left) and after feedback was switched off at the simulation time $t = 5.6\,\mathrm{Gyr}$ (right), looking face-on (top row) and edge-on (bottom row). Each panel covers 10 kpc, where every tick marks a distance of 2 kpc.

field has actually reached equipartition in localised regions, usually associated with these strongly magnetised filaments.

We plot in Figure 3.7 the spectra of the magnetic and kinetic energy inside the galaxy. The kinetic energy spectrum stays roughly constant over time and exhibits a characteristic power-law behaviour $E_{\rm kin} \propto k^{\alpha}$ with a best fit for $\alpha = -1.8$, which is between the theoretical values of $\alpha = -5/3$ for incompressible Kolmogorov turbulence and $\alpha = -2$ for highly compressible, shock-dominated Burgers turbulence. The magnetic energy spectrum develops also the characteristic shape predicted by Kazantsev's theory, with a power law on larger scales with index 1.5, bottlenecked at small scales because of magnetic diffusion. During the kinematic phase, the magnetic energy power spectrum peaks at a length scale $\ell_{\rm peak} \simeq 500$ pc, and progressively shifts to larger scales until it reaches saturation, with a final peak length scale of $\ell_{\rm peak} \simeq 1\,{\rm kpc}$. This rather large spatial scale is a fundamental prediction of our theoretical calculations, and is justified by the very large spatial scale (around 10 kpc or more) at which the galactic fountains injects turbulent energy into the magnetic dynamo.

Interestingly, our saturated dynamo being strongly coupled to a large scale galactic fountain, we are in a position to provide strong observational predictions on the strength of the magnetic field around high-redshift galaxies. Indeed, magnetic fields in the circumgalactic medium can be detected by the Faraday rotation of polarised emission from background sources, with impact parameters as large as the virial radius of the parent halo (Bernet et al., 2008). We plot in Figure 3.8 the radial profiles of the mean gas density, the gas metallicity and the magnetic field strength averaged in spherical shells around the galaxy out to the virial radius at 30 kpc. We can see that the galactic fountain is polluting the IGM around the galaxy, with a metallicity of $Z \approx 0.2 Z_{\odot}$ and the magnetic field strength declining from μG to a tenth of a nG, and the gas density from $1\,{\rm H/cc}$ to $\sim 10^{-4}$ H/cc.

3.4.2 Effect of Resolution

The small-scale dynamo growth rate increases with the effective Reynolds number, which in our case is set by the numerical diffusion of our Godunov scheme. In order to study this numerical effect, we increase the resolution by one level to reduce both magnetic diffusion and

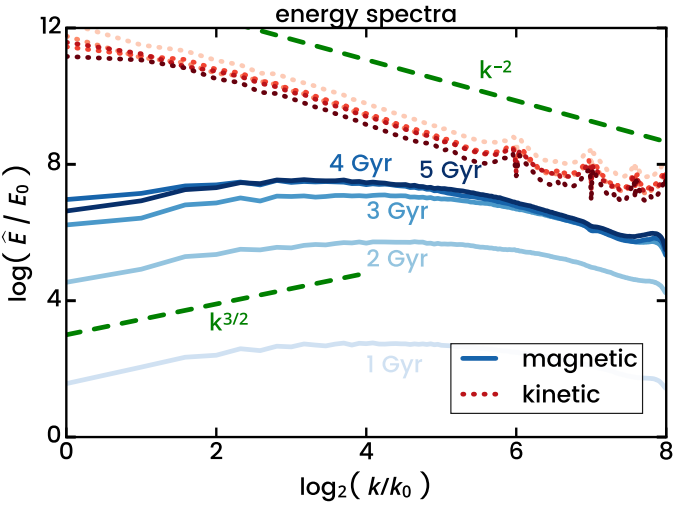

Figure 3.7: Spectra of kinetic and magnetic energies in central 512^3 cube box at grid resolution, resulting in cube size of 9.4 kpc. The normalization factor E_0 is the initial magnetic energy integrated over the whole spectrum.

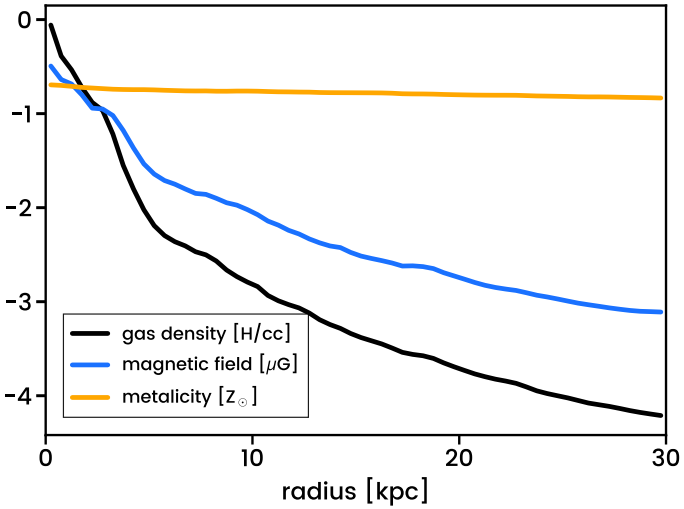

Figure 3.8: Radial profiles of average gas density, metalicity, and magnetic field strength in spherical shells around the galaxy out to large radii from the galaxy with strong feedback.

kinematic viscosity, so that both effective Reynolds numbers (magnetic and kinematic) become larger. Due to limited computational resources, we could only run this simulation for 3 Gyr. However, since the dynamo operates more than twice as fast at this increased resolution, it reached saturation before the lower resolution run.

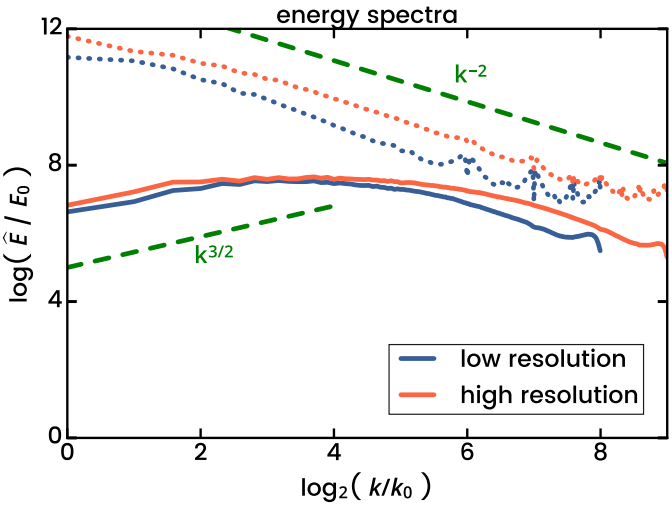

Figure 3.9: Comparison of the spectra at saturation in the low-resolution run to the kinetic and magnetic energy spectra in the high-resolution run with 1024^3 *points.*

The magnetic energy evolution for this high-resolution run is plotted alongside the low resolution evolution in Figure 3.3. The behaviour is qualitatively the same for both. However, the growth rate in the kinematic phase is larger with $\Gamma \simeq 9.4\,\mathrm{Gyr}^{-1}$ in the high resolution case. Consequently, the onset of the non-linear dynamo phase happens earlier. The overall magnetic energy level at saturation is slightly higher than in the low-resolution run, so that the magnetic field saturates at 5% of turbulent energy density, corresponding also to a final plasma $\beta \simeq 20$.

We plot in Figure 3.9 the kinetic and magnetic energy spectra from the last snapshot of the high resolution run, compared to the same

spectra at saturation for the low resolution run. The high-resolution kinetic spectrum has the same turbulent slope as the low-resolution one, with however a slightly higher amplitude, owing to the slightly more efficient star formation efficiency and associated supernovae feedback. The magnetic spectra for the high resolution run also agrees well with the low resolution one at large scale, with however slightly more power on small scales, due to the decrease of the effective dissipation length. This results in a slight shift of the peak scale from $\ell_{\rm peak} = 1$ kpc to $\ell_{\rm peak} = 0.7$ kpc.

3.4.3 Transition to Quiescence

We have seen in the previous section that in the active, early phase of its life, dominated by stellar feedback, a galaxy with a fully developed turbulent fountain can power a small-scale dynamo that efficiently amplifies an initially weal seed magnetic fields to saturation. Naturally, one might wonder what would happen to this sub-equipartition field, if feedback becomes weaker. Indeed, present-day galaxies like the Milky Way have thin and quiescent disks, with a modest level of turbulence and a small kinetic energy injection scale around 100 pc, traditionally associated to the thickness of the gas disk or to local supernova super-bubbles (Ferriere, 1992). For that purpose, we rerun the simulation from our snapshot at 4 Gyr but with supernova feedback turned off and let it evolve for a couple of Gyr.

In Figure 3.10, we show images of our galaxy at time 5.6 Gyr, 1.6 Gyr after feedback has been switched off. Without feedback to drive the turbulence anymore, the galaxy has entered a quiescent phase where the gas has cooled down and collapsed into a thin, although clumpy, rotationally supported disk, with a clear spiral structure. The velocity field is dominated by a strong rotational component, anti-clockwise in this image, which means that the spirals are trailing.

The evolution of the thermal, turbulent and magnetic pressure components is shown with dashed lines in Figure 3.4. The average magnetic energy density decreases only slightly when the disk enters this new phase and remains at a level of 10^{-14} erg/cc. At the same time, we can see a clear drop in thermal energy density and, less pronounced, in the turbulent component. The latter, however, since we use the vertical gas velocity component as a proxy for turbulence,

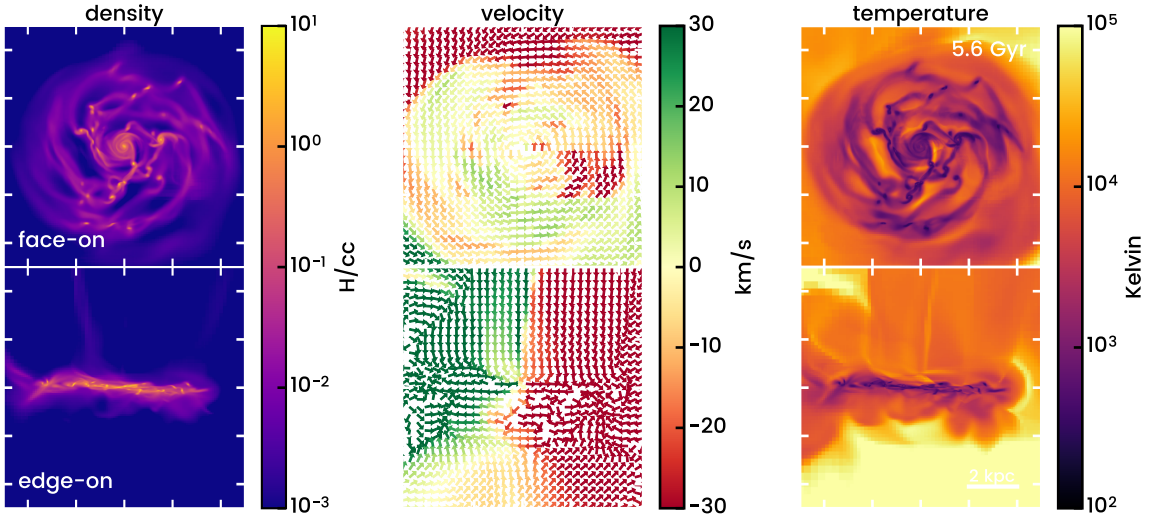

Figure 3.10: Volume-averaged line-of-sight projections for different plasma properties looking face-on (top row) and edge-on (bottom row) in the central 10 kpc cube in the $\Delta x = 18\,\mathrm{pc}$ (lower resolution) simulation at the simulation time $t = 5.6\,\mathrm{Gyr}$, or 1.6 Gyr after feedback was switched off. Left: density Center: velocity Right: temperature.

is still contaminated by a vertically collapsing flow.

To characterise the magnetic field strength in our thin disk galaxy even further, we compare the magnetic pressure to the gas thermal and turbulent energy densities side-by-side, by plotting line-of-sight projections of all three pressure components in Figure 3.11. The contamination of our turbulent energy proxy by the vertical collapse is clearly visible from the in-falling gas above the disk. While all three components have significantly decayed inside the galactic corona (except for the vertical component of the velocity field), they all remain strong inside the disk. Notably, the energy density of the magnetic field is now in equipartition with the other two energies inside the galactic arms, exceeding $10^{-12}\,\mathrm{barye}$, which amounts to field strengths greater or around $1\,\mu\mathrm{G}$. We have also plotted the ratio of the magnetic to turbulent pressure in the quiescent case in the right panel of Figure 3.6. The ratio reaches unity inside the arms, meaning that the magnetic field is in fact *locally* in equipartition with turbulence and thermal pressure in the dense galactic arms of our thin disk. The increase of this ratio is caused by a decrease of the turbulent energy density.

In order to characterise the magnetic field topology, we plot in the top panel of Figure 3.12 the toroidal, radial and vertical components of the field, as a function of the disk height, averaged within cylindrical shells of different sizes, parallel to the disk plane. On can see that after the collapse of the fountain into a thin disk, the vertical component of the field cancelled almost entirely, leaving only a dominant toroidal component, with a clear even-symmetry with respect to the disc plane, and a very weak average radial component. We argue here that this quadrupole symmetry is a natural consequence of a random magnetic field collapsing into the midplane, with a cancellation of odd-symmetric modes and a strengthening of even-symmetric ones during the formation of the thin disk. On the other hand, one also clearly sees sign reversals in the average toroidal component, so that its average over the entire disk remains very small.

In Figure 3.13, we plot the three magnetic field components as a function of radius, averaged over very thin cylindrical shells of thickness $H = 40$ pc. Inside the innermost region up to 1 kpc, the magnetic field is dominated by the toroidal field component with field strengths up to $1\,\mu\mathrm{G}$. One can also see in the radial profile significant

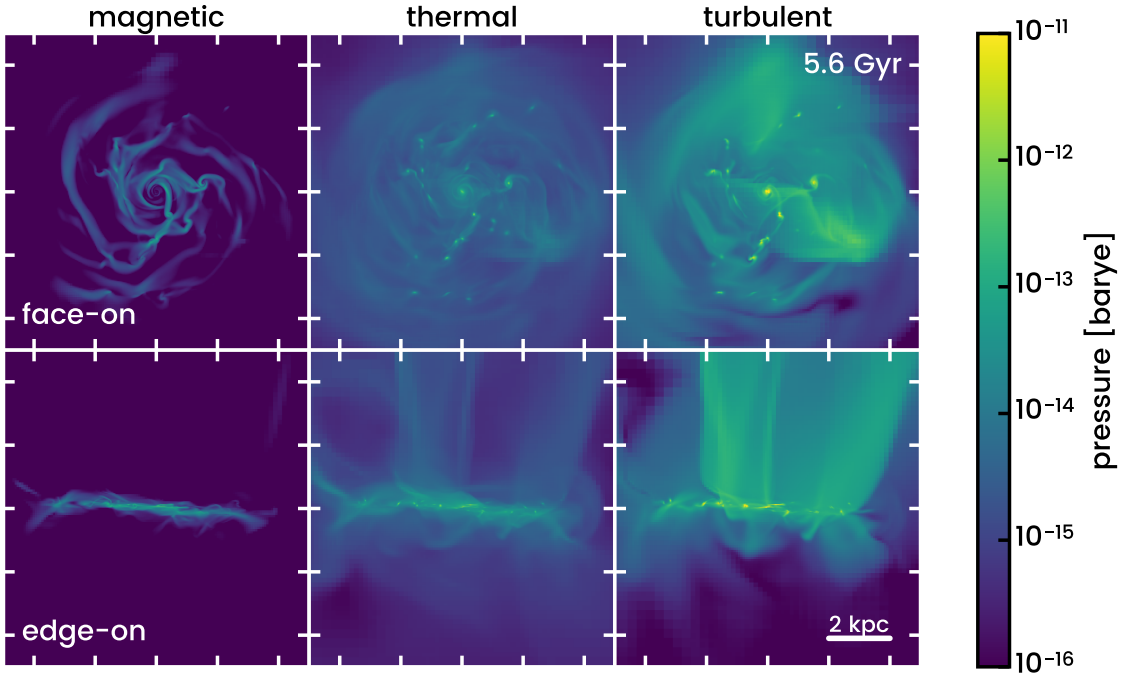

Figure 3.11: Volume-weighted average magnetic (left), thermal (center), and turbulent (right) pressure components along line of sight, looking face-on (top row) and edge-on (bottom row) in the $\Delta x = 18\,\mathrm{pc}$ (lower resolution) simulation after feedback was switched off at the simulation time $t = 5.6\,\mathrm{Gyr}$. Each panel covers 10 kpc, where every tick marks a distance of 2 kpc.

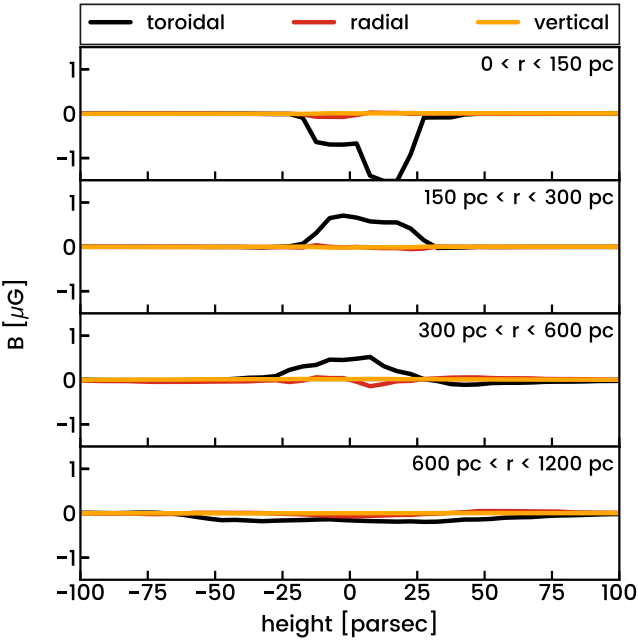

Figure 3.12: Average toroidal, radial and vertical magnetic field components as a function of the height relative to the mid-plane of the quiescent disk in cylindrical shells of different sizes.

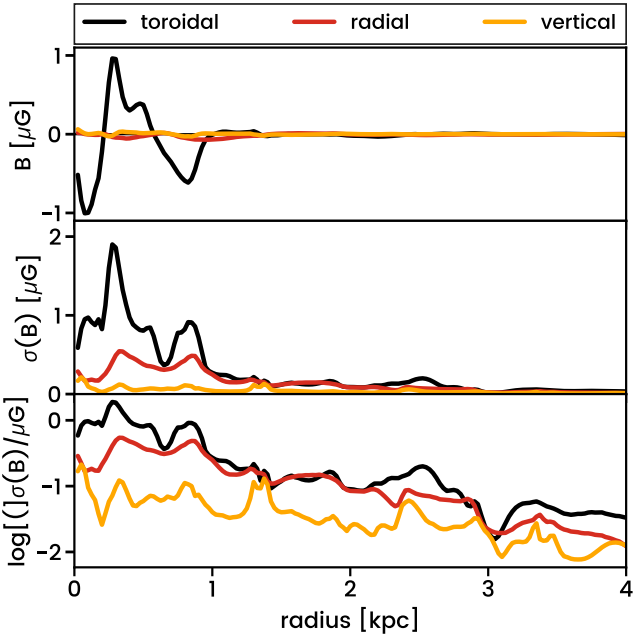

Figure 3.13: Averaged profiles of magnetic field (top panel) *and its standard deviation* (middle panel) *for the toroidal, radial and vertical field components along the radius in cylindrical shells around the quiescent galaxy. The standard deviation is also plotted in logarithmic scale* (bottom panel) *to illustrate the difference in strength of each component.*

sign reversals of the toroidal component. These sign reversals are a clear relic of the small scale dynamo in the feedback-dominated corona prior to the collapse, and are also tightly connected to the spiral pattern. In the lower panel of Figure 3.13, we show the standard deviation of the three field components, averaged within the same small cylinders. This quantity is a measure of the field strength at small scale, and reaches 1 μG for the toroidal component, roughly in equipartition with the mean field. The standard deviation for the vertical component is almost zero, while the small scale radial component has a field strength around 0.3-0.4 μG.

To quantify and illustrate the relative strength of the radial and toroidal components better, we show the magnetic field line directions $B_\perp$ perpendicular to the line of sight in a face-on view of the average magnetic field in Figure 3.14, together with a histogram of the pitch angle

$$p_B = \arctan \frac{B_r}{B_t}. \tag{3.14}$$

which is a common observable when measuring galactic magnetic fields. The magnetic field is strongest inside the trailing main arms which also coincide with the dense gas arms. Its field lines are generally aligned with the arm structure in the arms and otherwise mostly pointing along the toroidal direction (sometimes parallel, sometimes anti-parallel). We find that the pitch angles are symmetrically distributed around a mean pitch angle of $\langle p_\mathrm{B} \rangle = -12.4\,^\circ$ with a standard deviation of $\sigma(p_\mathrm{B}) = 35.1\,^\circ$. Note that these negative pitch angles are a clear indicator of magnetic field alignment with the spiral structure of a trailing spiral galaxy and change sign because of the field reversals.

3.5 Discussion

We have set up magnetohydrodynamical simulations of an isolated cooling dwarf halo which hosts a galaxy with strong turbulence driven by supernova feedback. The gas component features high Mach number flows with up to $M \approx 10$ and a kinetic energy spectrum with a characteristic slope between incompressible Kolmogorov and highly compressible shock-driven Burgers turbulence. Just as in Chapter 2, the magnetic seed field is quickly amplified by a small-scale dynamo. The magnetic energy spectrum has the typical bottlenecked $3/2$-slope on large scales which peaks near the resistive scale and falls off on smaller scales as predicted by dynamo theory (Kulsrud and Anderson, 1992). The global magnetic field time evolution in our experiment can be divided into three distinct phases:

1. exponential growth (kinematic phase)
2. constant growth (non-linear phase)
3. zero growth (saturation)

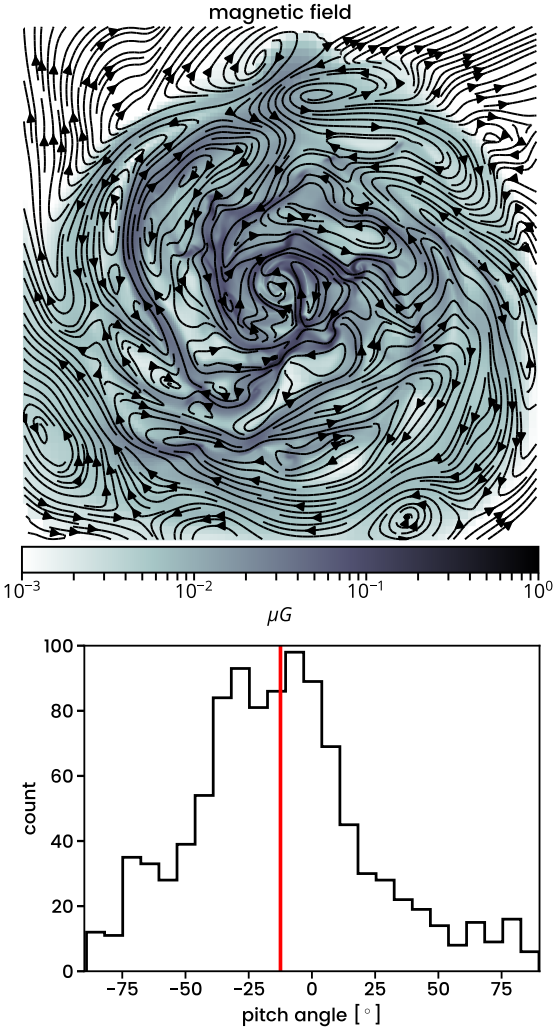

Figure 3.14: Magnetic field line directions on top of a line-of-sight averaged magnetic field map in a face-on view (top panel) *and the count histogram of pitch angles in above image* (bottom panel). *The red line marks the mean pitch angle* $\langle p_{\mathrm{B}} \rangle = -12.4\,^{\circ}$ *with a standard deviation of* $35.1\,^{\circ}$.

During the exponential growth phase, the e-folding times are $\sim 300\,\mathrm{Myr}$ with lower resolution and $\sim 100\,\mathrm{Myr}$ with higher resolution. Since the dynamo growth rate increases with the Reynolds numbers of the flow, it could potentially become very large if we were not constrained by our limited computational resources. Estimating the Reynolds numbers in a simulation with numerical viscosity and diffusivity can be very difficult when not using explicit terms in the system of equations and when complicated flows are involved. As a lower limit, we can take the numerical diffusion of a first-order method which is given by

$$\mathrm{Re_N} = 2\frac{L}{\Delta x} \tag{3.15}$$

with the typical length scale of the system L and the spatial resolution Δx. This would give values for $\mathrm{Re_N} = 100$ in the lower resolution case and 200 for the higher resolution in our simulations. Generally, in this kind of simulations, both the kinematic as well as the magnetic Reynolds number will range between a few 100 and 1000. We can compare this to a typical ISM with an estimate for the ISM viscosity (Spitzer, 1941)

$$\mathrm{Re} = \sqrt{3\gamma} M \frac{L}{\lambda} \tag{3.16}$$

where λ is the mean free path of a hydrogen atom and M is the Mach number. At a density of $1\,\mathrm{H/cc}$ and a Mach number of 5 the Reynolds number will be $\mathrm{Re} = 10^7$. The magnetic Reynolds number computed from the Spitzer resistivity formula at $T = 10^4\,\mathrm{K}$ is even larger with $\mathrm{Rm} = 10^{21}$, yielding the magnetic Prandtl number $\mathrm{Pm} = 10^{14}$. Schober et al. (2015) derive a scaling for the small-scale dynamo growth rate in the case of large Pm and supersonic turbulence as

$$\Gamma \propto \mathrm{Re}^{1/2} \tag{3.17}$$

meaning that we can extrapolate the growth rate we measured in our simulation to expected ISM Reynolds numbers obtaining the growth rate with a realistic galactic small-scale dynamo of $\Gamma = 1000\,\mathrm{Gyr}^{-1}$ and an e-folding time of just $\tau = 1\,\mathrm{Myr}$ respectively.

After this kinematic phase, the dynamo becomes non-linear where we see that the exponential magnetic field growth slows down. The

underlying reason is that, although the magnetic energy density is still low, the Lorentz force term in the momentum equation

$$\mathbf{J} \times \mathbf{B} = (\mathbf{B} \cdot \nabla)\,\mathbf{B} - \nabla \cdot \left(\frac{1}{2}\mathbf{B}^2\right) \tag{3.18}$$

can still be strong enough for the magnetic field to backreact due to the first term on the right-hand side, the magnetic tension force. It will become strong enough to counterbalance the advection term $\mathbf{u} \cdot \nabla \mathbf{u}$ and suppress further growth on scales smaller than the stretching scale (Schekochihin et al., 2004). The magnetic energy growth will then be identical to the constant Kolmogorov energy flux.

At the time of saturation, the magnetic-to-turbulent pressure ratio is between 2.6% in the lower resolution case and 5% for the higher resolution. All of this is in agreement with the theoretical results of Schober et al. (2015) who predict the same three-phase evolution and give expected saturation levels. Although those numbers apply only in the limiting cases of very small or very large magnetic Prandtl numbers, they are still consistent with our result lying in between due to $\mathrm{Pm} \sim 1$ from both Reynolds numbers being dominated by the numerical scheme. The saturation values are also in agreement with prior numerical studies, such as Federrath et al. (2011) who find 2% with $\mathrm{Pm} = 2$ and solenoidal forcing at Mach 10 and Federrath et al. (2014) who find 3% for $\mathrm{Pm} = 2$ and 5% for $\mathrm{Pm} = 5$ (both at Mach 11). The same holds for Tricco et al. (2016) who report saturation ratios between 2% and 4% and also point out a trend of an increased ratio in the case of higher resolutions. The agreement of our results with the simulations mentioned above is remarkable considering that our numerical setup differs considerably.

With the magnetic field amplified up to full saturation, albeit not yet in equipartition, we have used that configuration to observe its evolution into a quiescent disk by turning off supernova feedback, thereby removing the main driver of turbulence. We find that with the decay of turbulence, the gas cools down and falls onto a thin clumpy disk with dense arms. Inside these arms, we observe the magnetic field to be locally at equipartition with turbulence and thermal pressure, with field strengths of several μG. Field lines inside the quiescent disk are aligned with the disk plane, with a strong toroidal

component and slightly weaker radial component. These results are consistent with observations of spiral galaxies which usually have ordered magnetic field strengths of $5\,\mu\mathrm{G}$ where the magnetic energy density is at equipartition with the turbulent energy density (Beck, 2016). The toroidal as well as the radial components are symmetric across the midplane, with an average pitch angle of $\langle p_\mathrm{B} \rangle = -12\,^\circ$. This symmetry confirms measurements of the Galactic magnetic field (Mao et al., 2012) and pitch angle measurements of various nearby galaxies (Van Eck et al., 2015). Furthermore, the magnetic field reversals along the radial distance from the centre of the galaxy confirm observations of nearby spiral galaxies (Beck, 2016) where such reversals are found, usually attributed to their spiral structure.

3.6 Conclusions

We have performed numerical experiments with an idealised setup of a dwarf galaxy to study the evolution of a galactic magnetic seed field as small-scale dynamo amplification occurs due to turbulence driven by feedback processes, such as supernova explosions. We have shown that, with the formation and the death of the first massive stars, the gas swiftly becomes turbulent and the initially weak seed field grows exponentially. The e-folding time of this dynamo process becomes shorter and shorter as the numerical resolution increases. Since the Reynolds number in our simulations is several orders of magnitude lower than that of a typical ISM plasma, we extrapolate the small-scale dynamo efficiency to an e-folding time of $\tau = 1\,\mathrm{Myr}$. We conclude that even an initially very weak field strength of $B = 10^{-20}\,\mathrm{G}$ would be amplified up to dynamo saturation in a time span of only $30\,\mathrm{Myr}$. Thus, a newly born turbulent galaxy can be highly efficient in amplifying its early seed fields, whether they be primordial or generated during structure formation, extremely rapidly. This mechanism would establish considerably strong fields since the early stages of the Universe in turbulent galactic environments, which would explain the high magnetic field strengths found by Bernet et al. (2008) even at high redshift. The strong but sub-equipartition-strength field can then be further transformed by other processes like the $\alpha - \Omega$ dynamo. Moreover, the magnetic field will follow and

even influence the history of its host galaxy through decisive events such as starbursts, mergers or more quiet phases. Therefore, magnetic fields should not be neglected when dealing with problems of galaxy evolution.

4 Cosmological evolution

In the previous chapters, we have studied how weak magnetic fields can be amplified by a small-scale dynamo in a turbulent dwarf galaxy and how this dynamo saturates, all in an isolated setting without cosmological effects. In this chapter, we will investigate how such a turbulent dwarf galaxy can form and evolve from first density fluctuations at very high redshifts up to a more recent past.[1]

In this regard, we present here a new cosmological high-resolution zoom-in magnetohydrodynamic (MHD) simulation, using the adaptive mesh refinement (AMR) technique, of a dwarf galaxy with an initially weak and uniform magnetic seed field that is amplified by a small-scale dynamo driven by supernova-induced turbulence. As first structures form from the gravitational collapse of small density fluctuations, the frozen-in magnetic field separates from the cosmic expansion and grows through compression. In a second step, star formation sets in and establishes a strong galactic fountain, self-regulated by supernova explosions. Inside the galaxy, the interstellar medium becomes highly turbulent, dominated by strong supersonic shocks, as demonstrated by the spectral analysis of the gas kinetic energy. In this turbulent environment, the magnetic field is quickly amplified via small-scale dynamo action and is finally advected into the circumgalactic medium by a galactic wind.

This realistic cosmological simulation explains how initially weak magnetic seed fields can be amplified quickly in early, feedback-dominated galaxies, and predicts, as a consequence of the small scale dynamo process, that high-redshift magnetic fields are likely to be dominated by their small scale components.

[1] The work presented in this chapter has been published in the *Monthly Notices of the Royal Astronomical Society* under the title 'A small-scale dynamo in feedback-dominated galaxies - III. Cosmological simulations' following peer-review (Rieder and Teyssier, 2017b). It was also presented at the RAMSES User Meeting in Paris, France on 6th October 2016.

4.1 Introduction

Magnetic fields are ubiquitous in the Universe. They are found in planets, stars, galaxies, the intergalactic space in between them and may possibly permeate even spaces in the Universe. Their origin might be primordial (Durrer and Neronov, 2013) or due to microphysical processes at later epochs, such as the Biermann battery (Biermann, 1950) in shock fronts (Kulsrud et al., 1997) or ionization fronts (Gnedin et al., 2000), spontaneous fluctuations (Schlickeiser, 2012) or fluctuations due to the Weibel instability (Lazar et al., 2009) in the plasma of protogalaxies, or even magnetic fields released into the ISM by stars through stellar winds or supernova outbursts (Bisnovatyi-Kogan et al., 1973) or even by AGN jets (Rees, 2005) and subsequently diluted. Magnetic fields of the order of $10^{-20}\,\mathrm{G}$ can be created by microphysical mechanisms like the Biermann battery, but they might also be remnants from primordial creation. Planck Collaboration et al. (2016a) constrain the upper limit of the primordial magnetic field (PMF) strength to $10^{-9}\,\mathrm{G}$, while Neronov and Vovk (2010), Dermer et al. (2011), Vovk et al. (2012) set lower limits for the field strength ranging from $10^{-18}\,\mathrm{G}$ up to $10^{-15}\,\mathrm{G}$ based on γ-ray observations of blazar spectra. As far as galactic magnetic fields are concerned, observations from the Milky Way (Taylor et al., 2009), nearby galaxies (Beck, 2016) as well as high-redshift galaxies (Bernet et al., 2008) reveal that they are strong, usually at equipartition with the turbulent energy density. Robishaw et al. (2008) detected field strengths up to $18\,\mathrm{mG}$ in starburst galaxies but ordered galactic magnetic fields in the ISM are typically expected to be of the order of several μG. Kim et al. (2016) found a correlation between magnetic field traces and strong Mg II absorption, which indicates a link between strong outflows and a high magnetisation.

In order to explain this growth over several orders of magnitude in less than a Gyr, dynamo mechanisms are usually invoked which convert kinetic energy from gas flows into magnetic energy. Large-scale dynamos (LSD) are capable of amplifying magnetic fields coherently on large spatial scales but do so in time frames that are too slow to be viable. Contrariwise, small-scale dynamos (SSD) can function very fast where typical amplification time scales are of the order of the eddy turnover times of the smallest turbulent eddies (Brandenburg

et al., 2012). There are ongoing efforts to study its effectiveness in laser-driven laboratory experiments (Tzeferacos et al., 2017). On the theoretical side, Kazantsev (1968) laid out the foundation of a small-scale dynamo theory, for which Kulsrud and Anderson (1992) found that the magnetic energy spectrum scales with the wavenumber as $k^{3/2}$ on scales larger than the resistive scale. SSD generally create fluctuating fields without a large scale component and do not reach equipartition with the other energies. This does not conform with observations in nearby galaxies (Beck, 2015). It is likely that the magnetic fields we observe in galaxies are not the result of just one single process, but probably a combination of various mechanisms.

Fully cosmological simulations with MHD solvers have been reported since over a decade, first focusing on galaxy clusters, the intergalactic and intracluster medium (Dolag et al., 2005, Dubois and Teyssier, 2008), which have evolved into fruitful studies of its turbulence and shocks (Miniati, 2014, Miniati and Beresnyak, 2015, Vazza et al., 2017), in mostly subsonic turbulence but high Mach numbers in the shock regions. Furthermore, zoom-in simulations of Milky Way-like galaxies have been performed with the SPH code GADGET (Beck et al., 2012), and with the moving-mesh code AREPO (Pakmor et al., 2014). They found fast amplification of their initial magnetic field up to a saturation level due to supersonic turbulence. The redshift at which saturation was reached depended on the initial field strength but the field strength at saturation did not. Most recently, Pakmor et al. (2017) reported similar results based on Auriga simulations, where small-scale dynamo amplification is observed in supersonic turbulence, until dynamo saturation is reached at 10% of the turbulent energy level. The seed field with $10^{-4}\,\mu$G initial field strength was chosen extremely high, in order to observe the saturation at a redshift of $z = 2$. All those experiments were using divergence cleaning methods for the magnetic field which suffers from the problem of unphysical magnetic field divergence. Constrained Transport techniques previously only used in AMR codes, have been fitted for Lagrangian codes such as Mocz et al. (2016), which could be used in favour of divergence cleaning but have not seen widespread adoption yet.

With regard to realistic feedback mechanisms in cosmological MHD simulations, a more accurate treatment of feedback with cosmic-rays (CR) physics was developed by Pfrommer et al. (2017), who

included CR evolution equations in cosmological MHD simulations with AREPO. This opens new interesting mechanisms of magnetic field backreaction on the galaxy, such as a more strongly suppressed star formation in small galaxies due to the additional effect of CR pressure feedback.

Dwarf galaxies are the dominant galaxy population at high redshift, possibly responsible for cosmic re-ionisation (Kimm and Cen, 2014). They are also the progenitors of the Milky Way satellites, which are useful laboratories to test our current galaxy formation paradigm.

In Chapter 3, we have studied how the turbulent environment in dwarf galaxies with strong feedback-driven winds is able to drive an SSD amplifying even weak magnetic fields very rapidly, and how the resulting small-scale fields can be transformed large-scale fields once feedback becomes weaker. In this chapter, our intention is to build on that previous work and extend it to a more natural set-up with cosmologically realistic initial conditions, in order to make another step towards a better comprehension of the evolution of magnetic fields in the Universe. In Section 4.2, we explain the numerical details of our simulation, the results of which are presented in Section 4.3. We discuss these results in Section 4.4 and conclude with a future outlook in Section 4.5.

4.2 Method

We used the Adaptive Mesh Refinement (AMR) code RAMSES (Teyssier, 2002) to follow the cosmological evolution of a dwarf galaxy in a zoom-in simulation. This code simulates a self-gravitating magnetised plasma together with a collisionless fluid of dark matter and stars and additional physical sub-resolution processes such as gas cooling, star formation and supernova feedback. The ideal MHD equations are solved using a second order unsplit Godunov scheme (Teyssier et al., 2006) with a perfect gas equation of state. The gas is coupled to collisionless dark matter and stellar matter particles by the particle-mesh method. The solenoidal constraint

$$\nabla \cdot \mathbf{B} = 0. \tag{4.1}$$

is implicitly fulfilled by the Constrained Transport (CT) method proposed to solve the induction equation by (Yee, 1966) and formulated by Evans and Hawley (1988), thereby keeping the magnetic field divergence free. For a more detailed description of the numerical scheme, we refer the interested reader to Fromang et al. (2006).

Gas cooling is implemented using a standard H and He cooling function, with an additional metal cooling component and fine-structure cooling. Star particles are created as a random Poisson process according to a Schmidt law as in Rasera and Teyssier (2006) with an efficiency of $\epsilon_* = 1\,\%$. The effect of supernovae is modeled by releasing non-thermal energy into the ISM over a dissipation time scale of 20 Myr (Teyssier et al., 2013) for $\eta_{\rm SN} = 10\,\%$ of the stars. These physics parameters for cooling, star formation and supernova efficiency have been selected and tested intensively in dwarf galaxy simulations with successful dynamo action in Chapter 2 and Chapter 3 and were adopted here in a cosmological context.

We transcribed the system of equations into 'supercomoving variables' tracing the universe in the Friedmann-Lemaître-Robertson-Walker metric as described by Martel and Shapiro (1998). We chose to scale the supercomoving magnetic field with the scale factor a as

$$\widetilde{\mathbf{B}} = a^{5/2}\frac{\mathbf{B}}{B_*} \tag{4.2}$$

where $\mathbf{B}$ is the magnetic field in physical units and $B_* = \rho_*^{1/2} v_*$ is a fiducial scaling. Note that, although this definition is in contrast to the commonly used convention of a^2-scaling for $\widetilde{\mathbf{B}}$, both formulations are equivalent, and the induction equation in these supercomoving variables becomes

$$\frac{\partial}{\partial \widetilde{t}}\widetilde{\mathbf{B}} = \widetilde{\nabla} \times \left(\widetilde{\mathbf{v}} \times \widetilde{\mathbf{B}}\right) + \frac{1}{2a}\frac{\mathrm{d}a}{d\widetilde{t}}\widetilde{\mathbf{B}} \tag{4.3}$$

thereby introducing only one 'antidrag' term term to the induction equation and conveniently leaving the other MHD equations unchanged. We used the 'Multi-Scale-Initial-Conditions' tool developed by Hahn and Abel (2011), together with the 2015 Planck cosmology parameters (Planck Collaboration et al., 2016b) to generate our initial conditions. We ran a box with a comoving size of $7.5\,\mathrm{Mpc}$ from

Figure 4.1: Volume-averaged line-of-sight projections of gas density (top row) *and magnetic pressure* (bottom row) *in the central 15 kpc around the galaxy at redshifts* $z = 7, 6, 5, 4.5$ *(from* left *to* right*). The white circles mark the volume inside the virial radius.*

redshift $z = 99$ until $z = 4.5$, zooming on a high resolution region around a dwarf-sized halo with $M = 1.75 \cdot 10^{10}\,\mathrm{M}_\odot$, selected from an initial unigrid dark matter only simulation. The mass resolution for dark matter particles in the zoomed region was $M = 1.5 \cdot 10^4\,\mathrm{M}_\odot$ and $M = 7.5 \cdot 10^6\,\mathrm{M}_\odot$ in the coarse surrounding region, and we started with an initial effective resolution of 1024^3 grid cells in the zoomed region. Further refinement levels are unlocked successively as the simulated universe expands and matter condeses, ensuring that the physical resolution stays below $22.5\,\mathrm{pc}$. While low-resolution cells are refined when the mass contained within exceeds 8 times a typical mass scale M_*, we decided to be more vigorous on refining the zoomed region by lowering that requirement for the finest resolution cells since dynamo amplification is very reliant on resolving the turbulent flow. The initial magnetic field was set to be uniform, aligned with the z axis and a field strength of $B_0 = 10^{-20}\,\mathrm{G}$ in physical units, giving it a conservatively low starting value.

4.3 Results

Images of volume-averaged line-of-sight projections of gas density and magnetic pressure are rendered in Figure 4.1 at various redshifts. As the galaxy evolves through time it grows substantially from mass inflows and mergers, reaching a virial radius of $R_{200,c} = 8.6\,\mathrm{kpc}$ at redshift $z = 4.5$. With densities becoming large enough to trigger star formation, feedback processes set in and drive turbulent winds which give rise to dynamo field amplification. Indeed, we can see the overall magnetic pressure rising with its filamentary structure typical for dynamo processes inside the galaxy and carried outside into the circumgalactic medium by winds.

The evolution of the total magnetic pressure inside the 'zoomed' region is plotted in Figure 4.2 together with the expected evolution of $B \propto \rho^{2/3}$-scaling for field lines that are compressed or stretched as the cosmic structure forms and plasma matter falls into dark matter halos. The initial development is dominated by cosmic expansion where gas density and magnetic field are both diluted as the universe expands and, subsequently, density fluctuations collapse into structures. We see this decrease until the first stars have formed and supernova explo-

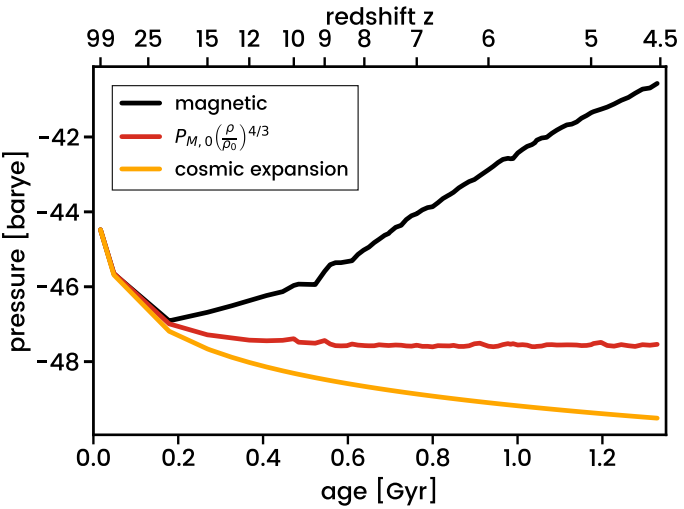

Figure 4.2: Average magnetic pressure in physical, non-comoving units (black) *inside the zoomed region as a function of time and redshift. The yellow curve shows the $B \propto a^{-2}$ evolution for a trivially expanding universe and the red curve the expected scaling when the magnetic field follows the structure formation as $B \propto \rho^{2/3}$.*

sions start to drive turbulent winds. This process sets off a continuous, self-regulating feedback process where steady mass infall triggers star formation and supernova winds push mass outwards. The resulting dynamo starts to amplify the field exponentially throughout its host galaxy's evolution history with an e-folding time $B \propto \exp(t/\tau)$ of $\tau = 65\,\mathrm{Myr}$, essentially undisturbed by merger events.

This picture becomes clearer in Figure 4.3, where we plot mass-weighted 2D log-log histograms of gas density and magnetic pressure. Assuming isotropic collapse without any field amplification processes, magnetic pressure is expected to stay on the $P_M \propto \rho^{4/3}$ line tracking the stretching or compression of the initial magnetic field when it follows the structure formation. We can see that it starts to deviate from this line towards higher magnetic pressures at high densities where stars are forming and driving turbulent winds with their feed-

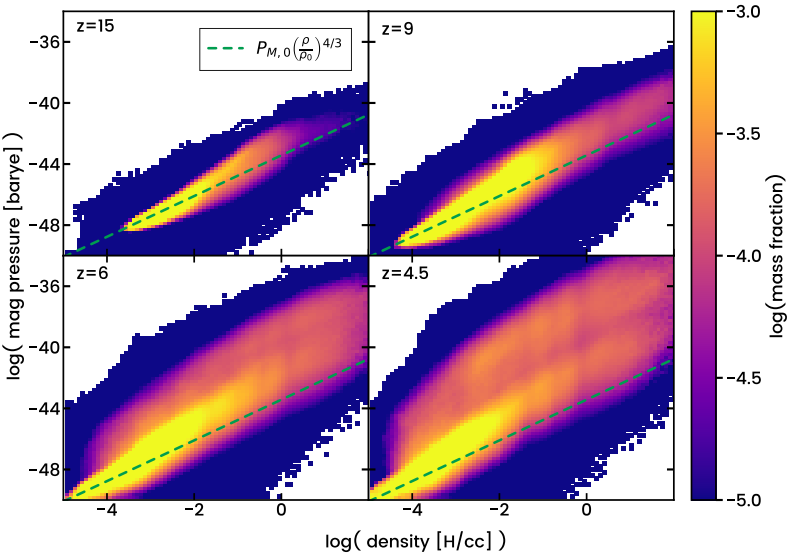

Figure 4.3: Mass-weighted 2D histograms of magnetic pressure vs. gas density at redshifts $z = 15, 9, 5, 4.5$. The dashed green line indicates the magnetic pressure resulting from stretching or compression of the initial field when it follows the structure formation as $B \propto \rho^{2/3}$.

back processes. This process continues to higher and higher magnetic pressure which then also propagates to lower densities as magnetised winds transport magnetic energy from the dense central regions out to the circumgalactic medium.

In Figure 4.4, we plot the kinetic energy spectra at several redshifts. The spectra have a clear power-law shape $E_{\rm kin} \propto k^{\alpha}$ with a best fit for α ranging between -2.04 and -2.13. This slope is close to the theoretical value of -2 predicted for highly compressible, shock-dominated Burgers turbulence. Analogously, the magnetic energy spectra are also plotted for several redshifts in Figure 4.4. It develops the typical bottlenecked power-law shape with $E_{\rm mag} \propto k^{3/2}$ on larger scales as predicted by Kazantsev's theory, and falling off below the resistive scale. We plot in Figure 4.5 radial profiles of virial and tangential velocity, turbulent and sound speed, gas density, magnetic

pressure and metalicity up to the virial radius averaged in spherical shells around the center at redshift $z = 4.5$. The turbulent speed is considerably high compared to the rotational motion of the gas and the sound speed, leading to a supersonic flow with a Mach number $\mathcal{M} \sim 2$. Both gas density and magnetic field strength fall off by two orders of magnitude from their peak at the center to the virial radius in a similar fashion. The metalicity in comparison is more uniformly blown out by the galactic winds at a value of roughly $10\,\%$ solar metalicity.

4.4 Discussion

We have performed magnetohydrodynamical simulations of a 'zoom-in' dwarf galaxy in a cosmological context, with a weak magnetic seed field to study its evolution through cosmic time. Starting from an initially uniform universe with tiny density fluctuations and a spatially constant magnetic field, we see early structure formation where matter starts to fall into the potential wells of dark matter halos. This phase is characterised by dilution of the magnetic field as the universe expands and its scale factors increases. After redshift $z \sim 20$, this global effect is counter-balanced by the accelerated collapse of gas into halo structures which also compresses magnetic field lines locally and thereby begins to dominate over the cosmic expansion. As the first stars form inside these structures, they set the stage for a self-regulating mechanism of star formation and feedback-driven energy release. Galaxies form and this energy release gives rise to strong winds stirring the interstellar medium to become highly turbulent and supersonic with kinetic energy spectra indicating a shock-dominated Burgers turbulence regime. This in turn then leads to small-scale dynamo field amplification inside the galaxy and persistently rising magnetic field strengths, with magnetic energy spectra in conformance with Kazantsev dynamo theory. As magnetic pressure builds up in the central regions of the galaxy, it is carried out into the circumgalactic medium by magnetised winds. Even though the central galaxy is subject to several merger events throughout its cosmic evolution, these events do not alter the turbulent flow process substantially and have no measurable effect on the dynamo mechanism.

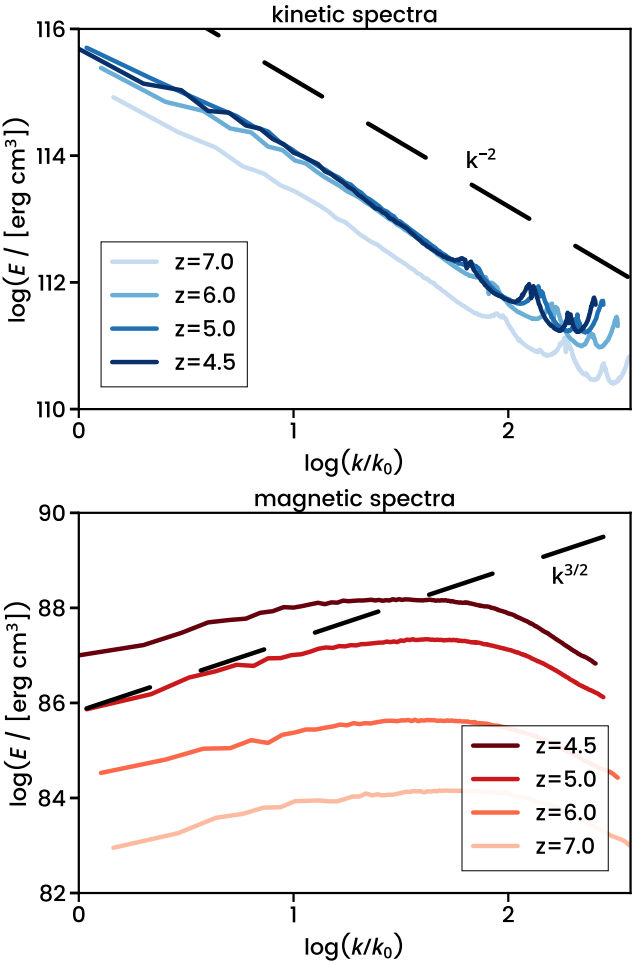

Figure 4.4: Kinetic and magnetic energy spectra in 512^3 cubes centered on the halo at various redshifts, sampled at the grid resolution.

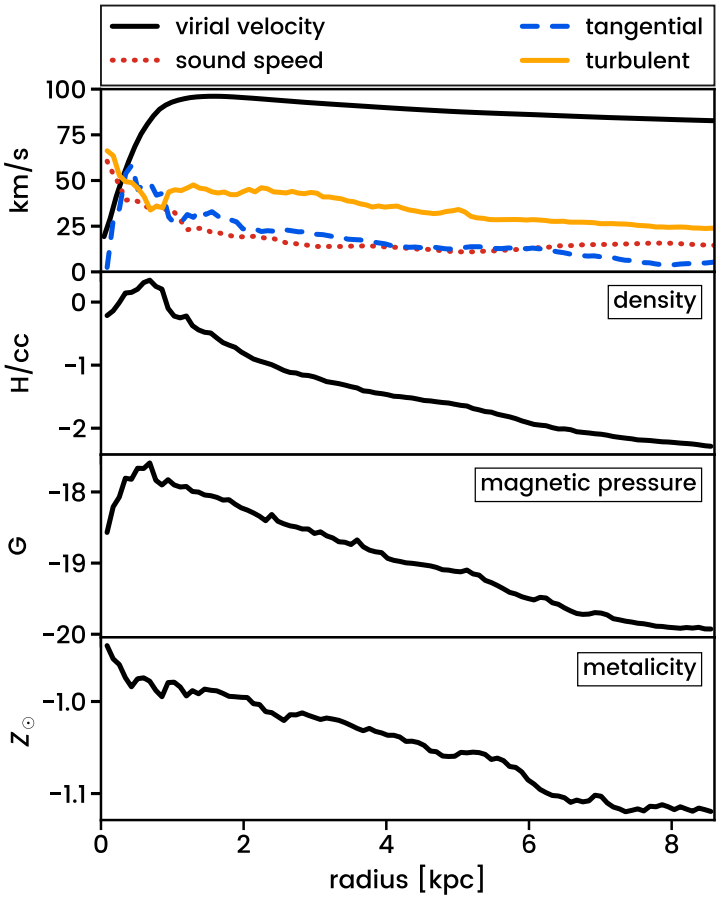

Figure 4.5: Radial profiles of various characteristic speeds, gas density, magnetic pressure and metalicity averaged in spherical shells around the center at redshift $z = 4.5$.

These results are remarkable given the difficulty of capturing turbulence in galaxy simulations, even more so for a cosmological zoom-in, where the dynamic range of resolution from large scales down to the smallest possible in order to resolve the tiniest turbulent eddies is extraordinarily demanding in terms of computational efforts. The small-scale dynamo amplification rate essentially depends on the viscosity and magnetic diffusitivity of the medium, or the kinetic and magnetic Reynolds numbers respectively. As discussed in Chapter 3, those characteristics are dominated by numerical resolution in this kind of simulation where any realistically attainable computational resolution is far from the required length scales of a realistic astrophysical plasma but can be extrapolated to 'real-world' values, predicting full amplification from seed fields to saturation in just a few Myr. Therefore, a scenario is plausible where even the very weak seed fields given by theoretical constraints are rapidly amplified inside galaxies by a small-scale dynamo process to considerable strength at very high redshift just after the first stars have formed during very turbulent phases of a galaxy's history.

Our results confirm the findings of Pakmor et al. (2017), where a small-scale dynamo was observed in Milky Way-like galaxies with comparable turbulent kinetic energy and Kazantsev magnetic energy spectra.

4.5 Conclusions

We have presented a cosmological simulation of a dwarf galaxy where magnetic fields have been amplified from weak seed fields since the early stages of the Universe in turbulent galactic environments, and they could possibly reach considerable strength if not limited by current computational capabilities. This work is an important step towards a comprehensive probing of magnetic field evolution from the early Universe after the Big Bang to the present time in a fully cosmological framework. Given the ever increasing computing power due to steady technological advance and improved software it will become feasible to shed more light on the open questions regarding the magnetic field evolution. Future simulations will have to overcome the problem of attainable high resolution required to resolve

the turbulence responsible for the dynamo mechanism and reduce the numerical resistivity. To this effect it is also worth considering the limits of the ideal MHD assumption, and how the varying ionisation fraction influences plasma properties, possibly leading to magnetic field diffusion and unsteady dynamo efficiency. Furthermore, there remains uncertainty on the nature of seed fields as there are numerous viable mechanisms in question. These matters stand to be solved by future numerical investigation.

5 Comparison to observations

In the previous chapters, we have studied magnetohydrodynamical simulations of turbulent dwarf galaxies which host a magnetic-field producing small-scale dynamo. In this chapter we shall investigate how this simulated data would compare to observational data and see if there is agreement.[1]

5.1 Faraday Rotation

To this effect, we have worked with Kwang Seong Kim during his time as a doctoral student with Prof. Simon Lilly at ETH Zürich, whose work involved analysis of Faraday Rotation Measure (RM) data from distant quasars whose polarisation carries imprints of magnetic fields in the circumgalactic media (CGM) around intervening galaxies at intermediate redshifts.

When polarised electromagnetic radiation passes through a magnetised medium, its plane of polarisation will be rotated. This effect is called Faraday Rotation and depends linearly on the square of the wavelength λ

$$\Delta\chi = \mathrm{RM}\,\Delta\lambda^2 \tag{5.1}$$

where χ is the polarisation angle, and RM is the Rotation Measure (Kim et al., 2016). In the case where all radiation in the received light beam is subject to the same Faraday rotation, the latter will be equal

[1] The results presented in this chapter are the outcome of a collaboration with Kwang Seong Kim as a doctoral student with Simon Lilly at ETH Zürich and have been presented in his doctoral thesis (Kim, 2017) which he successfully defended recently. The plot compilation and comparison to observations in this chapter were made by him, for which I am very grateful. They are based on the simulation setup and data extraction which was prepared and carried out by the author of this thesis. All images in this chapter © 2017 Kwang Seong Kim. The following results will be presented in a journal article in preparation with Kwang Seong Kim and Simon Lilly (Kim et al., 2017).

to the Faraday depth

$$\phi(z_s) = 8.1 \cdot 10^5 \,\mathrm{rad/m^2} \int_{z_s}^{0} \frac{n_e(z)\mathbf{B}(z)}{(1+z)^2} \cdot \frac{d\mathbf{l}}{dz} dz \tag{5.2}$$

which is integrated along the line of sight from the redshift of the source z_s to the observer, with n_e being the number density of free electrons in cm^{-3} and $B_\parallel$ in G is the parallel magnetic field component. If one can estimate the electron density, this will give the accumulated $B_\parallel$, however, it does not allow for conclusions where it is located and opposing fields will cancel. Furthermore, any inhomogeneities across the telescope beam that are below its resolution will taint χ and break the simple linear relation of Equation 5.1. Therefore, it is more advantageous to consider the full polarisation structure by taking the complex representation $\mathbf{P}(\lambda^2) = P(\lambda^2) \exp\left(2i\chi(\lambda^2)\right)$ of it and taking the Fourier transform

$$\mathbf{F}(\phi) = \frac{1}{\pi} \int_{-\infty}^{\infty} \mathbf{P}(\lambda^2) \exp\left(2i\phi\lambda^2\right) d\lambda^2 \tag{5.3}$$

which is called the complex Faraday depth distribution, its absolute value $F(\phi)$ the Faraday Spectrum, and its phase $\psi(\phi)$ is the effective angle of polarisation of the source. In the simple case of one intervener that is homogeneous across the plane of sight, $F(\phi)$ would have a single peak. In any other case, the analys of the full complex FD distribution permits us to 'see' more of the structure behind it.

Using this Faraday Rotation Measure Synthesis technique, Kim (2017) obtained Faraday Depth distributions and found correlation with Mg II absorption, which is associated with superwinds from starbursting galaxies (Bond et al., 2001). He found quite strong random magnetic fields of order $10\,\mu$G in the CGM of galaxies at intermediate redshifts. Another important finding is that regular fields are small compared to the random fields in these intermediate redshift galaxies, hinting at the presence of small-scale processes.

5.2 Simulated observations

One can wonder if the same techniques as in Section 5.1 can be applied to the imitated signal one would get if a simulated galaxy was

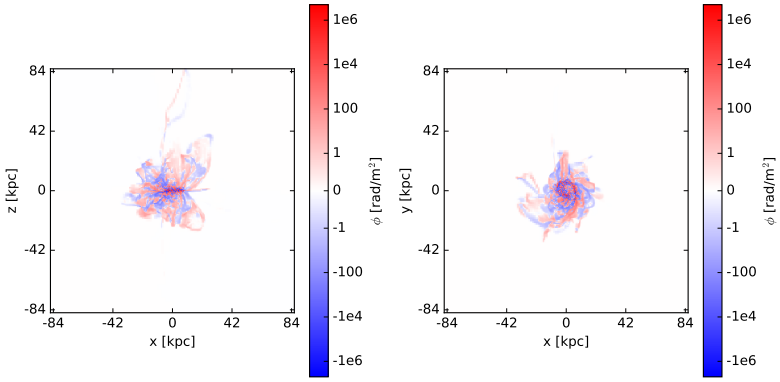

Figure 5.1: Line of sight projections of Faraday Depth ϕ edge-on (left) *and face-on* (right)*. The color scaling for ϕ is linear between -1 and 1, and logarithmic beyond. Image: Kwang Seong Kim.*

an intervener to a distant quasar. Therefore, we designed a simulation setup of the isolated Milky Way galaxy with strong feedback as described in Section 2.3.1, but with an initial magnetic field that could reach dynamo saturation during the timeframe of the simulation like we found in Section 3.4, and with strong radiation feedback with a dust opacity parameter of $\kappa = 20\,\mathrm{cm/g}$.

After turbulence has driven dynamo amplification of the magnetic field up to its saturation, we have a strong magnetic field that has grown naturally from small-scale dynamo action and is blown out into the CGM by galactic winds. We take a snapshot fiducially at simulation time $t = 3\,\mathrm{Gyr}$, after saturation was attained and use it to compute maps of the Faraday depth (Equation 5.2) as they would be seen by a telescope if it had a resolution of 84 pc, the same as the simulation grid, and assuming constant values of n_e and $\mathbf{B}$ inside each grid cell. These maps are shown in Figure 5.1 looking from the side (edge-on view) and from the front (face-on view). Strong outflows of magnetised material are clearly visible out to 30 kpc away from the galaxy. The distribution is centered around $\phi = 0$, without a preferred direction.

5.2.1 Through the telescope

This data was the basis for Kwang Seong Kim to compare to to his collected observation data, whose work will be outlined in this section. The telescopes used to collect data for Kim (2017) were VLA and ATCA. VLA's L-band angular resolution of 1.3 arcsec equates to 8.4 kpc for an object at redshift $z = 0.5$, so in order to mimic the data as though they had been observed by a similar telescope, it had to be smoothed on that scale, which corresponds to a smoothing scale of 100 pixels.

The smoothed Faraday Depth maps and their standard deviation are plotted in Figure 5.2. For the outflow regions surrounding the galaxies, it was found that the Faraday Depth distributions were bell-shaped, and that the outflow is almost radially symmetric. Therefore, we can compile radial profiles of ϕ and σ in Figure 5.3. The Faraday Depth profile shows that just outside the galaxy, the maximum $\overline{\phi}$ is reached at 20 rad/m^2, but dropping to 1 rad/m^2 and below. This is considerably lower than older observational results such as Bernet et al. (2008), but the latest findings of Kim (2017) suggest that tose RM measurements have almost always been overestimated when compared to the Faraday Depth spectrum. This is explained by the fact that the nature of random magnetic fields could not be seen in those measurements, and it turned out that they are in fact stronger than the regular fields.

The $\sigma(\phi)$ profiles in Figure 5.2 show that σ is roughly one order of magnitude stronger than ϕ itself. In order to compare the values of σ to observations, the the primary component in the observed Faraday Depth spectrum is identified and a measure of its spread σ_{PC} is computed. The range of σ_{PC} found in those observations is marked as the red shaded area. One can see that our simulated galaxy would lie within this range for beams passing by at a range between $b = 13\,\mathrm{kpc}$ and $b = 30\,\mathrm{kpc}$.

5.2.2 Ionised magnesium

Since in their observations, Kim (2017) also analyse Mg II absorption data, it makes sense to compute Mg II abundances in our simulation and compare the results. The number density of Mg II is computed as

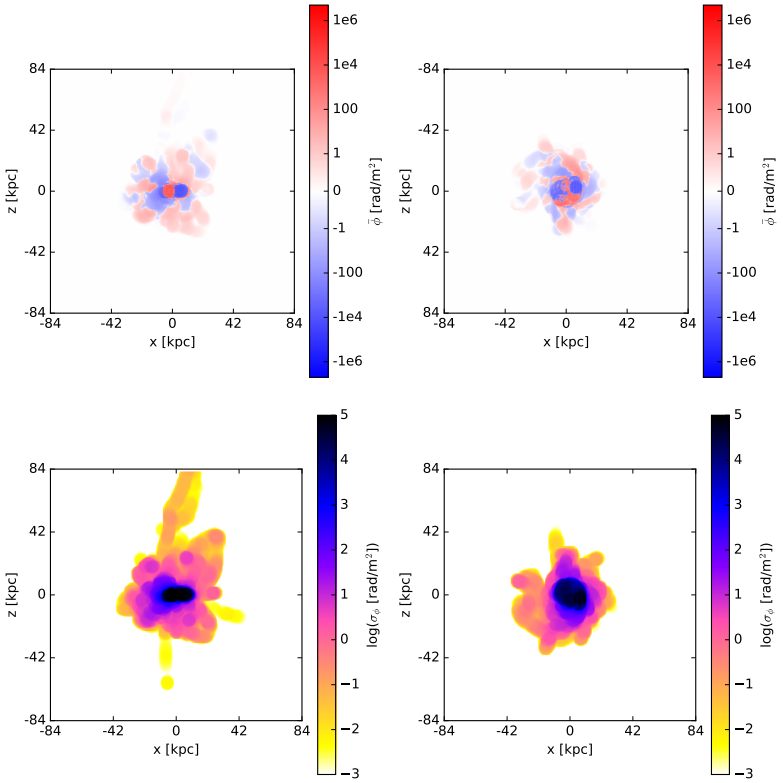

Figure 5.2: Faraday Depth maps from Figure 5.1 averaged (top) *on circles of 8.4 kpc and their standard deviation* (bottom)*. Images: Kwang Seong Kim.*

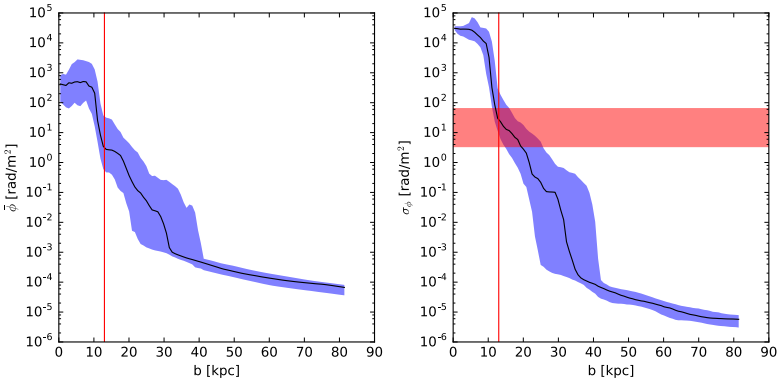

Figure 5.3: Radial profiles of Faraday Depth $\overline{\phi}$ (left) *averaged within annuli of radius b and a thickness of 400 pc and the standard deviation* $\overline{\sigma}$ (right). *The blue shades mark the 10th and 90th percentile and the red line marks the distance at which the annuli do not cover the inner part of the galaxy. The red shaded area is the range of* σ_{PC} *in the observations. Image: Kwang Seong Kim.*

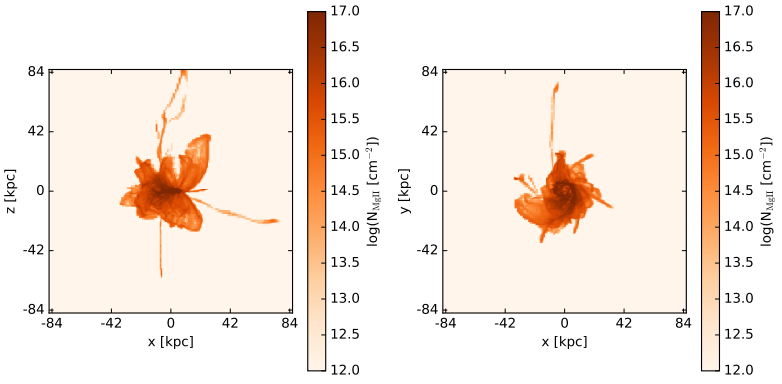

Figure 5.4: Line of sight projections of Mg II column density edge-on (left) *and face-on* (right). *Image: Kwang Seong Kim.*

$$n_{\mathrm{MgII}} = n_{\mathrm{gas}} \cdot Z \cdot f_{\mathrm{Mg}} \cdot f_{\mathrm{MgII}} \tag{5.4}$$

where Z is the metalicity, f_{Mg} is the fraction of magnesium in metals which we estimate to about 3%, and f_{MgII} is the fraction of ionised Mg II out of all magnesium atoms, which we compute from the gas temperature following the relation given in Bryans et al. (2006). The column density maps of n_{MgII} are given in Figure 5.4 and were interpreted by Kim (2017).

It is found that the column density maps are very similar to the Faraday Depth maps in Figure 5.1, linking random magnetic fields in the CGM with Mg II outflows. Observational evidence of biconical outflows that has been established (Bordoloi et al., 2011) could not be confirmed in our simulation, which is not surprising as the feedback model used was not intended to reproduce galactic winds realistically.

5.2.3 Velocity dispersion

Analogously to the Mg II column density maps, we also compute maps of the velocity dispersion $\sigma(v)$ in each pixel, so that it can be compared to the rest-frame equivalent width W_0 of the Mg II absorption lines. This quantity is assumed to be mainly due to Doppler shift and therefore the relation gives us a measurement of the velocity dispersion in the interveners via

$$W_0 = \frac{\sigma(v)\lambda}{2\sqrt{2c\ln(2)}} \tag{5.5}$$

where λ = 2796 Å is the rest-frame MgII absorption wavelength. A 2D histogram of the velocity dispersion in the simulation vs. the Faraday depth dispersion is plotted in Figure 5.5. On top are plotted observational results from Kim et al. (2016) where the velocity dispersion is inferred from the rest-frame equivalent width W_0 of the Mg II absorption lines, and plotted vs. the primary component spread σ_{PC}.

The data does not show any clear correlation between the velocity dispersion and the standard deviation of Faraday Depth. The velocity dispersions measured in the simulation seem to be higher than the most of the observed W_0. Since the equivalent width that would be observed from a heterogeneous of velocity dispersion would be more

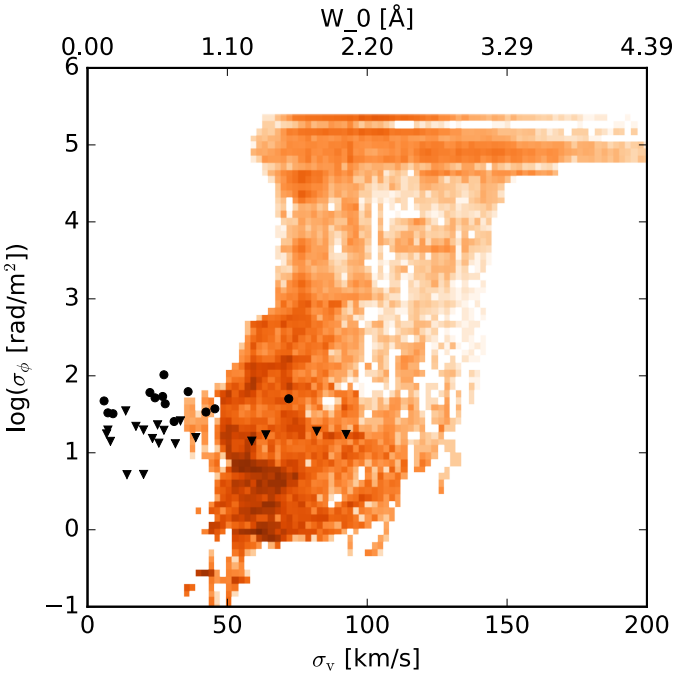

Figure 5.5: 2D histogram (counting pixels) of velocity dispersion $\sigma(v)$ in simulation data (bottom) */ rest-frame equivalent width of Mg II absorption of observations* (top) *and spread of Faraday Depth $\sigma(\phi)$, considering only Mg II column densities $N_{\mathrm{MgII}} > 10^{15}\,\mathrm{cm}^{-2}$. Sources with unresolved Faraday Depth are marked by triangles. Image: Kwang Seong Kim.*

complicated than the simple relation in Equation 5.5, it is not clear where the simulation would lie on the plot were it a single data point like the observations. Furthermore, there is only one simulation to compare, so that even if there was a discrepancy it could be a simple outlier.

5.3 Conclusions

We have investigated how the magnetic fields produced in a simulated galaxy by a small-scale dynamo compares to observations and how the dynamo-amplified magnetic fields would shape the polarisation signal of a light beam passing through its circumgalactic medium if it were observed through a telescope such as the VLA. We find that there is very good compatibility with Faraday Spectra and velocity dispersions observed from interveners at intermediate redshifts. This is especiallly remarkable considering that the simulations were designed independently from the observational work. Furthermore, recent interesting results of our collaborator Kwang Seong Kim show that regular magnetic fields in these distant interveners had previously been overestimated.

In summary, there is strong evidence of galaxies at intermediate redshift with strong outflows and turbulent magnetic fields, which suggests that these galaxies could indeed host small-scale dynamos.

6 Summary

> There is a theory which states that if ever anyone discovers exactly what the Universe is for and why it is here, it will instantly disappear and be replaced by something even more bizarre and inexplicable. There is another theory which states that this has already happened.
>
> *The Hitchhiker's Guide to the Galaxy (Douglas Adams)*

This thesis addresses the question of the origin and evolution of magnetic fields in galaxies. With a special focus on small-scale dynamo field amplification, we investigate how weak magnetic fields may have grown in turbulent dwarf galaxies to almost equipartition with the turbulent energy level. These fields could then have attained equipartition and large-scale structure at a later stage either through other dynamo processes or through reshaping by mergers, reconnection and shearing in more quiescent phases. We find that when a galaxy becomes less turbulent after the dynamo has saturated, turbulence decreases over a timescale of roughly 1 Gyr to a level where the turbulent pressure becomes comparable to the magnetic energy density. In the context of galaxy evolution theory, this supports a paradigm where magnetic fields were amplified quickly in highly active and turbulent dwarf galaxies that eventually settled down and became more quiescent, with comparable levels of magnetic and turbulent energy densities.

We also investigate how our data compares to observations and how the dynamo-amplified magnetic fields would shape the polarisation signal of a light beam passing through its circumgalactic medium if it were observed through a telescope. We find that there is remarkable compatibility with Faraday Spectra and velocity dispersions observed from interveners at intermediate redshifts, considering that the simulations were carried out independently from the observational work. In summary, there is strong evidence of galaxies at intermediate redshift with strong outflows and turbulent magnetic fields, which suggests that these galaxies could indeed host small-scale dynamos.

Building upon these findings, further investigation could open interesting new insights into the case of dynamo amplification in galaxies. For one, turbulence is very important for fast dynamos to operate, but it also requires very powerful supercomputers to be able to attain very high numerical resolutions. The steadily progressing technological improvement, along with new software that scales well on massively parallel systems will certainly allow us to advance the possibilities even further.

The small-scale dynamo growth rates that we observed are very fast, but they scale inversely with the numerical viscosity ν_{N} and numerical diffusion η_{N} which, at our current resolutions, are still very high compared to their physical counterparts in the interstellar media. Bringing them down towards more realistic values, also with respect to the magnetic Prandtl number $\mathrm{Pr}_{\mathrm{M}} = \nu_{\mathrm{N}}/\eta_{\mathrm{N}}$, which is the ratio of the two, might bring more insight into the subtleties of turbulent dynamo operation. Furthermore, the understanding of how different feedback mechanisms such as cosmic ray or radiation feedback influence the galaxy evolution with respect to magnetic fields, can be still improved.

On the large end of the scale, we have the cosmological simulations, which cannot be disregarded if one is interested in obtaining a consistent picture of magnetic field evolution 'from the beginning to the end'. Simulating a Megaparsec-scaled fully cosmological MHD system at parsec resolution may seem daunting, but might prove very fruitful in understanding galaxy evolution as a whole. Adding to this, the validity of the ideal MHD is certainly debatable, considering that those parameters will neither be constant in space nor im time and will co-evolve with other criteria such as the ionisation fraction of the plasma. There remain many open questions, such as: What is the nature of seed fields? How fast does the turbulent dynamo saturate? How is this related to its host galaxy's evolution? How does the magnetic field evolve after saturation? What role does its back reaction play? If the magnetic fields are amplified as fast as our results suggest, then they can be dynamically important early on in the history of a galaxy and might change our idea of galaxy evolution considerably. To that extent, there is also considerable potential in combining the insights of magnetohydrodynamic galaxy simulations with other advancements in the field of numerical astrophysics, such as radiation or more realistic feedback.

Finally, with new promising telescopes, notably the Square Kilometre Array (SKA), there will also be major improvements in polarisation measurements. These are of great importance in order to obtain better resolved and more robust results of galactic magnetic fields. They will certainly provide us with more answers and perhaps even new questions as well, that will then have to be addressed in the future.

Bibliography

O. Agertz, G. Lake, R. Teyssier, B. Moore, L. Mayer, and A. B. Romeo. Large-scale galactic turbulence: can self-gravity drive the observed HI velocity dispersions? *Monthly Notices of the Royal Astronomical Society*, 392(1):294–308, Jan. 2009.

O. Agertz, A. V. Kravtsov, S. N. Leitner, and N. Y. Gnedin. Toward a Complete Accounting of Energy and Momentum from Stellar Feedback in Galaxy Formation Simulations. *The Astrophysical Journal*, 770(1):25, June 2013.

N. C. Amorisco, N. W. Evans, and G. van de Ven. The remnant of a merger between two dwarf galaxies in Andromeda II. *Nature*, 507: 335–337, Mar. 2014. doi: 10.1038/nature12995.

D. S. Balsara. Divergence-Free Adaptive Mesh Refinement for Magnetohydrodynamics. *Journal of Computational Physics*, 174(2):614–648, Dec. 2001.

A. M. Beck, H. Lesch, K. Dolag, H. Kotarba, A. Geng, and F. A. Stasyszyn. Origin of strong magnetic fields in Milky Way-like galactic haloes. *Monthly Notices of the Royal Astronomical Society*, 422: 2152–2163, May 2012. doi: 10.1111/j.1365-2966.2012.20759.x.

R. Beck. Magnetism in the spiral galaxy NGC 6946: magnetic arms, depolarization rings, dynamo modes, and helical fields. *Astronomy & Astrophysics*, 470:539–556, Aug. 2007. doi: 10.1051/0004-6361:20066988.

R. Beck. Magnetic fields in the nearby spiral galaxy IC 342: A multi-frequency radio polarization study. *Astronomy & Astrophysics*, 578: A93, June 2015. doi: 10.1051/0004-6361/201425572.

R. Beck. Magnetic fields in spiral galaxies. *The Astronomy and Astrophysics Review*, 24:4, Dec. 2016. doi: 10.1007/s00159-015-0084-4.

R. Beck and R. Wielebinski. *Magnetic Fields in Galaxies*, page 641. Springer Berlin Heidelberg, 2013. doi: 10.1007/978-94-007-5612-0_13.

R. Beck, A. Brandenburg, D. Moss, A. Shukurov, and D. Sokoloff. Galactic Magnetism: Recent Developments and Perspectives. *Annual Review of Astronomy & Astrophysics*, 34(1):155–206, 1996.

R. Beck, A. Shukurov, D. Sokoloff, and R. Wielebinski. Systematic bias in interstellar magnetic field estimates. *Astronomy & Astrophysics*, 411:99–107, Nov. 2003. doi: 10.1051/0004-6361:20031101.

P. S. Behroozi, R. H. Wechsler, and C. Conroy. The Average Star Formation Histories of Galaxies in Dark Matter Halos from z = 0-8. *The Astrophysical Journal*, 770:57, June 2013. doi: 10.1088/0004-637X/770/1/57.

S. V. Berdyugina. Starspots: A Key to the Stellar Dynamo. *Living Reviews in Solar Physics*, 2:8, Dec. 2005. doi: 10.12942/lrsp-2005-8.

M. L. Bernet, F. Miniati, S. J. Lilly, P. P. Kronberg, and M. Dessauges-Zavadsky. Strong magnetic fields in normal galaxies at high redshift. *Nature*, 454:302–304, July 2008. doi: 10.1038/nature07105.

L. Biermann. Über den Ursprung der Magnetfelder auf Sternen und im interstellaren Raum (miteinem Anhang von A. Schlüter). *Zeitschrift Naturforschung Teil A*, 5:65, 1950.

G. S. Bisnovatyi-Kogan, A. A. Ruzmaikin, and R. A. Syunyaev. Star Contraction and Magnetic-Field Generation in Protogalaxies. *Soviet Ast.*, 17:137, Aug. 1973.

N. A. Bond, C. W. Churchill, J. C. Charlton, and S. S. Vogt. High-redshift superwinds as the source of the strongest mg ii absorbers: A feasibility analysis. *The Astrophysical Journal*, 562(2):641, 2001. URL `http://stacks.iop.org/0004-637X/562/i=2/a=641`.

R. Bordoloi, S. J. Lilly, C. Knobel, M. Bolzonella, P. Kampczyk, C. M. Carollo, A. Iovino, E. Zucca, T. Contini, J.-P. Kneib, O. Le Fevre, V. Mainieri, A. Renzini, M. Scodeggio, G. Zamorani, I. Balestra, S. Bardelli, A. Bongiorno, K. Caputi, O. Cucciati, S. de la Torre,

L. de Ravel, B. Garilli, K. Kovač, F. Lamareille, J.-F. Le Borgne, V. Le Brun, C. Maier, M. Mignoli, R. Pello, Y. Peng, E. Perez Montero, V. Presotto, C. Scarlata, J. Silverman, M. Tanaka, L. Tasca, L. Tresse, D. Vergani, L. Barnes, A. Cappi, A. Cimatti, G. Coppa, C. Diener, P. Franzetti, A. Koekemoer, C. López-Sanjuan, H. J. McCracken, M. Moresco, P. Nair, P. Oesch, L. Pozzetti, and N. Welikala. The Radial and Azimuthal Profiles of Mg II Absorption around 0.5 < z < 0.9 zCOSMOS Galaxies of Different Colors, Masses, and Environments. *The Astrophysical Journal*, 743:10, Dec. 2011. doi: 10.1088/0004-637X/743/1/10.

A. Brandenburg and K. Subramanian. Astrophysical magnetic fields and nonlinear dynamo theory. *Phys. Rep.*, 417:1–209, Oct. 2005. doi: 10.1016/j.physrep.2005.06.005.

A. Brandenburg, D. Sokoloff, and K. Subramanian. Current Status of Turbulent Dynamo Theory. From Large-Scale to Small-Scale Dynamos. *Space Sci. Rev.*, 169:123–157, Sept. 2012. doi: 10.1007/s11214-012-9909-x.

R. Braun, G. Heald, and R. Beck. The Westerbork SINGS survey. III. Global magnetic field topology. *Astronomy & Astrophysics*, 514:A42, May 2010. doi: 10.1051/0004-6361/200913375.

C. B. Brook, G. Stinson, B. K. Gibson, J. Wadsley, and T. Quinn. MaGICC discs: matching observed galaxy relationships over a wide stellar mass range. *Monthly Notices of the Royal Astronomical Society*, 424:1275–1283, Aug. 2012. doi: 10.1111/j.1365-2966.2012.21306.x.

P. Bryans, N. R. Badnell, T. W. Gorczyca, J. M. Laming, W. Mitthumsiri, and D. W. Savin. Collisional Ionization Equilibrium for Optically Thin Plasmas. I. Updated Recombination Rate Coefficients for Bare through Sodium-like Ions. *The Astrophysical Journal Supplement Series*, 167:343–356, Dec. 2006. doi: 10.1086/507629.

J. Burgers. *The Nonlinear Diffusion Equation: Asymptotic Solutions and Statistical Problems*. SpringerLink : Bücher. Springer Netherlands, 2013. ISBN 9789401017459. URL `https://books.google.ch/books?id=U5vnCAAAQBAJ`.

J. M. Burgers. Correlation problems in a one-dimensional model of turbulence. *Proc. Acad. Sci. Amsterdam*, 53, 1950.

L. Burlaga. Voyager observations of the magnetic field in the heliosheath and the local interstellar medium. *Journal of Physics: Conference Series*, 642(1):012003, 2015. URL http://stacks.iop.org/1742-6596/642/i=1/a=012003.

I. Butsky, J. Zrake, J.-h. Kim, H.-I. Yang, and T. Abel. Ab Initio Simulations of a Supernova-driven Galactic Dynamo in an Isolated Disk Galaxy. *The Astrophysical Journal*, 843:113, July 2017. doi: 10.3847/1538-4357/aa799f.

E. R. Caley and J. F. C. Richards. *Theophrastus On Stones*. Graduate School Monographs. The Ohio State University, 1956.

P. Charbonneau and O. Steiner. *Solar and Stellar Dynamos: Saas-Fee Advanced Course 39 Swiss Society for Astrophysics and Astronomy*. Saas-Fee Advanced Course. Springer Berlin Heidelberg, 2012. ISBN 9783642320934. URL https://books.google.ch/books?id=DIXmLBR1ICsC.

S. Childress and A. Gilbert. *Stretch, Twist, Fold: The Fast Dynamo*. Lecture Notes in Physics Monographs. Springer Berlin Heidelberg, 2008. ISBN 9783540447788. URL https://books.google.ch/books?id=aJXvCAAAQBAJ.

K. T. Chyży and R. J. Buta. Discovery of a Strong Spiral Magnetic Field Crossing the Inner Pseudoring of NGC 4736. *The Astrophysical Journal Letters*, 677:L17, Apr. 2008. doi: 10.1086/587958.

K. T. Chyży, M. Weżgowiec, R. Beck, and D. J. Bomans. Magnetic fields in Local Group dwarf irregulars. *Astronomy & Astrophysics*, 529:A94, May 2011. doi: 10.1051/0004-6361/201015393.

J. M. D. Coey. *Magnetism and Magnetic Materials*. Cambridge University Press, 2010.

S. Cole, C. G. Lacey, C. M. Baugh, and C. S. Frenk. Hierarchical galaxy formation. *Monthly Notices of the Royal Astronomical Society*, 319: 168–204, Nov. 2000. doi: 10.1046/j.1365-8711.2000.03879.x.

T. G. Cowling. The stability of gaseous stars. *Monthly Notices of the Royal Astronomical Society*, 94:768–782, June 1934. doi: 10.1093/mnras/94.8.768.

W. J. G. de Blok, S. S. McGaugh, A. Bosma, and V. C. Rubin. Mass Density Profiles of Low Surface Brightness Galaxies. *The Astrophysical Journal Letters*, 552:L23–L26, May 2001. doi: 10.1086/320262.

A. Dekel, Y. Birnboim, G. Engel, J. Freundlich, T. Goerdt, M. Mumcuoglu, E. Neistein, C. Pichon, R. Teyssier, and E. Zinger. Cold streams in early massive hot haloes as the main mode of galaxy formation. *Nature*, 457(7):451–454, Jan. 2009.

F. Del Sordo, G. Guerrero, and A. Brandenburg. Turbulent dynamos with advective magnetic helicity flux. *Monthly Notices of the Royal Astronomical Society*, 429(2):1686–1694, Feb. 2013.

C. D. Dermer, M. Cavadini, S. Razzaque, J. D. Finke, J. Chiang, and B. Lott. Time Delay of Cascade Radiation for TeV Blazars and the Measurement of the Intergalactic Magnetic Field. *The Astrophysical Journal Letters*, 733:L21, June 2011. doi: 10.1088/2041-8205/733/2/L21.

C. L. Dobbs, D. J. Price, A. R. Pettitt, M. R. Bate, and T. S. Tricco. Magnetic field evolution and reversals in spiral galaxies. *Monthly Notices of the Royal Astronomical Society*, 461:4482–4495, Oct. 2016. doi: 10.1093/mnras/stw1625.

K. Dolag, D. Grasso, V. Springel, and I. Tkachev. Constrained simulations of the magnetic field in the local Universe and the propagation of ultrahigh energy cosmic rays. *J. Cosmology Astropart. Phys.*, 1:009, Jan. 2005. doi: 10.1088/1475-7516/2005/01/009.

B. T. Draine and A. Li. Infrared Emission from Interstellar Dust. IV. The Silicate-Graphite-PAH Model in the Post-Spitzer Era. *The Astrophysical Journal*, 657(2):810–837, Mar. 2007.

E. Du Trémolet de Lacheisserie, D. Gignoux, and M. Schlenker. *Magnetism*. Number v. 1 in Collection Grenoble Sciences. Springer, 2005. ISBN 9780387229676. URL `https://books.google.ch/books?id=MgCExarQD08C`.

Y. Dubois and R. Teyssier. Cosmological MHD simulation of a cooling flow cluster. *Astronomy and Astrophysics*, 482(2):L13–L16, May 2008.

Y. Dubois and R. Teyssier. Magnetised winds in dwarf galaxies. *Astronomy and Astrophysics*, 523:72, Nov. 2010.

C. P. Dullemond. Lecture notes in numerical fluid dynamics, 2008. URL `https://www.mpia.de/homes/dullemon/lectures/fluiddynamics08/`.

R. Durrer and A. Neronov. Cosmological magnetic fields: their generation, evolution and observation. *The Astronomy and Astrophysics Review*, 21:62, June 2013. doi: 10.1007/s00159-013-0062-7.

C. R. Evans and J. F. Hawley. Simulation of magnetohydrodynamic flows - A constrained transport method. *The Astrophysical Journal*, 332:659–677, Sept. 1988. doi: 10.1086/166684.

C. Federrath, G. Chabrier, J. Schober, R. Banerjee, R. S. Klessen, and D. R. G. Schleicher. Mach Number Dependence of Turbulent Magnetic Field Amplification: Solenoidal versus Compressive Flows. *Physical Review Letters*, 107(11):114504, Sept. 2011. doi: 10.1103/PhysRevLett.107.114504.

C. Federrath, J. Schober, S. Bovino, and D. R. G. Schleicher. The Turbulent Dynamo in Highly Compressible Supersonic Plasmas. *The Astrophysical Journal Letters*, 797:L19, Dec. 2014. doi: 10.1088/2041-8205/797/2/L19.

K. Ferriere. Effect of the explosion of supernovae and superbubbles on the Galactic dynamo. *Astrophysical Journal*, 391:188–198, May 1992.

K. M. Ferrière. The interstellar environment of our galaxy. *Reviews of Modern Physics*, 73:1031–1066, Oct. 2001. doi: 10.1103/RevModPhys.73.1031.

A. Fletcher. Magnetic Fields in Nearby Galaxies. In R. Kothes, T. L. Landecker, and A. G. Willis, editors, *The Dynamic Interstellar Medium: A Celebration of the Canadian Galactic Plane Survey*, volume 438 of *Astronomical Society of the Pacific Conference Series*, page 197, Dec. 2010.

S. Fromang, P. Hennebelle, and R. Teyssier. A high order Godunov scheme with constrained transport and adaptive mesh refinement for astrophysical magnetohydrodynamics. *Astronomy & Astrophysics*, 457:371–384, Oct. 2006. doi: 10.1051/0004-6361:20065371.

D. Galloway and U. Frisch. Dynamo action in a family of flows with chaotic streamlines. *Geophysical and Astrophysical Fluid Dynamics (ISSN 0309-1929)*, 36(1):53–83, 1986.

S. S. Girimaji and Y. Zhou. Spectrum and energy transfer in steady burgers turbulence. *Physics Letters A*, 202(4):279 – 287, 1995. ISSN 0375-9601. doi: https://doi.org/10.1016/0375-9601(95)00317-V. URL http://www.sciencedirect.com/science/article/pii/037596019500317V.

N. Y. Gnedin, A. Ferrara, and E. G. Zweibel. Generation of the Primordial Magnetic Fields during Cosmological Reionization. *The Astrophysical Journal*, 539:505–516, Aug. 2000. doi: 10.1086/309272.

F. Governato, C. Brook, L. Mayer, A. Brooks, G. Rhee, J. Wadsley, P. Jonsson, B. Willman, G. Stinson, T. Quinn, and P. Madau. Bulgeless dwarf galaxies and dark matter cores from supernova-driven outflows. *Nature*, 463:203–206, Jan. 2010. doi: 10.1038/nature08640.

F. Governato, A. Zolotov, A. Pontzen, C. Christensen, S. H. Oh, A. M. Brooks, T. Quinn, S. Shen, and J. Wadsley. Cuspy no more: how outflows affect the central dark matter and baryon distribution in Λ cold dark matter galaxies. *Monthly Notices of the Royal Astronomical Society*, 422:1231–1240, May 2012. doi: 10.1111/j.1365-2966.2012.20696.x.

D. Gurnett and A. Bhattacharjee. *Introduction to Plasma Physics: With Space, Laboratory and Astrophysical Applications*. Cambridge University Press, 2017. ISBN 9781107027374. URL https://books.google.ch/books?id=HR8EDgAAQBAJ.

O. Hahn and T. Abel. Multi-scale initial conditions for cosmological simulations. *Monthly Notices of the Royal Astronomical Society*, 415:2101–2121, Aug. 2011. doi: 10.1111/j.1365-2966.2011.18820.x.

G. E. Hale. SOLAR VORTICES (Contributions from the Mt. Wilson Solar Observatory, No. 26). *The Astrophysical Journal*, 28:100, Sept. 1908a. doi: 10.1086/141581.

G. E. Hale. On the Probable Existence of a Magnetic Field in Sun-Spots. *The Astrophysical Journal*, 28:315, Nov. 1908b. doi: 10.1086/141602.

J. L. Han, R. N. Manchester, A. G. Lyne, G. J. Qiao, and W. van Straten. Pulsar Rotation Measures and the Large-Scale Structure of the Galactic Magnetic Field. *The Astrophysical Journal*, 642:868–881, May 2006. doi: 10.1086/501444.

M. Hanasz, G. Kowal, K. Otmianowska-Mazur, and H. Lesch. Amplification of Galactic Magnetic Fields by the Cosmic-Ray-driven Dynamo. *The Astrophysical Journal*, 605(1):L33–L36, Apr. 2004.

N. E. L. Haugen, A. Brandenburg, and W. Dobler. Simulations of nonhelical hydromagnetic turbulence. *Physical Review E*, 70(1): 016308, July 2004.

V. Heesen, E. Brinks, A. K. Leroy, G. Heald, R. Braun, F. Bigiel, and R. Beck. The Radio Continuum-Star Formation Rate Relation in WSRT SINGS Galaxies. *The Astronomical Journal*, 147:103, May 2014. doi: 10.1088/0004-6256/147/5/103.

P. F. Hopkins, P. F. Hopkins, E. Quataert, and N. Murray. The structure of the interstellar medium of star-forming galaxies. *Monthly Notices of the Royal Astronomical Society*, 421(4):2654–3521, Mar. 2012.

P. F. Hopkins, D. Kereš, J. Onorbe, C.-A. Faucher-Giguère, E. Quataert, N. Murray, and J. S. Bullock. Galaxies on FIRE (Feedback In Realistic Environments): stellar feedback explains cosmologically inefficient star formation. *Monthly Notices of the Royal Astronomical Society*, 445 (1):581–603, Nov. 2014.

B. Hunt. *The Maxwellians*. Cornell History of Science Series. Cornell University Press, 1991. ISBN 9780801426414. URL `https://books.google.ch/books?id=rLnvAAAAMAAJ`.

K. Ichiki, K. Takahashi, N. Sugiyama, H. Hanayama, and H. Ohno. Magnetic Field Spectrum at Cosmological Recombination. *ArXiv Astrophysics e-prints*, Jan. 2007.

M. D. Johnson, V. L. Fish, S. S. Doeleman, D. P. Marrone, R. L. Plambeck, J. F. C. Wardle, K. Akiyama, K. Asada, C. Beaudoin, L. Blackburn, R. Blundell, G. C. Bower, C. Brinkerink, A. E. Broderick, R. Cappallo, A. A. Chael, G. B. Crew, J. Dexter, M. Dexter, R. Freund, P. Friberg, R. Gold, M. A. Gurwell, P. T. P. Ho, M. Honma, M. Inoue, M. Kosowsky, T. P. Krichbaum, J. Lamb, A. Loeb, R.-S. Lu, D. MacMahon, J. C. McKinney, J. M. Moran, R. Narayan, R. A. Primiani, D. Psaltis, A. E. E. Rogers, K. Rosenfeld, J. SooHoo, R. P. J. Tilanus, M. Titus, L. Vertatschitsch, J. Weintroub, M. Wright, K. H. Young, J. A. Zensus, and L. M. Ziurys. Resolved magnetic-field structure and variability near the event horizon of Sagittarius A*. *Science*, 350:1242–1245, Dec. 2015. doi: 10.1126/science.aac7087.

G. Kauffmann. Quantitative constraints on starburst cycles in galaxies with stellar masses in the range 10^8-10^{10} $M_\odot$. *Monthly Notices of the Royal Astronomical Society*, 441:2717–2724, July 2014. doi: 10.1093/mnras/stu752.

A. P. Kazantsev. Enhancement of a Magnetic Field by a Conducting Fluid. *Soviet Physics JETP*, 26:1031, May 1968.

S. Kazantzidis, J. Magorrian, and B. Moore. Generating Equilibrium Dark Matter Halos: Inadequacies of the Local Maxwellian Approximation. *The Astrophysical Journal*, 601(1):37–46, Jan. 2004.

D. Kereš, N. Katz, D. H. Weinberg, and R. Davé. How do galaxies get their gas? *Monthly Notices of the Royal Astronomical Society*, 363(1): 2–28, Oct. 2005.

K. S. Kim. Magnetic fields in the circumgalactic media of galaxies at intermediate redshifts. Doctoral thesis, ETH Zürich, 2017.

K. S. Kim, S. J. Lilly, F. Miniati, M. L. Bernet, R. Beck, S. P. O'Sullivan, and B. M. Gaensler. Faraday Rotation Measure Synthesis of Intermediate Redshift Quasars as a Probe of Intervening Matter. *The Astrophysical Journal*, 829:133, Oct. 2016. doi: 10.3847/0004-637X/829/2/133.

K. S. Kim, S. J. Lilly, M. Rieder, and R. Teyssier. Faraday Rotation Measure Synthesis as Smoking Gun of the Turbulent Dynamo. *In preparation*, 2017.

T. Kimm and R. Cen. Escape Fraction of Ionizing Photons during Reionization: Effects due to Supernova Feedback and Runaway OB Stars. *The Astrophysical Journal*, 788:121, June 2014. doi: 10.1088/0004-637X/788/2/121.

R. S. Klessen and S. C. O. Glover. Physical Processes in the Interstellar Medium. *Star Formation in Galaxy Evolution: Connecting Numerical Models to Reality, Saas-Fee Advanced Course, Volume 43. ISBN 978-3-662-47889-9. Springer-Verlag Berlin Heidelberg, 2016, p. 85*, 43:85, 2016. doi: 10.1007/978-3-662-47890-5_2.

A. Kolmogorov. The Local Structure of Turbulence in Incompressible Viscous Fluid for Very Large Reynolds' Numbers. *Akademiia Nauk SSSR Doklady*, 30:301–305, 1941.

M. R. Krumholz and J. C. Tan. Slow Star Formation in Dense Gas: Evidence and Implications. *The Astrophysical Journal*, 654(1):304–315, Jan. 2007.

R. M. Kulsrud and S. W. Anderson. The spectrum of random magnetic fields in the mean field dynamo theory of the Galactic magnetic field. *The Astrophysical Journal*, 396:606–630, Sept. 1992. doi: 10.1086/171743.

R. M. Kulsrud, R. Cen, J. P. Ostriker, and D. Ryu. The Protogalactic Origin for Cosmic Magnetic Fields. *The Astrophysical Journal*, 480:481–491, May 1997. doi: 10.1086/303987.

M. Lazar, R. Schlickeiser, R. Wielebinski, and S. Poedts. Cosmological Effects of Weibel-Type Instabilities. *The Astrophysical Journal*, 693:1133–1141, Mar. 2009. doi: 10.1088/0004-637X/693/2/1133.

J. M. Lotz, P. Jonsson, T. J. Cox, D. Croton, J. R. Primack, R. S. Somerville, and K. Stewart. The Major and Minor Galaxy Merger Rates at $z < 1.5$. *The Astrophysical Journal*, 742:103, Dec. 2011. doi: 10.1088/0004-637X/742/2/103.

W. Lowrie. *Fundamentals of Geophysics*. Cambridge University Press, 2007.

S. Mao, N. McClure-Griffiths, B. Gaensler, M. Haverkorn, R. Beck, D. McConnell, M. Wolleben, S. Stanimirović, J. Dickey, and L. Staveley-Smith. Magnetic field structure of the large magellanic cloud from faraday rotation measures of diffuse polarized emission. *The Astrophysical Journal*, 759(1):25, 2012.

S. A. Mao, N. M. McClure-Griffiths, B. M. Gaensler, J. C. Brown, C. L. van Eck, M. Haverkorn, P. P. Kronberg, J. M. Stil, A. Shukurov, and A. R. Taylor. New Constraints on the Galactic Halo Magnetic Field Using Rotation Measures of Extragalactic Sources toward the Outer Galaxy. *The Astrophysical Journal*, 755:21, Aug. 2012. doi: 10.1088/0004-637X/755/1/21.

H. Martel and P. R. Shapiro. A convenient set of comoving cosmological variables and their application. *Monthly Notices of the Royal Astronomical Society*, 297:467–485, June 1998. doi: 10.1046/j.1365-8711.1998.01497.x.

C. L. Martin. Properties of Galactic Outflows: Measurements of the Feedback from Star Formation. *The Astrophysical Journal*, 513(1): 156–160, Mar. 1999.

J. Mathieu and J. Scott. *An Introduction to Turbulent Flow*. Cambridge University Press, 2000. ISBN 9780521775380. URL `https://books.google.ch/books?id=nVA53NEAx64C`.

J. C. Maxwell. A dynamical theory of the electromagnetic field. *Philosophical Transactions of the Royal Society of London*, 155:459–512, 1865. doi: 10.1098/rstl.1865.0008. URL `http://rstl.royalsocietypublishing.org/content/155/459.short`.

F. Miniati. The Matryoshka Run: A Eulerian Refinement Strategy to Study the Statistics of Turbulence in Virialized Cosmic Structures. *The Astrophysical Journal*, 782:21, Feb. 2014. doi: 10.1088/0004-637X/782/1/21.

F. Miniati and A. Beresnyak. Self-similar energetics in large clusters of galaxies. *Nature*, 523:59–62, July 2015. doi: 10.1038/nature14552.

P. Mocz, R. Pakmor, V. Springel, M. Vogelsberger, F. Marinacci, and L. Hernquist. A moving mesh unstaggered constrained transport

scheme for magnetohydrodynamics. *Monthly Notices of the Royal Astronomical Society*, 463:477–488, Nov. 2016. doi: 10.1093/mnras/stw2004.

P. J. Mohr, D. B. Newell, and B. N. Taylor. CODATA recommended values of the fundamental physical constants: 2014*. *Reviews of Modern Physics*, 88(3):035009, July 2016. doi: 10.1103/RevModPhys.88.035009.

B. P. Moster, T. Naab, and S. D. M. White. Galactic star formation and accretion histories from matching galaxies to dark matter haloes. *Monthly Notices of the Royal Astronomical Society*, 428:3121–3138, Feb. 2013. doi: 10.1093/mnras/sts261.

N. Murray, E. Quataert, and T. A. Thompson. The Disruption of Giant Molecular Clouds by Radiation Pressure & the Efficiency of Star Formation in Galaxies. *The Astrophysical Journal*, 709(1):191–209, Jan. 2010.

S. Naoz and R. Narayan. Generation of Primordial Magnetic Fields on Linear Overdensity Scales. *Physical Review Letters*, 111(5):051303, Aug. 2013.

J. F. Navarro, C. S. Frenk, and S. D. M. White. A Universal Density Profile from Hierarchical Clustering. *Astrophysical Journal v.490*, 490:493, Dec. 1997.

A. Neronov and I. Vovk. Evidence for Strong Extragalactic Magnetic Fields from Fermi Observations of TeV Blazars. *Science*, 328:73, Apr. 2010. doi: 10.1126/science.1184192.

P. Ocvirk, C. Pichon, and R. Teyssier. Bimodal gas accretion in the Horizon-MareNostrum galaxy formation simulation. *Monthly Notices of the Royal Astronomical Society*, 390(4):1326–1338, Nov. 2008.

H. Ohno and S. Shibata. The random magnetic field in the Galaxy. *Monthly Notices of the Royal Astronomical Society*, 262:953–962, June 1993. doi: 10.1093/mnras/262.4.953.

B. D. Oppenheimer and R. Davé. Cosmological simulations of intergalactic medium enrichment from galactic outflows. *Monthly Notices of the Royal Astronomical Society*, 373(4):1265–1292, Dec. 2006.

N. Oppermann, H. Junklewitz, G. Robbers, M. R. Bell, T. A. Enßlin, A. Bonafede, R. Braun, J. C. Brown, T. E. Clarke, I. J. Feain, B. M. Gaensler, A. Hammond, L. Harvey-Smith, G. Heald, M. Johnston-Hollitt, U. Klein, P. P. Kronberg, S. A. Mao, N. M. McClure-Griffiths, S. P. O'Sullivan, L. Pratley, T. Robishaw, S. Roy, D. H. F. M. Schnitzeler, C. Sotomayor-Beltran, J. Stevens, J. M. Stil, C. Sunstrum, A. Tanna, A. R. Taylor, and C. L. Van Eck. An improved map of the Galactic Faraday sky. *Astronomy & Astrophysics*, 542: A93, June 2012. doi: 10.1051/0004-6361/201118526.

R. Pakmor and V. Springel. Simulations of magnetic fields in isolated disc galaxies. *Monthly Notices of the Royal Astronomical Society*, 432: 176–193, June 2013. doi: 10.1093/mnras/stt428.

R. Pakmor, A. Bauer, and V. Springel. Magnetohydrodynamics on an unstructured moving grid. *Monthly Notices of the Royal Astronomical Society*, 418(2):1392–1401, Dec. 2011.

R. Pakmor, F. Marinacci, and V. Springel. Magnetic Fields in Cosmological Simulations of Disk Galaxies. *The Astrophysical Journal Letters*, 783:L20, Mar. 2014. doi: 10.1088/2041-8205/783/1/L20.

R. Pakmor, F. A. Gómez, R. J. J. Grand, F. Marinacci, C. M. Simpson, V. Springel, D. J. R. Campbell, C. S. Frenk, T. Guillet, C. Pfrommer, and S. D. M. White. Magnetic field formation in the Milky Way like disc galaxies of the Auriga project. *Monthly Notices of the Royal Astronomical Society*, 469:3185–3199, Aug. 2017. doi: 10.1093/mnras/stx1074.

V. I. Pariev, S. A. Colgate, and J. Finn. A magnetic α-ω dynamo in agn disks. ii. magnetic field generation, theories, and simulations. *The Astrophysical Journal*, 658(1):129, 2007.

E. N. Parker. The Origin of Magnetic Fields. *Astrophysical Journal*, 160: 383, May 1970.

E. N. Parker. Fast dynamos, cosmic rays, and the Galactic magnetic field. *Astrophysical Journal*, 401:137–145, Dec. 1992.

I. Patrikeev, A. Fletcher, R. Stepanov, R. Beck, E. M. Berkhuijsen, P. Frick, and C. Horellou. Analysis of spiral arms using anisotropic

wavelets: gas, dust and magnetic fields in M 51. *Astronomy & Astrophysics*, 458:441–452, Nov. 2006. doi: 10.1051/0004-6361:20065225.

C. Pfrommer, R. Pakmor, K. Schaal, C. M. Simpson, and V. Springel. Simulating cosmic ray physics on a moving mesh. *Monthly Notices of the Royal Astronomical Society*, 465:4500–4529, Mar. 2017. doi: 10.1093/mnras/stw2941.

Planck Collaboration, P. A. R. Ade, N. Aghanim, M. Arnaud, F. Arroja, M. Ashdown, J. Aumont, C. Baccigalupi, M. Ballardini, A. J. Banday, and et al. Planck 2015 results. XIX. Constraints on primordial magnetic fields. *Astronomy & Astrophysics*, 594:A19, Sept. 2016a. doi: 10.1051/0004-6361/201525821.

Planck Collaboration, P. A. R. Ade, N. Aghanim, M. Arnaud, M. Ashdown, J. Aumont, C. Baccigalupi, A. J. Banday, R. B. Barreiro, J. G. Bartlett, and et al. Planck 2015 results. XIII. Cosmological parameters. *Astronomy & Astrophysics*, 594:A13, Sept. 2016b. doi: 10.1051/0004-6361/201525830.

Y. B. Ponomarenko. Theory of the hydromagnetic generator. *Journal of Applied Mechanics and Technical Physics*, 14(6):775–778, Nov. 1973.

A. Pontzen and F. Governato. How supernova feedback turns dark matter cusps into cores. *Monthly Notices of the Royal Astronomical Society*, 421(4):3464–3471, Apr. 2012.

Y. Rasera and R. Teyssier. The history of the baryon budget. Cosmic logistics in a hierarchical universe. *Astronomy & Astrophysics*, 445: 1–27, Jan. 2006. doi: 10.1051/0004-6361:20053116.

J. I. Read, M. I. Wilkinson, N. W. Evans, N. W. Evans, G. Gilmore, J. T. Kleyna, and J. T. Kleyna. The importance of tides for the Local Group dwarf spheroidals. *Monthly Notices of the Royal Astronomical Society*, 367(1):387–399, Mar. 2006.

M. J. Rees. Magnetic Fields in the Early Universe. In R. Wielebinski and R. Beck, editors, *Cosmic Magnetic Fields*, volume 664 of *Lecture Notes in Physics, Berlin Springer Verlag*, pages 6–7, 2005. doi: 10.1007/11369875_1.

A. Reisenegger. Magnetic field evolution in neutron stars. *Astronomische Nachrichten*, 328:1173, Dec. 2007. doi: 10.1002/asna.200710848.

M. Rieder and R. Teyssier. A small-scale dynamo in feedback-dominated galaxies as the origin of cosmic magnetic fields - I. The kinematic phase. *Monthly Notices of the Royal Astronomical Society*, 457:1722–1738, Apr. 2016. doi: 10.1093/mnras/stv2985.

M. Rieder and R. Teyssier. A small-scale dynamo in feedback-dominated galaxies - II. The saturation phase and the final magnetic configuration. *Monthly Notices of the Royal Astronomical Society*, 471: 2674–2686, Nov. 2017a. doi: 10.1093/mnras/stx1670.

M. Rieder and R. Teyssier. A small-scale dynamo in feedback-dominated galaxies - III. Cosmological simulations. *Monthly Notices of the Royal Astronomical Society*, 472:4368–4373, Dec. 2017b. doi: 10.1093/mnras/stx2276.

T. Robishaw, E. Quataert, and C. Heiles. Extragalactic Zeeman Detections in OH Megamasers. *The Astrophysical Journal*, 680:981-998, June 2008. doi: 10.1086/588031.

A. Rosen, A. Rosen, and J. N. Bregman. Global Models of the Interstellar Medium in Disk Galaxies. *Astrophysical Journal v.440*, 440:634, Feb. 1995.

R. Roškar, R. Teyssier, O. Agertz, M. Wetzstein, and B. Moore. A systematic look at the effects of radiative feedback on disc galaxy formation. *Monthly Notices of the Royal Astronomical Society*, 444(3): 2837–2853, Nov. 2014.

G. Rüdiger and R. Hollerbach. *The Magnetic Universe*. WILEY-VCH Verlag, 2004.

C. Scannapieco, C. Scannapieco, M. Wadepuhl, M. Wadepuhl, O. H. Parry, O. H. Parry, J. F. Navarro, A. Jenkins, A. Jenkins, V. Springel, and R. Teyssier. The Aquila comparison project: the effects of feedback and numerical methods on simulations of galaxy formation. *Monthly Notices of the Royal Astronomical Society*, page 2970, Apr. 2012.

A. A. Schekochihin, S. C. Cowley, S. F. Taylor, J. L. Maron, and J. C. McWilliams. Simulations of the Small-Scale Turbulent Dynamo. *The Astrophysical Journal*, 612:276–307, Sept. 2004. doi: 10.1086/422547.

R. Schlickeiser. Cosmic Magnetization: From Spontaneously Emitted Aperiodic Turbulent to Ordered Equipartition Fields. *Physical Review Letters*, 109(26):261101, Dec. 2012. doi: 10.1103/PhysRevLett.109.261101.

J. Schober, D. R. G. Schleicher, C. Federrath, S. Bovino, and R. S. Klessen. Saturation of the turbulent dynamo. *Phys. Rev. E*, 92(2):023010, Aug. 2015. doi: 10.1103/PhysRevE.92.023010.

D. Semenov, T. Henning, C. Helling, M. Ilgner, and E. Sedlmayr. Rosseland and Planck mean opacities for protoplanetary discs. *Astronomy and Astrophysics*, 410(2):611–621, Nov. 2003.

M. Soida, R. Beck, M. Urbanik, and J. Braine. Magnetic fields in the absence of spiral density waves - NGC 4414. *Astronomy & Astrophysics*, 394:47–57, Oct. 2002. doi: 10.1051/0004-6361:20021100.

L. Spitzer, Jr. The Dynamics of the Interstellar Medium. I. Local Equilibrium. *The Astrophysical Journal*, 93:369, May 1941. doi: 10.1086/144273.

J. Squire and A. Bhattacharjee. Generation of Large-Scale Magnetic Fields by Small-Scale Dynamo in Shear Flows. *Physical Review Letters*, 115(17):175003, Oct. 2015. doi: 10.1103/PhysRevLett.115.175003.

C. C. Steidel, D. K. Erb, A. E. Shapley, M. Pettini, N. Reddy, M. Bogosavljević, G. C. Rudie, and O. Rakic. The Structure and Kinematics of the Circumgalactic Medium from Far-ultraviolet Spectra of z ~= 2-3 Galaxies. *The Astrophysical Journal*, 717(1):289–322, July 2010.

R. S. Sutherland and M. A. Dopita. Cooling functions for low-density astrophysical plasmas. *Astrophysical Journal Supplement Series (ISSN 0067-0049)*, 88:253–327, Sept. 1993.

A. R. Taylor, J. M. Stil, and C. Sunstrum. A Rotation Measure Image of the Sky. *The Astrophysical Journal*, 702:1230–1236, Sept. 2009. doi: 10.1088/0004-637X/702/2/1230.

B. Tessore, A. Lèbre, J. Morin, P. Mathias, E. Josselin, and M. Aurière. Measuring surface magnetic fields of red supergiant stars. *Astronomy & Astrophysics*, 603:A129, July 2017. doi: 10.1051/0004-6361/201730473.

R. Teyssier. Cosmological hydrodynamics with adaptive mesh refinement. A new high resolution code called RAMSES. *Astronomy & Astrophysics*, 385:337–364, Apr. 2002. doi: 10.1051/0004-6361:20011817.

R. Teyssier. Grid-Based Hydrodynamics in Astrophysical Fluid Flows. *Annual Review of Astronomy and Astrophysics*, 53:325–364, Aug. 2015. doi: 10.1146/annurev-astro-082214-122309.

R. Teyssier, S. Fromang, and E. Dormy. Kinematic dynamos using constrained transport with high order Godunov schemes and adaptive mesh refinement. *Journal of Computational Physics*, 218:44–67, Oct. 2006. doi: 10.1016/j.jcp.2006.01.042.

R. Teyssier, A. Pontzen, Y. Dubois, and J. I. Read. Cusp-core transformations in dwarf galaxies: observational predictions. *Monthly Notices of the Royal Astronomical Society*, 429:3068–3078, Mar. 2013. doi: 10.1093/mnras/sts563.

G. Tóth and P. L. Roe. Divergence- and Curl-Preserving Prolongation and Restriction Formulas. *Journal of Computational Physics*, 180(2): 736–750, Aug. 2002.

T. S. Tricco, D. J. Price, and C. Federrath. A comparison between grid and particle methods on the small-scale dynamo in magnetized supersonic turbulence. *Monthly Notices of the Royal Astronomical Society*, 461:1260–1275, Sept. 2016. doi: 10.1093/mnras/stw1280.

J. K. Truelove, R. I. Klein, C. F. McKee, J. H. I. Holliman, L. H. Howell, and J. A. Greenough. The Jeans Condition: A New Constraint on Spatial Resolution in Simulations of Isothermal Self-gravitational Hydrodynamics. *Astrophysical Journal Letters v.489*, 489:L179, Nov. 1997.

M. S. Turner and L. M. Widrow. Inflation-produced, large-scale magnetic fields. *Phys. Rev. D*, 37:2743–2754, May 1988. doi: 10.1103/PhysRevD.37.2743.

P. Tzeferacos, A. Rigby, A. Bott, A. R. Bell, R. Bingham, A. Casner, F. Cattaneo, E. M. Churazov, J. Emig, N. Flocke, F. Fiuza, C. B. Forest, J. Foster, C. Graziani, J. Katz, M. Koenig, C.-K. Li, J. Meinecke, R. Petrasso, H.-S. Park, B. A. Remington, J. S. Ross, D. Ryu, D. Ryutov, K. Weide, T. G. White, B. Reville, F. Miniati, A. A. Schekochihin, D. H. Froula, G. Gregori, and D. Q. Lamb. Numerical modeling of laser-driven experiments aiming to demonstrate magnetic field amplification via turbulent dynamo. *Physics of Plasmas*, 24(4):041404, Apr. 2017. doi: 10.1063/1.4978628.

T. Vachaspati. Magnetic fields from cosmological phase transitions. *Physics Letters B*, 265:258–261, Aug. 1991. doi: 10.1016/0370-2693(91)90051-Q.

S. I. Vainshtein and F. Cattaneo. Nonlinear restrictions on dynamo action. *Astrophysical Journal*, 393:165–171, July 1992.

C. L. Van Eck, J. C. Brown, A. Shukurov, and A. Fletcher. Magnetic Fields in a Sample of Nearby Spiral Galaxies. *The Astrophysical Journal*, 799:35, Jan. 2015. doi: 10.1088/0004-637X/799/1/35.

S. I. Vaĭnshteĭn and Y. B. Zel'dovich. REVIEWS OF TOPICAL PROBLEMS: Origin of Magnetic Fields in Astrophysics (Turbulent "Dynamo" Mechanisms). *Soviet Physics Uspekhi*, 15:159–172, Feb. 1972. doi: 10.1070/PU1972v015n02ABEH004960.

F. Vazza, T. W. Jones, M. Brüggen, G. Brunetti, C. Gheller, D. Porter, and D. Ryu. Turbulence and vorticity in Galaxy clusters generated by structure formation. *Monthly Notices of the Royal Astronomical Society*, 464:210–230, Jan. 2017. doi: 10.1093/mnras/stw2351.

M. Vietri. *Foundations of High-Energy Astrophysics*. Theoretical Astrophysics. University of Chicago Press, 2008. ISBN 9780226855714. URL `https://books.google.ch/books?id=faK5nmgWVysC`.

I. Vovk, A. M. Taylor, D. Semikoz, and A. Neronov. Fermi/LAT Observations of 1ES 0229+200: Implications for Extragalactic Magnetic Fields and Background Light. *The Astrophysical Journal Letters*, 747:L14, Mar. 2012. doi: 10.1088/2041-8205/747/1/L14.

L. Wang, A. A. Dutton, G. S. Stinson, A. V. Macciò, C. Penzo, X. Kang, B. W. Keller, and J. Wadsley. NIHAO project - I. Reproducing the inefficiency of galaxy formation across cosmic time with a large sample of cosmological hydrodynamical simulations. *Monthly Notices of the Royal Astronomical Society*, 454:83–94, Nov. 2015. doi: 10.1093/mnras/stv1937.

P. Wang and T. Abel. Magnetohydrodynamic Simulations of Disk Galaxy Formation: The Magnetization of the Cold and Warm Medium. *The Astrophysical Journal*, 696:96–109, May 2009. doi: 10.1088/0004-637X/696/1/96.

S. D. M. White and C. S. Frenk. Galaxy formation through hierarchical clustering. *The Astrophysical Journal*, 379:52–79, Sept. 1991. doi: 10.1086/170483.

L. M. Widrow. Origin of galactic and extragalactic magnetic fields. *Reviews of Modern Physics*, 74(3):775–823, 2002.

J. H. Wise, T. Abel, M. J. Turk, M. L. Norman, and B. D. Smith. The birth of a galaxy - II. The role of radiation pressure. *Monthly Notices of the Royal Astronomical Society*, 427:311–326, Nov. 2012. doi: 10.1111/j.1365-2966.2012.21809.x.

K. Yee. Numerical solution of inital boundary value problems involving maxwell's equations in isotropic media. *IEEE Transactions on Antennas and Propagation*, 14:302–307, May 1966. doi: 10.1109/TAP.1966.1138693.